Uncertainty and Robust Design in Aeroelastic Tailoring

Thesis submitted in accordance with the requirements of
the University of Liverpool for the degree of Doctor in
Philosophy

by

Abdul Manan

September 2009

Abstract

Traditional deterministic aeroelastic design approaches use safety factors and worst-case design scenarios to account for uncertainties and consequently designs are produced which are either conservative (inefficient and overcompensated) or unknowingly dangerous. In order to address the shortcomings of the deterministic approaches, three key challenges must be met: first, to decide upon the relevant uncertainty model, second, the development of methodologies that incorporate these uncertainties and finally, robust optimisation of aeroelastic systems.

Development of the uncertainty quantification and robust optimum design approaches by including uncertainties are the objectives in the present research work. This research exploits the Polynomial Chaos Expansion (PCE) to develop probabilistic aeroelastic models that include the Probability Distribution Functions (PDFs) of all uncertain parameters and the uncertainty quantification of the aeroelastic stability and response. An interval Analysis (IA) approach is also presented for the case of bounded-but-uncertain parameters. As a special case, IA is extended to account for the uncertain parameters, which are defined with PDFs.

The capabilities of these methodologies are utilised in the context of the design robustness by highlighting the impact of uncertainties in the design parameters for single and multi-objective design optimisation problems.

The PCE approach for the prediction of aeroelastic stability is demonstrated on an idealised flat plate wing model, the Goland wing and a more realistic full-scale FE composite wing model. An excellent

agreement with Monte Carlo Simulation (MCS) results is obtained but with much less computational time.

The effect of matrix cracking, with various amounts of crack density, on the aeroelastic stability of the full-scale FE aircraft composite wing is demonstrated and a 2-D PCE model, which has structural and damage parameters uncertainties is also presented for the flutter speed PDF.

Finally, the PCE approach is used to predict the uncertain bounds of the Frequency Response Function (FRF) of a FE beam model and the full-scale FE aircraft composite wing model; the results show that the approach is accurate and efficient.

Contents

List of Figures

List of Tables

Acknowledgements

I would like to express my gratitude to Prof Jonathan Edward Cooper for his guidance, support and encouragement throughout my research.

Financial support from the National Engineering and Scientific Commission (NESCOM-Pakistan), the 'UK/US composite project' and the University of Liverpool is gratefully acknowledged.

Technical discussions with some of my colleagues have been helpful. Among them are Dr Greg Dimitriadis, Dr Gareth Vio, Nick, Simon Miller and Hammed. Thanks to Hammed for sharing Monte Carlo Simulation results of the Goland wing.

The motivational support from my parents is something beyond mentioning. Their endless support and encouragement helped me a lot during the research work.

Finally, the completion of this research would not have been possible without the support and love of my wife, Tahira Sharif.

Nomenclature

A	mass matrix
$a_{i1}.....a_{ip}$	deterministic coefficients
B	aerodynamic damping matrix
C	aerodynamic stiffness matrix
c_1	particle belief factor
c_2	swarm belief factor
D	structural damping matrix
E	structural stiffness matrix
g_i	best position found by entire swarm
H	Frequency Response Function
H_f	Fitted Frequency Response Function
I	identity matrix
j	$\sqrt{-1}$
k	order of random variable or iteration number
[K], k	Global / element stiffness matrix
L	beam element length
[M], m	Global / element mass matrix
m_L	mass per unit length
N	dimension of search space
n	number of modes or number of Gaussian random variables
O	null matrix
p_i	best position found by i^{th} particle
P	order of Hermite polynomial
Q	eigen matrix of aeroelastic system
$q_i(t)$	generalized displacement of the i^{th} mode
$\dot{q}$	first derivative of $q_i(t)$

$\ddot{q}$	second derivative of $q_i(t)$
V	velocity
v_i	velocity of ith particle
w	out of plane deflection of wing or inertia factor
x_i	position of ith particle
$\gamma(x,y)$	assumed mode shape functions
ρ	density of air
$\xi_{i1}(\theta)$	set of independent standard Gaussian random variables
$\Gamma_p\lfloor\xi_{i1}(\theta).....\xi_{ip}(\theta)\rfloor$	set of multidimensional Hermite polynomials of order p.
β_i	deterministic coefficients
$\psi_i(\xi(\theta))$	set of multidimensional Hermite polynomial
δ_{ij}	knocker delta
λ	eigen value corresponding to unstable branch (i.e. flutter speed)
var(λ)	variance of eigen value λ
μ	mean flutter speed
σ	standard deviation as predicted by 2nd order PCE model
ω_i	Frequency of mode i
ζ_i	Damping ratio of mode i
PDF	probability density function
ϕ_{1d} and ϕ_{2d}	uniformly distributed random numbers

Chapter 1

Introduction

Aeroelasticity is the science which addresses the interaction of the aerodynamic, elastic and inertia forces, and the influence of this interaction on the aircraft design and performance[1]. Interactions of the said forces give rise to the various phenomena such as flutter and divergence, which indicate the onset of dynamic and static instabilities of the structure respectively. The aeroelastic response due to gust and manoeuvres is also important as this determines the sizing of the aircraft structures.

It is a well-known fact that the structural properties are uncertain and no two of the same structures are identical. For example, the material properties, laminate thickness and laminate fibre orientation angle due to the manufacturing limitations, resulting in the uncertain aeroelastic stability. Furthermore, the matrix cracking[2, 3], moisture absorption[4, 5] or the fibre breakage[4] due to the excessive and/ or fatigue loads can increase the stability uncertainty considerably.

The traditional deterministic design approaches ignore these structural and damage parameter uncertainties and adopt the safety factor and worst-case design scenarios principles in order to account for these uncertainties. Although with the aeroelastic tailoring approach, the composite designs are optimised, but potentially these designs can be sensitive to the uncertainties making them not only vulnerable but also their ability of robustness (an ability to be insensitive to a small uncertainty) a questionable. Similarly, the conservative designs produced from the deterministic design approaches can be inefficient and the uncertainties in these designs are overcompensated for.

The goal of the present research is to develop efficient and accurate design approaches which can incorporate these uncertainties, predict their effects, and explore robust optimum aeroelastic designs. Two methodologies, namely the Polynomial Chaos Expansion Method (PCE) and the Interval Analysis (probabilistic and non-probabilistic) have been explored to predict the bounds on the flutter/divergence speed and root bending moment due to gusts under uncertainty. The PCE approach has been applied for the first time in the aeroelastic field.

Furthermore, the two new approaches to predict the robust optimum designs for single and multi-objective aeroelastic optimisation problems utilizing the PCE and Interval Analysis approaches based on the Robust Pareto solution have been presented.

The damage due to the matrix cracks and the fibre breakage is incorporated into a full-scale FE aircraft composite wing model to study its effects on the aeroelastic stability and response. A new concept, in which the matrix crack density in the composite structure is dealt with in a probabilistic manner along with the structural parameter uncertainties, has been presented.

Finally, the present proposed methodologies provide a way to understand the aeroelastic stability and response variations due to the uncertainties, and then offer a solution to predict the robust optimum design performance of which is better(with less probability of failure and/or least sensitive to the small changes) compared with the deterministic optimum design.

Chapter 2 contains a literature review of aeroelasticity, aeroelastic tailoring, uncertainty modelling, robust design and damage.

Chapter 3 begins with the development of the aeroelastic and aero-servo-elastic models of an idealised rectangular composite wing. In the aeroelastic models, the Rayleigh-Ritz energy principles are adopted to model the structure whereas the unsteady aerodynamic models (with constant or frequency dependent aerodynamics) are derived using a modified strip theory approach via the torsional velocity term. Making use of the Lagrange's equation by considering the incremental work done over the entire wing due to the lift and the pitching moment (about the flexural axis) eventually yields the mathematical models. The 'P-K'frequency matching method, is adopted when aerodynamic model is frequency dependent whereas in an aero-servo-elastic model the gust response (i.e. minimise the root bending moment) is controlled in an active manner by using the wing aileron.

In chapter 4, Binary Genetic Algorithm (BGA) and Particle Swarm Optimisation (PSO) approaches are adopted for the aeroelastic tailoring of the composite wing. Three types of optimisation problems are defined to find the optimum fibre orientation angles: 1) Maximisation of the flutter/divergence speed: 2) Minimisation of the root bending moment caused by a gust in a passive manner: 3) Maximisation of the flutter/divergence speed and minimisation of the root bending moment caused due to gust- a multi objective problem.

In chapter 5, two approaches are explored to predict the bounds on aeroelastic stability and response: 1) Polynomial Chaos Expansion Method(PCE): 2) Interval Analysis (probabilistic and non-probabilistic) Approach. Two solutions of the PCE Method, PCE–Regression and PCE-Statistically Averaging Method (SAM) concepts, are presented. These approaches are applied on various types of the wing models to predict the bounds on the Flutter/ Divergence Speed and variation in Root Bending Moment arising due to "1-Cosine" discrete gust by

considering uncertainties in material properties, fibre angle and thickness. Finally, the PCE approach is tested to predict the uncertainty bounds of the Frequency Response Function of the FE beam model and the full-scale FE aircraft composite wing model, and an excellent agreement with MCS is obtained with much less computational time.

In chapter 6, two criteria for the robust design are presented; first when PDF of response is available (for example from PCE approach) and in second case when only upper and lower bounds are known (for example from non-probabilistic interval analysis approach). Furthermore, PDF estimates predicted by PCE (due to structural parameters) and upper and lower bounds from the non-probabilistic interval analysis approach are then utilized to predict the robust optimum design of the composite plate wing model against some design flutter and gust requirements.

In chapter 7, the effect of damage(defined via Talreja[2] and self-consistent[3] models) on the flutter speed, gust response against '1-cosine' discrete gusts, and the static wing bending deflection and wing twist at a particular flight condition are predicted and compared with an undamaged case.

Finally, Chapter 8 contains conclusions of the research carried out, as well as ideas of future work.

This research work has led to the following journal publications

1. Manan. A, and Cooper. J.E., "Design of Composite Wings Including Uncertainties: A Probabilistic Approach", Journal of Aircraft, 2009, Vol. 46, No. 2, pp. 601-607.
2. Manan. A, Vio. G. A., Harmin. M.Y. and Cooper. J.E, "Optimization of aeroelastic composite structures using

evolutionary algorithms" Accepted in Engineering Optimization Journal.

3. Manan. A, and Cooper. J.E., "Prediction of Uncertain Frequency Response Function Bounds using Polynomial Chaos Expansion". Under review in Journal of Sound and Vibration.
4. Manan. A, and Cooper. J.E., "Robustness Design of Composite Wings for Gust Response". Under review in Aerospace Science and Technology.

In addition, the following are the peer-reviewed conference publications resulting from the present research

1. Manan. A, and Cooper. J.E., "Uncertainty of Composite Wing Aeroelastic Behaviour". 12th AIAA/ISSMO Multidisciplinary Analysis and Optimization Conference, Victoria, British Columbia, Sep. 10-12, 2008.
2. Manan. A, and Cooper. J.E., "Robust Design of Composite Wings for Gust Response" 50th AIAA/ASME/ASCE/AHS/ASC Structures, Structural Dynamics, and Materials Conference, Palm Springs, California, 4-7 May, 2009.
3. Manan. A, and Cooper. J.E., "FRF Uncertainty Bounds prediction using Polynomial Chaos Expansion". 2nd International Conference on Uncertainty in Structural Dynamics, Sheffield, UK, 15-17 June 2009.
4. Manan. A, and Cooper. J.E., " Design of Composite Wing Including Uncertainties" Conference on Aircraft Structural Design, Challenges for the Next Generation- Concept to Disposal, The Forsight Centre, University of Liverpool,UK,14-16 October, 2008.

5. Manan. A, and Cooper. J.E., "Multi-Objective Aeroelastic Tailoring including Uncertainties" CEAS 2009, European Air and Space Conference, Manchester 2009.

Chapter 2

Literature Review

2.1 Introduction

This chapter provides an introduction to the background material and current state of the art to a number of following areas relevant to this thesis.

- Aeroelasticity and Aeroelastic Modelling
- Aeroelastic Tailoring
- Uncertainty Theories and Modelling
- Robust Design Criteria
- Damage and Damage Models

Each section contains brief topic description, their current modelling approaches and applications in the aeroelastic fields.

2.2 Aeroelasticity and Aeroelastic Modelling

Aeroelasticity is the science which addresses the interaction of the aerodynamic, elastic and inertia forces, and the influence of this interaction on the aircraft design and performance[1]. Interaction of various forces and instabilities are highlighted in the Collar's aeroelastic triangle (see Figure 2.1).

In dynamic aeroelasticity, flutter is the critical phenomenon[1, 6-8], which is catastrophic and undesirable. At the flutter speed, violent unstable vibration occurs resulting in the structural failure. Flutter phenomenon occurs due to the interaction of two modes, often predicted from the v-g and v-ω plots as shown in Figure 2.2.

In static aeroelasticity, the forces acting on and the resulting motion of the flexible aircraft are considered time independent. Critical static aeroelastic phenomena are divergence and control reversal[1]. At the divergence speed, the structural stiffness is not enough to sustain the further aerodynamic load or moment and causes the structure to fail. At the control reversal speed, pitching moments generated due to the wing incidence and control surface rotation angles are exactly equal cancelling each other effect making the aileron ineffective. At speeds near to the reversal speed, the aircraft response is either very slow, or not at all, and beyond this speed the opposite response is obtained[1].

Atmospheric turbulence but also gusts and manoeuvres can cause extreme loading and consequently affect the wing fatigue life due to the additional bending moment generated at the root while the induced drag resulting from the aeroelastic shape taken up by wing at the specific flight conditions can influence the aircraft performance or the fuel efficiency[1].

The aeroelastic models required to predict flutter/ divergence speed, gust response or wing aeroelastic shape consist of structural as well as aerodynamic models of various levels of sophistications. Some examples are reviewed in the remaining part of this section.

For vibration tailoring of the composite lifting surfaces, Weisshaar [9] presented the beam and plate models which are characterised by bending stiffness EI, torsional stiffness GJ and bend-torsional stiffness K parameters. In the plate model, the chord-wise rigidity is assumed meaning that stiff and closely spaced ribs are present within the wing. In both the models, infinite stiff vertical shear webs are assumed, which means that the box beam and plate models are composed of two rigidly

attached plates. A beam finite element was developed incorporating these stiffness parameters to predict the free vibration analysis.

Librescu [10]assumed a simple, anisotropic thin-walled beam model to study the aeroelastic lift distribution and the divergence instability of the forward- swept composite wing. The model incorporates anisotropy of the material, transverse shear deformation and warping effects. Moreover, in his model, wing at the root was considered fully restrained against the rigid body motion.

In[11], the laminate plate theory[12] is utilized to calculate the plate stiffness parameters while Rayleigh-Ritz assumed mode shape method is adopted to investigate the effect of stiffness coupling on the aeroelastic flutter and divergence speed of the composite wing idealised as a cantilever plate model. The unsteady, incompressible two-dimensional aerodynamic theory was assumed and the harmonic sinusoidal aerodynamic forces resulting from the pressure distribution (per unit area) produced the aerodynamic matrix of their aeroelastic model.

Lotatti [13] analytically investigated the flutter and divergence speed of a cantilevered, composite, forward swept rectangular wing, for various values of the bend-torsion coupling terms. In his work, the box beam stiffness characteristics were identical to the ref[9], while aerodynamic model assumed the two-dimensional unsteady aerodynamic strip theory.

The wing model can also be developed with the FE technique[14-16]. Various researchers have employed the said modelling technique to study the composite plates/structures vibrational and aeroelastic phenomena[17-20].

In 1980's, the swept forward wing designs [13, 19, 20]were explored by using the composite materials. The research was mainly motivated to exploit the bend-torsion coupling terms provided by these materials.

Later, the double-swept isotropic and composite wings designs (without sacrificing wing aerodynamic benefits) were also explored. In their aeroelastic model, FE technique was used to model the structure whilst the doublet point method was adopted to model the aerodynamics[21]. They found that by optimising the sweptback angle of the inboard wing, flutter and divergence speeds of the isotropic wings could be increased, while for the composite wing, the bend-torsion coupling terms have shown some success.

Some researchers[22, 23] have investigated gust or turbulence as a design criterion for the wing structures. For example, the double-wedged airfoil and supersonic wing structures were optimised under the gust loads constraints [22]. In both the studied examples, the objective was to find the minimum weight design such that value of stress in the wing remains within the prescribed range. Formulated non-linear constraint optimisation problems were then solved by using the finite element and interior penalty function methods.

The Root Bending Moment (RBM) caused by the gust can be alleviated in a passive or an active manner. In the passive approach, either by adopting a passive device [24] or controlling/adjusting the fibre orientation angles [25, 26]in the wing, alleviation of the RBM can be achieved. In these approaches, the RBM is minimised to some or desired extent but with the reduction of the flutter speed. In the active approach, which now becomes an Aero-Servo-Elastic (ASE) problem, wing aileron can be engaged to minimise the RBM due to gust. ASE approach requires designing of a controller for the control surface angle.

The simplistic approach for the controller may assume the control surface demand angle proportional to the wing deflection and velocity(which can be obtained by attaching a sensor in the wing)[1]. Nevertheless, RBM along with the in-flight loads caused due to the manoeuvres is often a critical design load for the wing design.

2.2.1 Summary on Aeroelasticity, modelling and Application

1. Interactions of aerodynamic, inertial and elastic forces give rise to static and dynamic aeroelastic phenomena, which are catastrophic and undesirable. In dynamics aeroelasticity, flutter is the key instability while divergence and aileron reversal are the main static instabilities.
2. Gust or turbulence causes additional RBM, which can be alleviated by adopting the passive and active approaches. In the passive method, either a passive device or adjusting the fibres in the wing, RBM can be minimised. In the active approach, wing aileron can be used to minimise the RBM.
3. The induced drag resulting from the aeroelastic wing shape can influence the aircraft performance and fuel efficiency.
4. Composite materials, due to the bend-torsion coupling terms, can provide flexibility in the aeroelastic designs and in 1980's were explored for the forward-swept wing designs and now being increasingly used in the aerospace industries.
5. Mostly aeroelastic design approaches are the deterministic one and do not include the structural and damage parameter uncertainties.

2.3 Aeroelastic Tailoring and Application

The work here first examines the resizing principle, a traditional approach of increasing the flutter speed. In this approach, the mass and

stiffness of the wing/tail plane panels or mass distribution within the panels is changed. A study adopting this approach was conducted against the strength and flutter constraints to obtain the near-minimum-weight designs of the metallic and composite wings [27]. Particularly for the composite wing design, a 30% increase in the flutter speed was set as an objective after meeting the strength requirements. The wing panel thicknesses were then iteratively varied and finally, with a 4% increase in weight compared with the original strength based wing design, the required increase in the flutter speed was achieved. Similarly, it has also been shown in [1, 28] that by attaching a mass on the leading edge, the flutter speed can be increased.

Aeroelastic tailoring is a rich and well-investigated field and has been defined as [29]

"Aeroelastic tailoring is the embodiment of directional stiffness into an aircraft structural design to control aeroelastic deformation, static or dynamic, in such a fashion as to affect the aerodynamic and structural performance of that aircraft in a beneficial way"

Aeroelastic tailoring approach, using fibre lay-up orientation to control the stiffness cross-coupling terms[30], can provide an alternate solution against the traditional resizing principle to increase the flutter speed and initially brought in to overcome the divergence problems of the forward swept wings. In either of the approaches, the objective is the same i.e. to control the bending and twisting response in the favourable and beneficial manner.

Effect on the static aeroelastic phenomena, such as the divergence speed, change in the centre of pressure and the aileron effectiveness, by varying the fibre orientation angles, was studied for the forward and

sweptback wings[19]. The wings with aspect ratio of 6 and 25 were studied in this regard and it was shown that fibre-tailoring approach improved the divergence speed at a certain level and the rest was achieved at the cost of weight. An aero-isoclinic condition (a condition defined with when wing flex without any change in the centre of pressure and wing lift curve slope compared with its rigid wing) could be achieved with the aeroelastic tailoring approach not only for the forward but also for the sweptback wings[19]. Such a condition can affect the longitudinal aircraft stability (due to change in lift centre of pressure) and wing root stresses (due to change in moment arm of the lift). Furthermore, they demonstrated that aileron effectiveness for the forward swept wing could be enhanced considerably by aligning the fibres towards forward direction from the reference axis (see Figure 2.3 where 'θ' is approximately 125^{o}).

In[31], reduction in the induced drag was demonstrated by using both the aeroelastic tailoring approach and adaptive control surface. The spanwise lift distributions of the wing at high speed, where it was found that the aeroelastic effects were substantial, were reshaped by adjusting the fibre orientation angles to reduce the induced drag. A control surface was also utilised, of which a small input could further provide desired reduction in the induced drag. However, they also found that at some speeds, the controller became ineffective.

Coupled deflection shapes of the wing, which make the wing design either washout or wash-in design (see Figure 2.4), can also be produced by adopting the aeroelastic tailoring approach. Wash-out designs are the one, which decrease the wing effective angle of attack with upward heave, whereas wash-in designs increase the wing effective angle of attack[29].

In [32], the aeroelastic tailoring approach was applied to the aerobatic composite wing design and it was demonstrated that a 30% increase in the flutter speed and a significant decrease in the weight was possible compared with the metallic wing by optimising the wing skins and spars webs.

Aeroelastic Tailoring approach for the high-aspect-ratio (=14) aft-swept wing was explored [33]and it was shown that the advantage of the bend-torsion coupling terms were minimal while torsional stiffness was the most influencing factor for increasing the flutter speed.

Recently, an investigation of the aeroelastic tailoring approach has been conducted on the swept and geometrically tapered wings[18]. For the case of a non-swept uniform wing design, the bend-twist coupling rigidity contributed significantly to increase the flutter speed. The other finding was that the bend-torsion coupling effect was negligible on the flutter speed of the swept and geometrically tapered wings while torsion stiffness was the significant contributing factor. It was also emphasized that, for the case of swept and mass and geometrically tapered wing designs, simplified optimisation problem could be formulated by simply maximizing the torsion stiffness rather than optimising the complicated flutter speed problem.

In a further study, the aeroelastic tailoring approach to design the composite wing [34] against strength, flutter speed, divergence speed, vertical deflection and wing tip twist constraints was investigated. Rayleigh-Ritz energy principle and Vortices Lattice Method (VLM) were employed to formulate the structural and aerodynamic matrices of the wing respectively; and Tsai-Wu failure criterion was considered to indentify failure in the ply.

2.3.1 Summary on Aeroelastic Tailoring

1. Aeroelastic tailoring is a passive approach in which after adjusting the fibre orientation angles in the composite wings, the aeroelastic stability and response can be improved.
2. Such approach provides an alternate solution to the traditional method of resizing in which increase in the flutter speed is achieved by the addition of mass or changing its distribution and/or changing the local structural stiffness values. For example, attaching a mass on the leading edge of the wing, the flutter speed is increased due to the shifting of mass axis towards the leading edge. Similar effects can be achieved by adjusting the fibre orientation angles at the beginning of the design process to increase the flutter speed.
3. Reduction in the induced drag by reshaping the lift curve distribution or optimising the gust response can be achieved via employing the aeroelastic tailoring approach. However, such approach cannot always provide a solution at all speeds, which may be possible by using the adaptive control surface.
4. An aero-isoclinic condition (a condition that is defined with no change in the centre of pressure and wing lift curve slope compared with its rigid wing counterpart when wing is allowed to flex) can be achieved from aeroelastic tailoring for both forward and sweptback wings. Variation in the centre of pressure changes the aircraft longitudinal stability and in turn changes the root bending moment (due to the change in moment arm).
5. For high aspect ratio wings or geometrically tapered wings, the effect of the bend-torsion coupling term is negligible and the torsion stiffness term is the key contributing factor influencing upon the flutter speed.

2.4 Modelling of Uncertainty

Deterministic approaches, by using safety factors and worst-case design scenarios principles to account for uncertainty, are often applied for the design and analysis of the composite structures and consequently produce conservative or unknowingly dangerous designs[35]. Hence, by adopting this approach, uncertainty inherent almost in every design and analysis approach is considered just intuitively. Measurements and observations, however, clearly show their random characteristics. For example, consider a mass-produced fibrous composite part, and due to manufacturing variability, these parts are never identical. The fibre used to manufacture these parts also has variability in the mechanical properties (Young's and shear modulus etc.). It is also a well-known fact that these composite structures tend to absorb moisture (environmental effects[4, 5]), often matrix cracks occur[2-4] and sometimes fibre breakage occurs due to the excessive load and/or fatigue.

These uncertainties can influence significantly the design and analysis process and consequently poses following three key challenges

1. The types of input uncertain models to be chosen(PDF or with small or large value interval bounds)
2. Approaches for the uncertainty propagation
3. Robustness under uncertainties

Various uncertainty theories are available in the literature[36-41] and broadly classified as either probabilistic or non-probabilistic. Such classification is often made because of available information of the uncertain data, for example, if probability density function (PDF) of the uncertain variable(s) is known then probability theory can be applied.

For the cases when data information is imprecise or scarce, and only bounds of uncertain parameters are known, then non-probabilistic theory can be a choice. Under severe uncertainty, information gap theory is applied[37].

Two approaches are reviewed and presented in the thesis, Polynomial Chaos Expansion (PCE) - a probabilistic approach and Interval Analysis- a non-probabilistic approach (as a special case it has been extended to the probabilistic manner).

Probabilistic PCE approach is preferred over other probabilistic methods such as perturbation technique because perturbation method, while predicting the overall response of the system, usually adopt only the first order Taylor series expansion of uncertain parameters as calculation of the higher order terms are computationally inefficient. On the other hand, the PCE approach utilise the orthogonal structure of the polynomials along with higher order terms for efficiently quantifying the uncertainty of the response. Moreover, it is also known that with large variation in uncertain parameters the accuracy of the perturbation model is somewhat compromised whereas in PCE approach, the effects due to large variation can be efficiently captured with the higher order polynomial terms. Furthermore, the inclusion of interaction terms of uncertain parameters in PCE may provide some insight if there is an interaction of the uncertain parameters exist and consequently might affect the overall response of the system.

Uncertainty representation and propagation via PCE

Polynomial chaos is an approach that exploits a polynomial based stochastic space for the uncertainty representation and propagation

defined with the PDFs. Norbert Weiner [42], first introduced this concept by representing the irregularities of the process (such as Brownian motion of the pollen particles on the surface of water) with homogenous chaos.

Ghanem and Spanos [43, 44] proposed a convergent series for the definition of the Polynomial Chaos Expansion (PCE) in the form

$$u(\theta) = a_0\Gamma_0 + \sum_{i1=1}^{\infty} a_{i1}\Gamma_1(\xi_{i1}(\theta)) + \sum_{i1=1}^{\infty}\sum_{i2=1}^{i1} a_{i1i2}\Gamma_2[\xi_{i1}(\theta),\xi_{i2}(\theta)] + \sum_{i1=1}^{\infty}\sum_{i2=1}^{i1}\sum_{i3=1}^{i2} a_{i1i2i3}\Gamma_3[\xi_{i1}(\theta),\xi_{i2}(\theta),\xi_{i3}(\theta)] + \ldots \quad (2.1)$$

in which $\{\xi_{i1}(\theta)\}_1^{\infty}$ denotes a set of independent standard Gaussian random variables and $\Gamma_p[\xi_{i1}(\theta).....\xi_{ip}(\theta)]$ is a set of multidimensional Hermite polynomials of order p, $a_{i1}.....a_{ip}$ are deterministic coefficients and θ is used to represent the randomness.

The shape of the represented PDF of any type of the input uncertain variable is created in the stochastic space with polynomials and if input uncertain random variable is Gaussian, then Hermite polynomials with first two terms are used. For the other types of uncertain random variables [45]see Table 5.1.

The response model, analogous to the input uncertain random variable models, can be defined with the same polynomials but with the inclusion of the higher order terms in order to capture the non-Gaussian response. Such higher-order PCE representation of the uncertainty is computationally efficient compared with the perturbation-based

methods (which usually use the first-order terms because calculation of the higher-order terms are computationally inefficient)[46].

The uncertainty propagation can be made with the sample or non-sample based approaches. In the sample-based approach, samples for the input uncertain are generated, and the regression analysis approach[47] can be adopted to build the response model by solving the simultaneous equations. On the other hand, the Galerkin projection method can be utilised to build the output response model, but such an approach leads to a mathematically complicated systems of the equations to be solved. The other disadvantage of using Galerkin projection method is that it requires modifying the deterministic codes, which are already validated and tested and does not remain an attractive option for the industry.

Uncertainty representation and propagation via IA

When information is imprecise or scarce, an uncertain variable is often defined with an interval, and can be thought of as a new kind of a real number, represented by the pair of the numbers also called as its endpoints[40].

The end points of an uncertain variable, X, often denoted as $\underline{X}$ (lower value of X) and $\overline{X}$ (upper value of X) and in the interval notation can be written as[39, 40]

$$X = \left[\underline{X}, \overline{X}\right] \tag{2.2}$$

The midpoint of an interval can be written as $m(X)=\frac{\left(\underline{X}+\overline{X}\right)}{2}$.

In[48], a concept is presented by combining the first order perturbation and interval mathematics to estimate the upper and lower bounds of the dynamic response. The same dynamic response problem was also handled in a probabilistic manner and it was found that interval approach predicted the larger bounds on the response compared with the probabilistic approach.

A comparison was presented between non-probabilistic interval analysis and probabilistic approach while studying the effects of bounded-but-uncertain parameters on the dynamic response of the system[49]. A simplified difference scheme was utilised to predict the first order derivative of mass, stiffness, damping and force matrices by perturbing the nominal values of the structural parameters by a very small values. They found that tighter bounds on the dynamic responses were produced by the probabilistic approach compared with the non-probabilistic approach[49].

The bounds on the real part of the eigenvalues, for the standard interval eigenvalue problem ($(Q-I\lambda)x_0=0$), can be determined as[40, 48-50]

$$\underline{\lambda_r}=\min_{Q\in Q^I}\left\{\mathrm{Re}\left(\lambda_i(Q)\right)\right\},\qquad \overline{\lambda_r}=\max_{Q\in Q^I}\left\{\mathrm{Re}\left(\lambda_i(Q)\right)\right\} \tag{2.3}$$

where $\underline{Q}\le Q\le\overline{Q}$; $Q\in Q^I=[\underline{Q},\overline{Q}]$.

The equation (2.3) means that for the upper and lower bounds of the real part of eigenvalues, a global optimisation approach is required. This means that finding the $\underline{\lambda_r}$ and $\overline{\lambda_r}$ by solving $(Q-I\lambda)x_0=0$ subject

to $\underline{up_i} \leq up_i \leq \overline{up_i}$, i=1, 2,...,n. Here up_i represents uncertain parameter and n shows their number. This approach gives the accurate bounds of the real part of the eigenvalues; however, it is computationally expensive.

2.4.1 Applications of Uncertainty Approaches in Aeroelasticity

Some work has been undertaken on the influence of uncertainties on aeroelastic behaviour[51-53]. Various sources of uncertainties can potentially complicate aircraft design, testing and certification methods, and some work on quantification of various aeroelastic problems such as flutter flight testing, prediction of Limit Cycle Oscillations (LCO) and design optimization with aeroelastic constraints was studied [51]. The LCO of a rigid pitch-plunge aerofoil incorporating uncertainties in the cubic coefficient of torsional spring and also in initial pitch angle of aerofoil was also investigated[52].

The flutter boundary and LCO behaviour of a metallic wing was studied via the incorporation of stiffness uncertainties and the Karhunen-Loeve (KL) expansion was adopted to define stiffness uncertainties along the span of the wing and perturbation theory was applied to find the response variability[53].

The aeroelastic design optimization with respect to uncertainties in material and structural properties was explored in order to increase the critical airspeed above that of baseline wing structure using mass balancing approach. In this regard, two-step constraint optimisation problems were formulated, in the first step, maximum change (called as a stability margin) in the real part of the flutter mode was determined due to uncertainties. In the next step, after including the stability

margin, the minimum change in the mass by doing mass balancing at twelve locations on the composite wing was performed to achieve the desired flutter speed[28]. However, in their work, the bend-torsion coupling terms were not included in the constraint optimization problems.

A method for the analysis and design of an aeroelastic system subject to the parametric uncertainties via hard inequality constraints requirement has also been proposed. Uncertainty models were defined given by the norm-bounded perturbation from the nominal value (hyper-sphere or hyper-rectangular) and if hard constraints were not satisfied on the surface, the deformation of the hyper-sphere via either expansion or contraction was proposed as a solution[54].

Polynomial Chaos Expansion (PCE) is a method that has been used to explore the variability of response in control [55, 56], computational fluid dynamics [57, 58]and buckling problems [47]. PCE with Latin hyper cube approach was first explored in [47]to analyse the buckling eigenvalues of the joined-wing model. Convergent series of the polynomials defined in[43]were utilised to model the response. Input uncertain variables followed Gaussian distribution, whereas a regression analysis was performed to predict the beta coefficients involved in the response expression via Latin hypercube sampling technique.

The use of PCE for the stability and control of non-linear problems has been found as an efficient method even when other techniques such as Lyapunov's method have failed [55]. The potential of PCE is tremendous because of its simplicity, versatility and computational efficiency within the framework of Probability Theory.

2.4.2 Summary on Uncertainty Theories and Modelling

1. The PCE approach can be applied when PDFs of the uncertain input variables are known, which are represented by taking the representative polynomials defined in the stochastic space.
2. Interval Analysis approach is often applied when only upper and lower bounds of the uncertain parameters are known.
3. In the PCE approach, PDF of the input uncertain parameters can be generated by using the polynomials (for example, in case of Gaussian distribution, hermite polynomials are used) and can be propagated by using the sample or non-sample based approaches to predict bounds on the response.
4. Sampled and non-sampled based PCE approaches have been applied in the fluid mechanics[58], control engineering[56] and the buckling frequencies variations predictions[47] of the structure containing structural parameters uncertainties.

2.5 Robust Design Criteria

A design, which minimises the performance variation without eliminating the uncertainty, is a robust design[59] and is often insensitive to the small changes. Robust design approaches seek to minimize the variation in the system performance about the mean design point[60].

Taguchi[59] first presented the approach for the robust design and later on this approach was explored and extended by the other researchers. The polynomial chaos was utilized to explore the robust aerodynamic design of two-dimensional airfoil[61] in which lift-to-drag ratio was maximised and its sensitivity due to the uncertainty of the leading edge thickness was minimised. In [62] a robust optimal design was explored

for the vibration absorber to miminise the displacement of the system over the large range of excitation frequncies by including the uncertainties in the stiffness and mass properties of the main system. Objective was to determine the stiffness, mass and damping parameters for the robust design of vibration absorber. In the field of aeroelasticity, however, a very less work is published[28, 54].

On the other hand, reliability-based design approaches [35] produce designs by analysing the limit-state-function [63]to meet the reliability requirement defined via reliability index(which is the measure of probability of failure of design). Different methods such as the First Order Reliability Method (FORM)[63], Second Order Reliability Method (SORM) and the Hasofer-Lind method (H-L method) have been used to predict the structural reliability. In the FORM approach, a first order Taylor series expansion of the limit-state-function is used, whereas in the H-L method this search is expanded from the mean of the limit-state-function to the most probable failure point. If the coefficient of variation of the uncertain parameter is large, or the response is non-linear, FORM predicts a poor reliability and also the H-L method does not guarantee convergence [63].

2.6 Damage Models for the Composite Structures

Damage within composite structures can be defined as an accumulation of defects such as matrix cracks, debonding or delamination and fibre fracture[64] as shown in Figure 2.5 and Figure 2.6. To model such damage modes, continuum, micromechanics and macro-mechanics damage principles are generally applied[2, 3].

In the continuum mechanics approach, damage parameters such as matrix cracks, inter-laminar cracking are characterised by a set of

internal state variables, which physically represents damage magnitude and modes[2].

In the micromechanics approach, a detailed micro-field of stress-strain in the vicinity of defect or crack is evaluated and in doing so effective stiffness is predicted; whereas in macro-mechanics such as two-phase or three-phase methods, composite layer is treated as an orthotropic homogenous solid with cracks (which are simulated with inclusions)[3].

In of the stated approaches, the reduced stiffness values or damaged material model of the composite structures is predicted. In the present study, continuum damage and macro-mechanics models are reviewed and employed to predict the damage material models.

2.6.1 Talreja's Formulation- Continuum Damage Model

Talreja [2]utilized the continuum damage approach to describe the effect of damage on the stiffness properties of the composite structures due to the presence of the transverse matrix cracks. The damaged material model proposed was the form [2]

$$E_x = E_x^0 + 2\zeta\left[kc_4 + kc_9(v_{xy}^0)^2 - kc_{17}v_{xy}^0\right]; E_y = E_y^0 + 2\zeta\left[kc_9 + kc_4(v_{xy}^0)^2 - kc_{17}v_{xy}^0\right];$$
$$v_{xy} = v_{xy}^0 + 2\zeta\left[\frac{1 - v_{xy}^0 v_{yx}^0}{E_y^0}\right](kc_{17} - 2kc_9 v_{xy}^0); G_{xy} = G_{xy}^0 + 2\zeta kc_{14} \quad (2.4)$$

where ζ is the non-dimensional crack density($=\frac{t_c}{s}$) and 't_c' and 's' are the thickness of layer and spacing between the adjacent cracks respectively (see Figure 2.7). $E_x^0, E_y^0, G_{xy}^0, v_{xy}^0$ and v_{yx}^0 are the undamaged material properties; and kc_i are constants which are

determined experimentally. Sanders[65]determined these constants experimentally for the graphite/epoxy composites which were kc_4 = -4.323GPa; kc_9 =-2.268 GPa; kc_{17} = -3.889 GPa. The kc_{14} value (which affects the shear modulus) was not determined and in the present study, kc_{14} is assumed equal to zero in equation(2.4), which means that reduction in the shear modulus due to damage is ignored. Nevertheless, such affects can be incorporated in the equation (2.4) for the known kc_{14}. Material properties for the graphite/epoxy composites are given in Table 2.1.

In Talreja Model, based on the continuum model, two key assumptions are made. i.e. the axial displacement component vector on crack is neglected and only the out of plane displacement component is considered. Second assumption is that the cracks are open whereas the closed cracks are assumed as in the undamaged state.

2.6.2 Two Phase Method for fibrous composite Damage

The concept behind this method is illustrated in Figure 2.8 where it is assumed that an inclusion is embedded in an infinite effective homogenous media[3]. In this approach, a crack is represented with an inclusion while consolidated fibres depict a homogenous media. Average strain and hence the effective stiffness of the damaged composite structure is then predicted due to the presence of such cracks. Two phase method[3] is applicable to any laminate geometry containing cracks (see Figure 2.8) and ultimately predicts laminate compliance and stiffness to its reduced value. The procedure defined in [3] is applied to find the damage material model for the various amount of crack density in the present study and key steps are highlighted in Appendix A. In this approach[3], β measure the average distance between cracks (called as

crack density) and the distance for the successive cracks is equal to $\frac{2a}{\beta}$.

Two-phase method is a macro-mechanics approach, in which it is assumed that the open cracks only reduce the effective stiffness of a ply whereas closed cracks do not have any effect on it[3].

2.7 Application of Damage Models in Aeroelastic Field

The investigation of damage effects, on the aeroelastic stability and response of the metallic aircraft structures because of the supersonic speed[66], battlefield [67]or of the fatigue reasons, have been remained a research topic.

In[67], the battle field damage effects on the flutter speed of the optimized metallic wings were investigated. At the damaged locations, the mass and stiffness properties were substituted with values representatives of the values obtained after including the damage.

Research on the stability of the metallic panels with thin cracks exposed in supersonic flow was focused in[66]. They handled the stress singularities occurring at the crack tip by dividing it into two regions at its close proximity. The stiffness, mass and aerodynamic matrices were then derived for the flutter analysis.

Later, the composite materials because of their excellent strength-to-weight ratio and ability to provide bend-torsion coupling terms were explored especially to tailor the fibre orientations in order to enhance the aeroelastic stability[10, 19, 68, 69]. However, the composite materials tend to absorb moistures, often matrix cracks are developed

and sometimes fibre breaks due to the excessive and/or fatigue loads, which in turn can affect the aeroelastic stability and response.

Eastep [70] studied the damaged skin effects on the divergence speed of the forward-swept wing designs that were being explored in 1980's by adopting the aeroelastic tailoring. A built-up metallic wing model with composite skins, which had known damage values and locations, was investigated in this regard. For the damaged skin layers, a complete loss of the material properties was assumed. Four damage locations and 17 different cases were studied, and for the case of the severe damage at the said locations, a ~9% reduction in the divergence speed was predicted.

A one-dimensional finite element model, for the aeroelastic analysis of damaged and undamaged wings defined with the built-up box geometry containing the reinforced stringers, was developed[71]. In their work like [70], the damage layers assumed the complete loss of the stiffness properties while the mass and geometry remained unaffected. They found that un-symmetry caused due to the damage had a detrimental effect on the flutter speed because of simultaneous drop of the extensional, bending and bending-extensional stiffness properties. However, in their model, top and bottom skins were assumed to provide the torsion stiffness and the webs contributions were neglected.

An investigation [72] on the flutter speed of the composite plates containing cracks exposed in the supersonic flow was conducted. The two-phase matrix crack model [3] was adopted to calculate the damaged layers material properties. Reduction in the torsion and bend-torsion stiffness terms, due to the matrix cracks, affected the stability of the studied composite plates considerably.

In [73] the crack-induced effects, located at the trailing edge, on the flutter/divergence speed of an un-swept composite wing was explored. At the crack location, the beam model was divided into two sections and a local flexibility matrix was defined consisting of the bending, torsion and bend-torsion coupling terms. It was found that when the crack was close to the wing root, a more reduction in the flutter and divergence speed was noted.

2.7.1 Summary on Damage Models and their Application

1. The Talreja's Model requires three steps to be followed from which the reduced effective stiffness of composite laminate can be predicted,

    - Utilize equation (2.4)to calculate E_1, E_2, G_{12}, v_{12} in local material axis for any given non-dimensional crack density.
    - Transform these moduli according to the each off-axis ply angle to global axis. This will eventually give us reduced effective stiffness of the damaged composite ply.
    - Perform integration of the composite laminate inclusive of the damage and non-damage layers (based on the location within composite laminate) to predict the total stiffness matrix.
2. In the Talreja model, the effect of crack density on longitudinal Young's modulus is minimal, whereas it lowers the transverse Young's modulus, shear modulus and Poison ratio.
3. Two-phase method follows same three steps already defined in Talreja model to calculate the reduced effective stiffness value of cracked ply. In this method, transverse Young's and shear moduli are reduced to the lower values.

4. Effect of damage on the flutter and divergence speed of the metallic wings and plate models has been explored. In metallic structure, main motivation was to assess the degraded flutter speed either due to battlefield damage or due to excessive loads because of supersonic flow.
5. Effects of the transverse matrix cracks and the damage plies on the flutter/divergence speed of the forward swept and built-up wings with composite skins were investigated.
6. In the published literature, while predicting the effect of damage on the aeroelastic stability and response, known damage locations and values are utilised. No such work exists in which either probabilistic nature of damage or bounded-but-uncertain damage parameter, for example the crack density effects, are explored for the aeroelastic stability analysis.

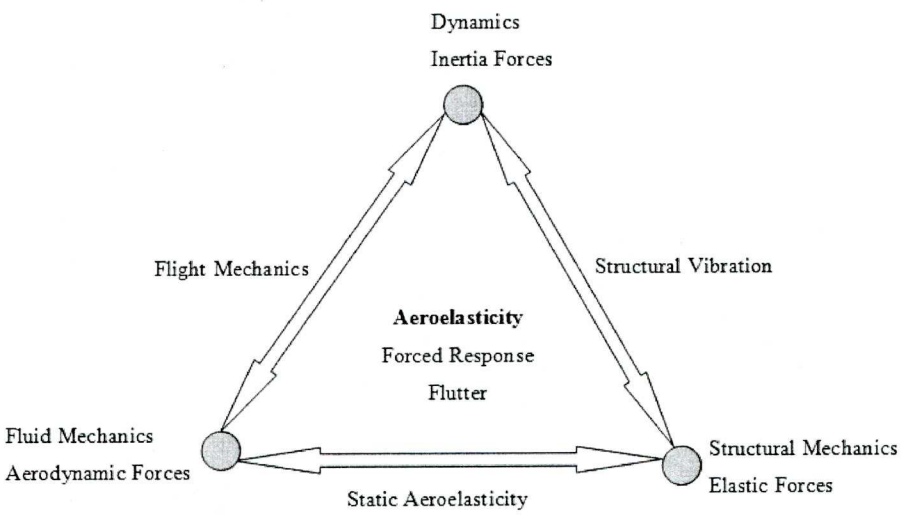

Figure 2.1: Collar's Aeroelastic Triangle[1]

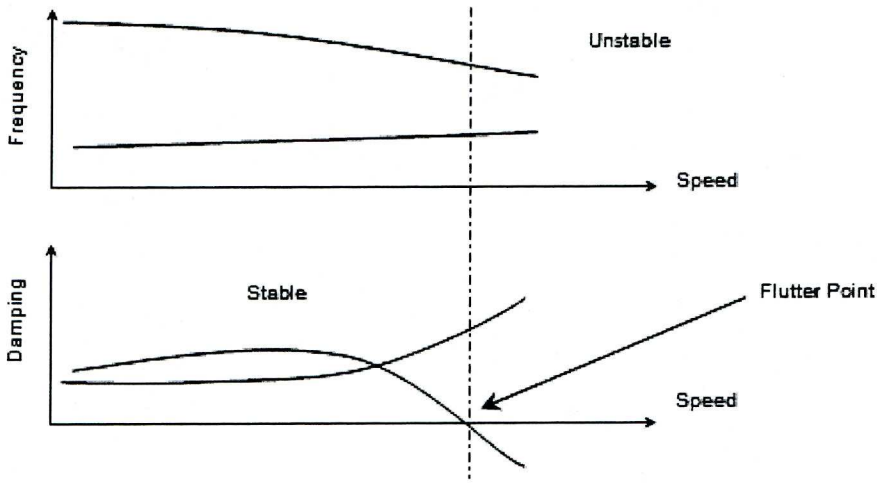

Figure 2.2: Typical v-g and v-ω plots for a binary aeroelastic system

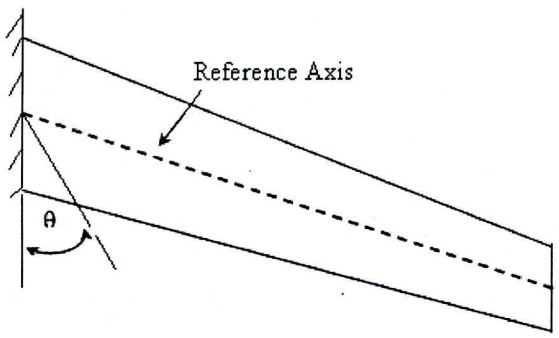

Figure 2.3: Definition of reference axis and fibre angle orientation[19]

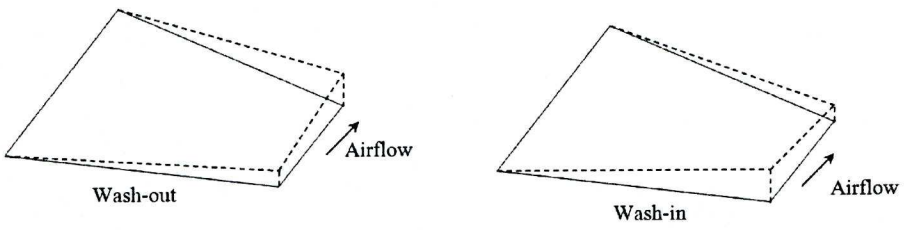

Figure 2.4: Wash-out and wash-in coupled deflection shapes[29]

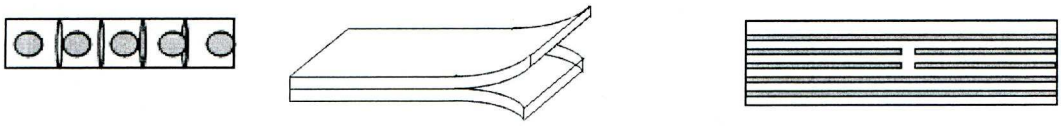

a. Matrix Crack b. Delamination of Two Layers c. Fibre Breakage

Figure 2.5: Various Damage Modes

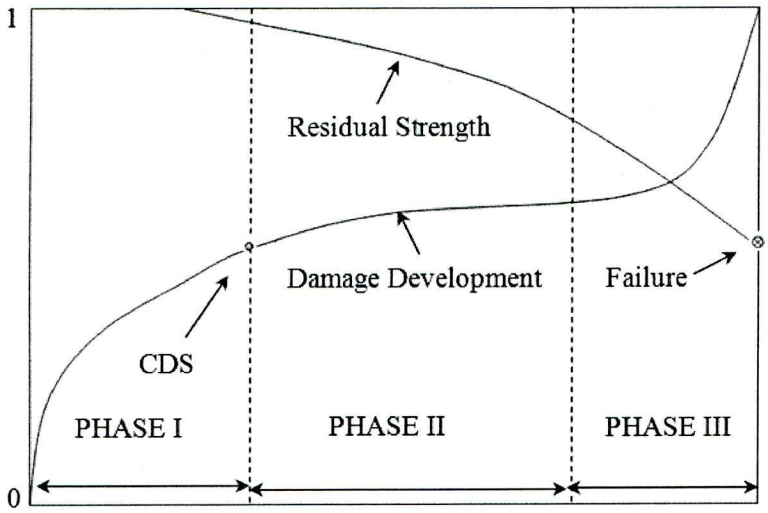

Figure 2.6:Three phase Diagram of Damage modes [64]

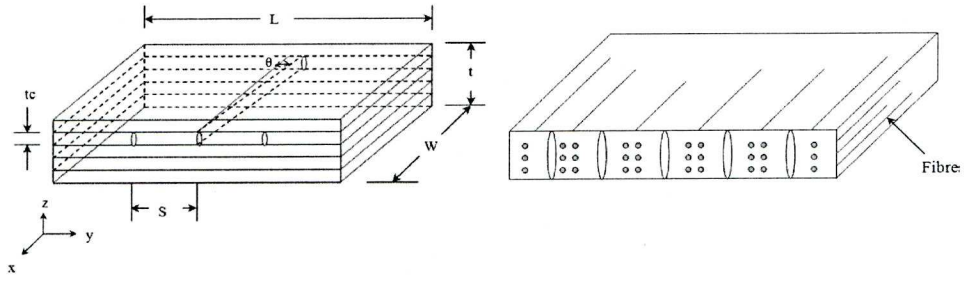

Figure 2.7: Geometrical parameters of composite plate with matrix cracks [2]

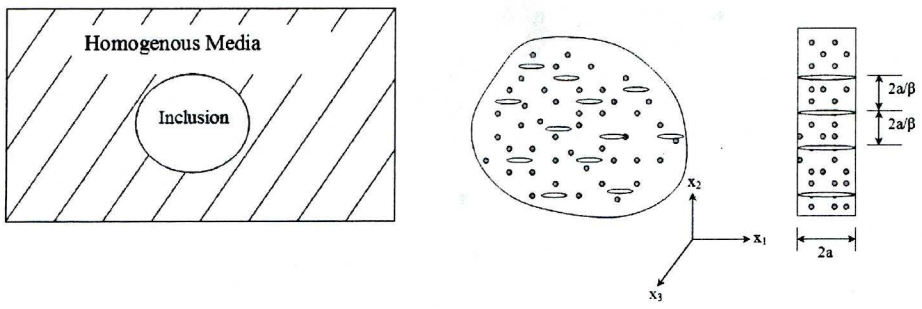

a) Two phase model concept

b) Infinite Fibrous Media with Cracks

Figure 2.8: Two-phase model(After[3])

Property	Values
E_1	136.52(GPa)
E_2	10.0(GPa)
V_{12}	0.3
G_{12}	4.83(GPa)
Ply thickness	0.125 (mm)
Density	1570(Kg/m^3)

Table 2.1: Material properties for Graphite/Epoxy

Chapter 3

Aeroelastic and Aero-Servo-Elastic Modelling of Composite Wings

3.1 Introduction

In this chapter, aeroelastic and aero-servo-elastic models of an idealised composite wing are developed and discussed. Aeroelastic models predict the flutter speed, divergence speed and "1-Cosine" discrete gust response whereas in an aero-servo-elastic model the gust response (i.e. minimise the root bending moment) is controlled in an active manner by engaging the wing aileron. A simplified Proportional and Integral (PI) controller is defined in which a control surface angle is a function of wing deflection and velocity.

Two versions of the aeroelastic models are presented which are based upon the type of aerodynamic model used i.e. unsteady with constant frequency aerodynamics and unsteady with frequency dependent aerodynamics respectively. The 'P-K' frequency matching method [1], is adopted for the solution of the latter case. In the aeroelastic models, the Rayleigh-Ritz energy principles are adopted to model the structure whereas the aerodynamic model is derived using a modified strip theory approach via the torsional velocity term. Making use of the Lagrange's equation by considering the incremental work done over the entire wing due to the lift and the pitching moment (about the flexural axis) eventually yields these mathematical models.

Parametric studies are then conducted to see the effect of fibre orientation angles and material coupling terms on the wind-off frequencies and the flutter/divergence speed.

3.2 Composite Wing Structural Modelling

The composite lifting surface is idealised as a rectangular plate in which the Rayleigh-Ritz assumed modes method [17],which addresses the minimization of energy functional composed of the strain and the kinetic energy, is employed. The strain energy over the entire plate domain Ω as shown in Figure 3.1a can be expressed as

$$U_{strain} = \frac{1}{2}\iiint(\sigma_x\varepsilon_x + \sigma_y\varepsilon_y + \sigma_z\varepsilon_z + \sigma_{xy}\varepsilon_{xy} + \sigma_{xz}\varepsilon_{xz} + \sigma_{yz}\varepsilon_{yz})dxdydz \quad (3.1)$$

which reduces, by taking into account the assumptions that all the transverse and normal stresses are negligible, to

$$U = \frac{1}{2}\iiint_{\Omega}(\sigma_x\varepsilon_x + \sigma_y\varepsilon_y + \sigma_{xy}\varepsilon_{xy})dxdydz \quad (3.2)$$

in which σ_i and ε_i are stress and strain(where $i = x, y, xy$) that are related to each other via the transformed reduced stiffness matrix, $\overline{Q}_{ij}$, by the following relation for each ply 'k' whose positive fibre angle is shown in Figure 3.1b.

$$\begin{bmatrix}\sigma_x\\ \sigma_y\\ \sigma_{xy}\end{bmatrix}_k = \begin{bmatrix}\overline{Q}_{11} & \overline{Q}_{12} & \overline{Q}_{16}\\ \overline{Q}_{12} & \overline{Q}_{22} & \overline{Q}_{26}\\ \overline{Q}_{16} & \overline{Q}_{26} & \overline{Q}_{66}\end{bmatrix}_k \begin{bmatrix}\varepsilon_x\\ \varepsilon_y\\ \varepsilon_{xy}\end{bmatrix} \quad (3.3)$$

Transformed reduced stiffness matrix $\overline{Q_{ij}}$ is related to the stiffness matrix Q_{ij} by the following expression

$$\overline{Q_{ij}} = [T]^{-1} Q_{ij} [T]^{-t} \tag{3.4}$$

in which superscript 't' denote matrix transpose whereas transformation matrix [T] is given by

$$[T] = \begin{pmatrix} (\cos\theta)^2 & (\sin\theta)^2 & 2\sin\theta\cos\theta \\ (\sin\theta)^2 & (\cos\theta)^2 & -2\sin\theta\cos\theta \\ -\sin\theta\cos\theta & \sin\theta\cos\theta & (\cos\theta)^2-(\sin\theta)^2 \end{pmatrix} \tag{3.5}$$

whereas stiffness matrix Q_{ij} has following stiffness terms, which are related to longitudinal Young's modulus (E_1), transverse Young's modulus(E_2), shear modulus(G_{12}) and Poisson ratio(ν_{12})

$$\begin{aligned} Q_{11} &= \frac{E_1}{1-\nu_{12}\nu_{21}}; Q_{12} = \frac{\nu_{12}E_2}{1-\nu_{12}\nu_{21}} = \frac{\nu_{21}E_1}{1-\nu_{12}\nu_{21}} \\ Q_{22} &= \frac{E_2}{1-\nu_{12}\nu_{21}}; Q_{66} = G_{12} \end{aligned} \tag{3.6}$$

Replacing stress relations defined in (3.3) into (3.2), one can obtain strain energy expression of

$$U = \frac{1}{2}\iiint_{\Omega} (\bar{Q}_{11}\varepsilon_x^2 + 2\bar{Q}_{12}\varepsilon_x\varepsilon_y + 2\bar{Q}_{16}\varepsilon_x\varepsilon_{xy} + 2\bar{Q}_{26}\varepsilon_y\varepsilon_{xy} + \bar{Q}_{22}\varepsilon_y^2 + \bar{Q}_{66}\varepsilon_{xy}^2) dxdydz \tag{3.7}$$

which after utilising strain-displacement relations for the pure bending problem reduces to

$$U_{\max} = \frac{1}{2}\iint_{\Omega}\left\{\begin{array}{l} D_{11}\left(\frac{\partial^2 w}{\partial x^2}\right)^2 + 2D_{12}\left(\frac{\partial^2 w}{\partial x^2}\right)\left(\frac{\partial^2 w}{\partial y^2}\right) + D_{22}\left(\frac{\partial^2 w}{\partial y^2}\right)^2 + \ldots \\ 4D_{16}\left(\frac{\partial^2 w}{\partial x^2}\right)\left(\frac{\partial^2 w}{\partial x \partial y}\right) + 4D_{26}\left(\frac{\partial^2 w}{\partial y^2}\right)\left(\frac{\partial^2 w}{\partial x \partial y}\right) + 4D_{66}\left(\frac{\partial^2 w}{\partial x \partial y}\right)^2 \end{array}\right\} dxdy \qquad (3.8)$$

where $D_{ij} = \frac{1}{3}\sum_{k=1}^{n}(\overline{Q}_{ij})_k (z_k^3 - z_{k-1}^3)$ [12] in which the z_k's terms are defined as shown in Figure 3.1c and 'w' is the out of plane deflection of the plate expressed as

$$w = \sum_{1}^{n}\gamma(\xi,\eta)q_i(t) \qquad (3.9)$$

where $q_i(t)$ is the generalised displacement of the ith mode represented with $\gamma(\xi,\eta)$. The strain energy can then be calculated by utilizing equation (3.8) such that

$$U_{\max} = \frac{1}{2}\iint_{\Omega}\left\{\begin{array}{l} \frac{D_{11}}{s^4}\left(\frac{\partial^2\sum_{i=1}^{n} q_i\gamma_i(\xi,\eta)}{\partial\xi^2}\right)^2 + \frac{2D_{12}}{s^2c^2}\left(\frac{\partial^2\sum_{i=1}^{n} q_i\gamma_i(\xi,\eta)}{\partial\xi^2}\right)\left(\frac{\partial^2\sum_{i=1}^{n} q_i\gamma_i(\xi,\eta)}{\partial\eta^2}\right) + \\ \frac{D_{22}}{c^4}\left(\frac{\partial^2\sum_{i=1}^{n} q_i\gamma_i(\xi,\eta)}{\partial\eta^2}\right)^2 + \frac{4D_{16}}{s^3c}\left(\frac{\partial^2\sum_{i=1}^{n} q_i\gamma_i(\xi,\eta)}{\partial\xi^2}\right)\left(\frac{\partial^2\sum_{i=1}^{n} q_i\gamma_i(\xi,\eta)}{\partial\xi\partial\eta}\right) + \\ \frac{4D_{26}}{sc^3}\left(\frac{\partial^2\sum_{i=1}^{n} q_i\gamma_i(\xi,\eta)}{\partial\eta^2}\right)\left(\frac{\partial^2\sum_{i=1}^{n} q_i\gamma_i(\xi,\eta)}{\partial\xi\partial\eta}\right) + \frac{4D_{66}}{s^2c^2}\left(\frac{\partial^2\sum_{i=1}^{n} q_i\gamma_i(\xi,\eta)}{\partial\eta\partial\xi}\right)^2 \end{array}\right\} d\xi d\eta \qquad (3.10)$$

Similarly, the maximum kinetic energy of the entire plate domain Ω can be formulated as

$$T_{\max} = \frac{1}{2}\rho h\omega^2 \iint_{\Omega} w^2(x,y)dxdy \tag{3.11}$$

where ' ρ 'is the mass per unit area of the plate, 'h' is the plate thickness and ' ω ' is the frequency of vibration. By putting expression (3.9) into (3.11), the maximum kinetic energy of the entire plate becomes as

$$T_{\max} = \frac{1}{2}\rho h\omega^2 \iint_{\Omega}\left[\sum_{i=1}^{n} q_i\gamma_i(\xi,\eta)\right]^2 d\xi d\eta \tag{3.12}$$

Minimization of the functional $(U_{\max} - T_{\max})$ with respect to each coefficient q_i results in the following general expressions for the elements of stiffness (E_{ij}) and mass (A_{ij}) matrices respectively,

$$E_{ij} = \iint_{\Omega}\begin{Bmatrix} D_{11}\dfrac{\partial^2\gamma_i}{\partial\xi^2}\dfrac{\partial^2\gamma_j}{\partial\xi^2} + D_{12}\dfrac{\partial^2\gamma_i}{\partial\eta^2}\dfrac{\partial^2\gamma_j}{\partial\xi^2} + 2D_{16}\dfrac{\partial^2\gamma_i}{\partial\xi\partial\eta}\dfrac{\partial^2\gamma_j}{\partial\xi^2} + \ldots \\ D_{12}\dfrac{\partial^2\gamma_i}{\partial\xi^2}\dfrac{\partial^2\gamma_j}{\partial\eta^2} + D_{22}\dfrac{\partial^2\gamma_i}{\partial\eta^2}\dfrac{\partial^2\gamma_j}{\partial\eta^2} + 2D_{26}\dfrac{\partial^2\gamma_i}{\partial\xi\partial\eta}\dfrac{\partial^2\gamma_j}{\partial\eta^2} + \ldots \\ 2D_{16}\dfrac{\partial^2\gamma_i}{\partial\xi^2}\dfrac{\partial^2\gamma_j}{\partial\xi\partial\eta} + 2D_{26}\dfrac{\partial^2\gamma_i}{\partial\eta^2}\dfrac{\partial^2\gamma_j}{\partial\xi\partial\eta} + 2D_{66}\dfrac{\partial^2\gamma_i}{\partial\xi\partial\eta}\dfrac{\partial^2\gamma_j}{\partial\xi\partial\eta} \end{Bmatrix} d\xi d\eta \tag{3.13}$$

$$A_{ij} = \iint_{\Omega}\rho h\gamma_i\gamma_j d\xi d\eta \tag{3.14}$$

where i=1,2,3,..., modes and j=1,2,3...,modes, for the case when modes=9, [E] and [A] will be of 9x9 matrices.

The symbolic tool box available in Matlab was utilized to calculate the [D] matrix for any generic layup-configuration involved in the equation (3.13). Two unique bend-twist coupling terms exist in [D] matrix i.e. one in the span-wise direction (D_{16}) and other in the chord-wise

direction (D_{26}). Whereas these coupling terms do not exist for conventional metals (See Table 3.1 for composite material properties and Table 3.2 for the case of composite and Aluminium plate).

The sign of D_{16} and D_{26} terms are extremely important as they affect the composite laminate a wash-in or wash-out behaviour. For example, wash-out designs (against some gust) may be called as the passive gust alleviated designs (i.e. when wing bends due to an aerodynamic load, the effective angle of attack is lowered as the leading edge deflects more in the downward direction relative to the trailing edge). Such composite designs are discussed in detail in Chapter 4 on aeroelastic tailoring.

The definition of the mode shapes is the other requirement to formulate the stiffness (E) and the mass (A) matrices and are defined in the following section.

3.2.1 Mode Shapes for the Flexible Composite Wing

Simplified polynomial functions are used to represent the mode shapes of the flexible composite wing. Consider a point P(x, y) on the surface of the wing (see Figure 3.2), the out of plane deflection of which in z-axis can be represented by the following expression (only nine terms are considered)

$$w = x^2 q_1 + x^2 (y - y_f) q_2 + x^2 (y - y_f)^2 q_3 + x^3 q_4 + x^3 (y - y_f) q_5 + x^3 (y - y_f)^2 q_6 + \ldots \\ x^4 q_7 + x^4 (y - y_f) q_8 + x^4 (y - y_f)^2 q_9 \qquad (3.15)$$

in which

- x^2, x^3, x^4 simulates the wing bending
- $x^2(y - y_f), x^3(y - y_f), x^4(y - y_f)$ simulates the wing torsion and

- $x^2(y-y_f)^2, x^3(y-y_f)^2, x^4(y-y_f)^2$ simulates the wing chord-wise bending.

Generalisation of these terms take the form of

- $x^2, x^3, x^4 \ldots x^i$ simulates the wing bending (where i=2,3,4,5…) and
- $x^2(y-y_f), x^3(y-y_f), x^4(y-y_f) \ldots x^i(y-y_f)^j$ simulates the wing torsion (where i=2,3,4,5… and j=1) and
- $x^2(y-y_f)^2, x^3(y-y_f)^2, x^4(y-y_f)^2 \ldots x^i(y-y_f)^j$ simulates the wing chord-wise bending(where i=2,3,4,5… and j=2,3..).

The chord-wise bending terms become important for the wing without which discrepancies in the torsion mode may be noted[74].

Equation of motion can be derived by utilising the Lagrange's equations, which can be expressed as[1]

$$\frac{d}{dt}\left(\frac{\partial T}{\partial \dot{q}}\right) - \frac{\partial T}{\partial q} + \frac{\partial \Im}{\partial \dot{q}} + \frac{\partial U}{\partial q} = Q \tag{3.16}$$

where T, U, $\Im$ and Q are the kinetic energy, the strain energy, the dissipative function and the generalised forces respectively. For the free un-damped case, the equation of motion derived from equation (3.16) reduces to

$$A\underline{\ddot{q}} + E\underline{q} = \underline{0} \tag{3.17}$$

Let us assume $q(t) = q_0 e^{i\omega t} \Rightarrow \ddot{q} = -\omega^2 q_0 e^{i\omega t}$,then equation (3.17) becomes the classical eigenvalue problem as

$$(E-\omega^2 A)\underline{X}=0 \tag{3.18}$$

where the stiffness (E) and mass (A) matrices are calculated from the equations (3.13) and (3.14) respectively. The solution to equation(3.18) produces the wind-off frequencies and the mode shapes.

3.2.2 Studied Wing Models

Four types of wing models are studied in the present thesis comprising of the two types of plate wing models, the Goland wing model and the full-scale aircraft composite wing model. Plate wing model are catagorised based on the aspect ratio.

Wing Model 1

Wing model 1 is a plate wing model with an aspect ratio of eight. For this wing, chord is 76.2mm and span is 304.8 mm (see Figure 3.1 and Figure 3.2). Fibre angle in the counter clockwise direction is assumed positive.

Wing Model 2

Wing model 2 is a plate wing model with an aspect ratio of towelve. For this wing, chord is 100 mm and span is 600 mm.

Wing Model 3

Wing model 3 is the Goland wing model. The wing has upper and lower skins, three spars, eleven ribs, three spar caps, eleven rib caps and 33 posts (1-D elements). FE model of the Goland wing is shown in Figure 3.3.

Wing Model 4

The composite wing model 4, which is the full-scale aircraft composite wing model, is shown in Figure 3.4 in which its semi-span, sweep angle, root and tip chords are defined. The thickness-to-chord ratio for this wing is 4 percent in which a geometrical box is fitted, and the front spar, rear spar, top skin and bottom skin form the wing box as shown in Figure 3.5 . The box was positioned in the wing aerofoil such that its front spar lies at the quarter chord and the rear spar lies at the quarter chord from the leading edge. Ten ribs form the other part of the wing structure, provide the chord-wise stiffness and suppress the local panel modes.

Local axes were defined to give definition to the fibre angle for the front spar, rear spar, top skin, bottom skin and ribs, for example, the x-y axis shown in Figure 3.5 is used to define top skin and bottom skin fibre angle, which is positive from x-axis to y-axis in anti-clockwise direction. The lay-up scheme and material properties are given in Table 3.3 and Table 2.1 respectively.

3.2.3 Validation of the Composite Wing Vibration Model

In this section, a convergence study is conducted for the first three frequency values [74]of the composite plate wing model 1 by varying number of bending and torsion modes. Effects of after inclusion of chord-wise bending terms on these frequency values are also studied. Two test cases are studied in this regard i.e. case1=$(0/0/90)_s$ and case2=$(45/45/0)_s$. Bend-twist coupling terms are present for the case2 and are non-existent for the case1. Reference [74] frequency values for the case1 are 11.1Hz, 39.5 Hz and 69.5 Hz whereas for the case2 these

values are 4.9Hz, 30.1Hz and 49.4 Hz. In the present model, the chord-wise bending terms has no effect on the frequency values for the case1. However, for the case 2 these have a significant affect. It can be concluded that for lay-up scheme that has the bend-twist coupling terms, the chord-wise bending terms must be included. It is these coupling terms, which provide the design flexibility and not present in metals.

The developed model was now tested to assess its accuracy against a reference model. Material properties used are given in Table 3.1. Error in predicted results is within 1.5% for the torsion mode and <1% for the bending modes (shown in Table 3.5). The developed model also has an advantage over the reference Finite Element Model in terms of the required number of degrees of freedom, which are far less (36 degrees of freedom or 36 modes for the present case and 365 degrees of freedom for the reference case).

3.3 Parametric Study on Composite Wing Vibration

Here the effect of the fibre orientation angles on the composite wing model 1 on the first three frequencies is explored (without specifically focusing on the torsion frequency). For example, consider a composite wing of six layers, the angle of each layer is 'θ' whereas lay-up configuration is represented with $\left((\theta)_3\right)_s$. In this example, the fibre orientation angle θ is a variable and is allowed to vary from -90° to +90°.

3.3.1 Frequencies Results of the Composite Wing Model

Frequency results are shown in Figure 3.6a whereas various stiffness terms variation plots are shown in Figure 3.6b. The 1st and 3rd

frequencies decrease with increase of the fibre angle (i.e. from 0^o to 90^o) whereas the 2^{nd} frequency shows a slight increasing trend to 15^o fibre angle and beyond this fibre angle it decreases. The main reason for this trend is the reduction of the span-wise stiffness term D_{11}, which becomes minimum for the 90^o fibre angle, for at this angle all the fibres aligned in the chord-wise direction.

The 1^{st}, 2^{nd} and 3^{rd} frequencies are same both for positive $(+\theta_3)_s$ and negative $(-\theta_3)_s$ lay-up configurations, despite the fact that the signs of D_{16} and D_{26} terms are opposite, obvious as it is symmetric until the airflow acts.

$(30^o/30^o/30^o)_s$ and $(-30^o/-30^o/-30^o)_s$ lay-up configurations exhibited maximum span-wise bend-twist coupling term D_{16} and $(60^o/60^o/60^o)_s$ and $(-60^o/-60^o/-60^o)_s$ lay-up configurations exhibited maximum chord-wise bend-twist coupling term D_{26} which was higher than the in-plane shear stiffness terms (D_{66}) which mainly governs the torsion frequency. The sign of these coupling terms contributes significantly to the aeroelastic response and are responsible for the wash-in and the washout phenomenon. Such designs are discussed in detail in Chapter 4 on aeroelastic tailoring.

3.4 Steady and Unsteady Aerodynamics

The aerodynamic model (required for the aeroelastic analysis) can be either steady or unsteady depending upon the aerodynamic theory used. Static aeroelasticity requires steady analysis whereas unsteady aerodynamics must be used for dynamic aeroelasticity. Consider a case when an aerofoil is harmonically oscillating (in heave and/or pitch) relative to the upstream flow, forces and moments acting on it varies with time. In the quasi-steady assumption, these forces and moments

can be calculated by assuming that the aerodynamic characteristics of this airfoil can be substituted at any instant of time by the aerodynamics characteristics of the same aerofoil moving with constant velocity equal to the actual instantaneous values [8]. Because of this assumption, frequency-dependent effects are ignored and this quasi-steady model when applied for the flutter speed prediction does not provide sufficient accuracy. More advanced unsteady aerodynamic models have to be adopted in which the aerodynamic forces and moments are frequency dependent of the dynamic motions of the aerofoil. With this assumption, the lift magnitude changes and phase lag in the aerofoil motion and the unsteady forces exist, whereas for the quasi-steady case these are always in phase.

For harmonically oscillating aerofoil, the lift and moment are often written as [75]

$$L = \rho V^2 \left(L_z z + L_{\dot{z}} \frac{b\dot{z}}{V} + L_\theta b\theta + L_{\dot{\theta}} \frac{b^2\dot{\theta}}{V} \right),$$
$$M = \rho V^2 \left(M_z z + M_{\dot{z}} \frac{b^2\dot{z}}{V} + M_\theta b^2\theta + M_{\dot{\theta}} \frac{b^3\dot{\theta}}{V} \right) \tag{3.19}$$

where 'z' and 'θ' terms involved are shown in Figure 3.7. Unsteady aerodynamic derivative $M_{\dot{\theta}}$ contributes/effects significantly [75] in flutter prediction and will be incorporated in aerodynamic model. When $M_{\dot{\theta}}$ is zero, it is often called Quasi-steady aerodynamics (frequency independent aerodynamics), whereas $M_{\dot{\theta}}$ term can be treated as a constant value (=-1.2) or can be function of the reduced frequency (k) such that [1]

$$M_{\dot{\theta}} = -\frac{5}{2+5k} \tag{3.20}$$

and aerodynamics becomes frequency dependent. The reduced frequency (k) is often defined as [1]

$$k = \frac{\omega c}{2V} \tag{3.21}$$

where 'c' and 'V' are chord and the speed of the wing respectively. For the case, when M_{θ} is a function of the reduced frequency, often frequency matching methods such as 'P-K' method [1] is employed for the flutter prediction.

3.5 Aerodynamic Modelling- Strip Theory

Strip theory divides the wing into infinitesimal strips on which lift acting on the quarter chord is assumed to be proportional to dynamic pressure, local angle of attack, lift curve slope and downwash due to the vertical motion. Although the effective local angle of attack will change due to the chord-wise bending assumption (chord-wise bending terms are required in order to have the correct torsion frequency, see section3.2.3), but the change in the local angle of attack because of this assumption is assumed negligible. Consequently, zeros can be placed corresponding to the relevant rows and columns of the aerodynamic matrices.

Strip theory approach with modified unsteady aerodynamics having $M_{\dot{\theta}}$ term (a torsional velocity term) is employed to formulate the aerodynamic model. Recall the out of plane deflection 'w' of the wing, which is represented with

$$w = x^2 q_1 + x^2 (y - y_f) q_2 + x^2 (y - y_f)^2 q_3 + x^3 q_4 + x^3 (y - y_f) q_5 + \ldots$$
$$x^3 (y - y_f)^2 q_6 + x^4 q_7 + x^4 (y - y_f) q_8 + x^4 (y - y_f)^2 q_9 \quad (3.22)$$

The lift on each strip, having width of 'dx', of the wing can be expressed as

$$dL = \frac{1}{2} \rho V^2 c dx a_w \left\{ \frac{x^2 q_1^{\bullet}}{V} + \frac{x^3 q_4^{\bullet}}{V} + \frac{x^4 q_7^{\bullet}}{V} + x^2 q_2 + x^3 q_5 + x^4 q_8 \right\} \quad (3.23)$$

and the moment about the flexural axis can be written as

$$dM = (dL)(ec)$$
$$= \frac{1}{2} \rho V^2 e c^2 a_w dx \left\{ \frac{x^2 q_1^{\bullet}}{V} + \frac{x^3 q_4^{\bullet}}{V} + \frac{x^4 q_7^{\bullet}}{V} + x^2 q_2 + x^3 q_5 + x^4 q_8 \right\} + \frac{M_{\theta^{\bullet}} c}{4V} \left\{ x^2 q_2^{\bullet} + x^3 q_5^{\bullet} + x^4 q_8^{\bullet} \right\} \quad (3.24)$$

where $\frac{x^2 q_1^{\bullet}}{V} + \frac{x^3 q_4^{\bullet}}{V} + \frac{x^4 q_7^{\bullet}}{V}$ is the effective heave velocity, which is positive downward and $M_{\theta^{\bullet}}$ is a negative term and provides damping to the pitching terms.

The incremental work done over the wing for small deformation of $\delta q_1, \delta q_2, \delta q_4, \delta q_5, \delta q_7$ *and* δq_8 can be written as

$$\delta W = \int_{wing} dL \left(-x^2 \delta q_1 - x^3 \delta q_4 - x^4 \delta q_7 \right) + dM \left(x^2 \delta q_2 + x^3 \delta q_5 + x^4 \delta q_8 \right) \quad (3.25)$$

The generalised forces Q_{q1}, Q_{q2}, $Q_{q3}, Q_{q4}, Q_{q5}, Q_{q6}, Q_{q7}, Q_{q8}$ and Q_{q9} are calculated as

$$Q_{q1} = \frac{\partial}{\partial}\frac{\delta W}{\delta q_1} = \int_0^s \left(-x^2 dL\right)$$

$$= -\frac{1}{2}\rho V^2 c a_w \int_0^s x^2 \left\{\frac{x^2 q_1^{\bullet}}{V} + \frac{x^3 q_4^{\bullet}}{V} + \frac{x^4 q_7^{\bullet}}{V} + x^2 q_2 + x^3 q_5 + x^4 q_8\right\} dx \qquad (3.26)$$

$$= -\frac{1}{2}\rho V^2 c a_w \left\{\frac{s^5 q_1^{\bullet}}{5V} + \frac{s^6 q_4^{\bullet}}{6V} + \frac{s^7 q_7^{\bullet}}{7V} + \frac{s^5}{5} q_2 + \frac{s^6}{6} q_5 + \frac{s^7}{7} q_8\right\}$$

$$Q_{q2} = \frac{\partial}{\partial}\frac{\delta W}{\delta q_2} = \int_0^s \left(\begin{array}{l} \frac{1}{2}\rho V^2 e c^2 a_w \left\{\frac{x^2 q_1^{\bullet}}{V} + \frac{x^3 q_4^{\bullet}}{V} + \frac{x^4 q_7^{\bullet}}{V} + x^2 q_2 + x^3 q_5 + x^4 q_8\right\} + \\ \frac{1}{2}\rho V^2 e c^2 a_w \left\{\frac{M_{\theta^{\bullet}} c}{4V}\left(x^2 q_2^{\bullet} + x^3 q_5^{\bullet} + x^4 q_8^{\bullet}\right)\right\} \end{array}\right) x^2 dx \qquad (3.27)$$

$$= \frac{1}{2}\rho V^2 e c^2 a_w \left\{\begin{array}{l} \left\{\frac{s^5 q_1^{\bullet}}{5V} + \frac{s^6 q_4^{\bullet}}{6V} + \frac{s^7 q_7^{\bullet}}{7V} + \frac{s^5}{5} q_2 + \frac{s^6}{6} q_5 + \frac{s^7}{7} q_8\right\} + \\ \frac{M_{\theta^{\bullet}} c}{4V}\left\{\frac{s^5 q_2^{\bullet}}{5} + \frac{s^6 q_5^{\bullet}}{6} + \frac{s^7 q_8^{\bullet}}{7}\right\} \end{array}\right\}$$

$$Q_{q3} = \frac{\partial}{\partial}\frac{\delta W}{\delta q_3} = 0 \qquad (3.28)$$

$$Q_{q4} = \frac{\partial}{\partial}\frac{\delta W}{\delta q_4} = \int_0^s \left(\frac{1}{2}\rho V^2 c a_w \left\{\frac{x^2 q_1^{\bullet}}{V} + \frac{x^3 q_4^{\bullet}}{V} + \frac{x^4 q_7^{\bullet}}{V} + x^2 q_2 + x^3 q_5 + x^4 q_8\right\}\right) x^3 dx \qquad (3.29)$$

$$= \frac{1}{2}\rho V^2 c a_w \left\{\frac{s^6 q_1^{\bullet}}{6V} + \frac{s^7 q_4^{\bullet}}{7V} + \frac{s^8 q_7^{\bullet}}{8V} + \frac{s^6}{6} q_2 + \frac{s^7}{7} q_5 + \frac{s^8}{8} q_8\right\}$$

$$Q_{q5} = \frac{\partial}{\partial}\frac{\delta W}{\delta q_5} = \int_0^s \left(\begin{array}{l} \frac{1}{2}\rho V^2 e c^2 a_w \left\{\frac{x^2 q_1^{\bullet}}{V} + \frac{x^3 q_4^{\bullet}}{V} + \frac{x^4 q_7^{\bullet}}{V} + x^2 q_2 + x^3 q_5 + x^4 q_8\right\} + \\ \frac{1}{2}\rho V^2 e c^2 a_w \left\{\frac{M_{\theta^{\bullet}} c}{4V}\left(x^2 q_2^{\bullet} + x^3 q_5^{\bullet} + x^4 q_8^{\bullet}\right)\right\} \end{array}\right) x^3 dx \qquad (3.30)$$

$$= \frac{1}{2}\rho V^2 e c^2 a_w \left\{\begin{array}{l} \left\{\frac{s^6 q_1^{\bullet}}{6V} + \frac{s^7 q_4^{\bullet}}{7V} + \frac{s^8 q_7^{\bullet}}{8V} + \frac{s^6}{6} q_2 + \frac{s^7}{7} q_5 + \frac{s^8}{8} q_8\right\} + \\ \frac{M_{\theta^{\bullet}} c}{4V}\left\{\frac{s^6 q_2^{\bullet}}{6} + \frac{s^7 q_5^{\bullet}}{7} + \frac{s^8 q_8^{\bullet}}{8}\right\} \end{array}\right\}$$

$$Q_{q6} = \frac{\partial}{\partial}\frac{\delta W}{\delta q_6} = 0 \tag{3.31}$$

$$\begin{aligned} Q_{q7} &= \frac{\partial}{\partial}\frac{\delta W}{\delta q7} = \int_0^s \left(-x^4 dL\right) \\ &= -\frac{1}{2}\rho V^2 c a_w \int_0^s x^4 \left\{\frac{x^2 q_1^{\bullet}}{V} + \frac{x^3 q_4^{\bullet}}{V} + \frac{x^4 q_7^{\bullet}}{V} + x^2 q_2 + x^3 q_5 + x^4 q_8\right\} dx \\ &= -\frac{1}{2}\rho V^2 c a_w \left\{\frac{s^7 q_1^{\bullet}}{7V} + \frac{s^8 q_4^{\bullet}}{8V} + \frac{s^9 q_7^{\bullet}}{9V} + \frac{s^7}{7} q_2 + \frac{s^8}{8} q_5 + \frac{s^9}{9} q_8\right\} \end{aligned} \tag{3.32}$$

$$Q_{q8} = \frac{\partial}{\partial}\frac{\delta W}{\delta q_8} = \int_0^s \left\{\begin{array}{l} \frac{1}{2}\rho V^2 e c^2 a_w \left\{\frac{x^2 q_1^{\bullet}}{V} + \frac{x^3 q_4^{\bullet}}{V} + \frac{x^4 q_7^{\bullet}}{V} + x^2 q_2 + x^3 q_5 + x^4 q_8\right\} + \\ \frac{1}{2}\rho V^2 e c^2 a_w \left\{\frac{M_{\theta^{\bullet}} c}{4V}\left(x^2 q_2^{\bullet} + x^3 q_5^{\bullet} + x^4 q_8^{\bullet}\right)\right\} \end{array}\right\} x^4 dx \tag{3.33}$$

$$= \frac{1}{2}\rho V^2 e c^2 a_w \left\{\begin{array}{l} \left\{\frac{s^7 q_1^{\bullet}}{7V} + \frac{s^8 q_4^{\bullet}}{8V} + \frac{s^9 q_7^{\bullet}}{9V} + \frac{s^7}{7} q_2 + \frac{s^8}{8} q_5 + \frac{s^9}{9} q_8\right\} + \\ \frac{M_{\theta^{\bullet}} c}{4V}\left\{\frac{s^7 q_2^{\bullet}}{7} + \frac{s^8 q_5^{\bullet}}{8} + \frac{s^9 q_8^{\bullet}}{9}\right\} \end{array}\right\}$$

$$Q_{q9} = \frac{\partial}{\partial}\frac{\delta W}{\delta q_9} = 0 \tag{3.34}$$

Here $q_i^{\bullet}$ form [B] and q_i form [C] matrices, where i=1, 2, 3....9 and are written as

$$[B]=\begin{bmatrix}
\frac{s^5 c a_w}{(2)(5)} & 0 & 0 & \frac{s^6 c a_w}{(2)(6)} & 0 & 0 & \frac{s^7 c a_w}{(2)(7)} & 0 & 0 \\
\frac{s^5 e c^2 a_w}{(2)(5)} & \frac{M_0 c}{4}\frac{s^5 e c^2 a_w}{(2)(5)} & 0 & \frac{s^6 e c^2 a_w}{(2)(6)} & \frac{M_0 c}{4}\frac{s^6 e c^2 a_w}{(2)(6)} & 0 & \frac{s^7 e c^2 a_w}{(2)(7)} & \frac{M_0 c}{4}\frac{s^7 e c^2 a_w}{(2)(7)} & 0 \\
0 & 0 & 0 & 0 & 0 & 0 & 0 & 0 & 0 \\
\frac{s^6 c a_w}{(2)(6)} & 0 & 0 & \frac{s^7 c a_w}{(2)(7)} & 0 & 0 & \frac{s^8 c a_w}{(2)(8)} & 0 & 0 \\
\frac{s^6 e c^2 a_w}{(2)(6)} & \frac{M_0 c}{4}\frac{s^6 e c^2 a_w}{(2)(6)} & 0 & \frac{s^7 e c^2 a_w}{(2)(7)} & \frac{M_0 c}{4}\frac{s^7 e c^2 a_w}{(2)(7)} & 0 & \frac{s^8 e c^2 a_w}{(2)(8)} & \frac{M_0 c}{4}\frac{s^8 e c^2 a_w}{(2)(8)} & 0 \\
0 & 0 & 0 & 0 & 0 & 0 & 0 & 0 & 0 \\
\frac{s^7 c a_w}{(2)(7)} & 0 & 0 & \frac{s^8 c a_w}{(2)(8)} & 0 & 0 & \frac{s^9 c a_w}{(2)(9)} & 0 & 0 \\
\frac{s^7 e c^2 a_w}{(2)(7)} & \frac{M_0 c}{4}\frac{s^7 e c^2 a_w}{(2)(7)} & 0 & \frac{s^8 e c^2 a_w}{(2)(8)} & \frac{M_0 c}{4}\frac{s^8 e c^2 a_w}{(2)(8)} & 0 & \frac{s^9 e c^2 a_w}{(2)(9)} & \frac{M_0 c}{4}\frac{s^9 e c^2 a_w}{(2)(9)} & 0 \\
0 & 0 & 0 & 0 & 0 & 0 & 0 & 0 & 0
\end{bmatrix} \quad (3.35)$$

$$[C]=\begin{bmatrix}
0 & \frac{s^5 c a_w}{(2)(5)} & 0 & 0 & \frac{s^6 c a_w}{(2)(6)} & 0 & 0 & \frac{s^7 c a_w}{(2)(7)} & 0 \\
0 & -\frac{s^5 e c^2 a_w}{(2)(5)} & 0 & 0 & -\frac{s^6 e c^2 a_w}{(2)(6)} & 0 & 0 & -\frac{s^7 e c^2 a_w}{(2)(7)} & 0 \\
0 & 0 & 0 & 0 & 0 & 0 & 0 & 0 & 0 \\
0 & \frac{s^6 c a_w}{(2)(6)} & 0 & 0 & \frac{s^7 c a_w}{(2)(7)} & 0 & 0 & \frac{s^8 c a_w}{(2)(8)} & 0 \\
0 & -\frac{s^6 e c^2 a_w}{(2)(6)} & 0 & 0 & -\frac{s^7 e c^2 a_w}{(2)(7)} & 0 & 0 & -\frac{s^8 e c^2 a_w}{(2)(8)} & 0 \\
0 & 0 & 0 & 0 & 0 & 0 & 0 & 0 & 0 \\
0 & \frac{s^7 c a_w}{(2)(7)} & 0 & 0 & \frac{s^8 c a_w}{(2)(8)} & 0 & 0 & \frac{s^9 c a_w}{(2)(9)} & 0 \\
0 & -\frac{s^7 e c^2 a_w}{(2)(7)} & 0 & 0 & -\frac{s^8 e c^2 a_w}{(2)(8)} & 0 & 0 & -\frac{s^9 e c^2 a_w}{(2)(9)} & 0 \\
0 & 0 & 0 & 0 & 0 & 0 & 0 & 0 & 0
\end{bmatrix} \quad (3.36)$$

[B] is the aerodynamic damping and [C] is the aerodynamic stiffness matrix respectively. Both matrices are non-symmetric and presence of coupling terms help flutter to occur.

3.6 Aeroelastic Model and Eigenvalue Solution

Once the structural and aerodynamic matrices are known, then Lagrange forms the equations of motion, via the generalised force terms $Q=\frac{\partial}{\partial}\frac{(\delta W)}{(\delta q_i)}$ [1]

$$A\ddot{\underline{q}}+(\rho VB+D)\dot{\underline{q}}+\left(\rho V^2C+E\right)\underline{q}=\underline{0} \quad (3.37)$$

where [A], [B], [C], [D] and [E] are the structural inertia, aerodynamic damping, aerodynamic stiffness, structural damping and structural stiffness matrices respectively, and q are the generalised coordinates. Structural damping is often ignored (i.e D=0) in the aeroelastic equation. The eigenvalue solution to N Dof system of the aeroelastic equation (3.37) can be applied efficiently to determine the frequencies

and damping ratios at different speeds. To do that let's introduce a trivial expression of the form[1]

$$I\underline{\dot{q}} - I\underline{\dot{q}} = 0 \tag{3.38}$$

in which 'I' is NxN identity matrix. Combining equation (3.38) and equation (3.37) yields the expression

$$\begin{bmatrix} I & 0 \\ 0 & A \end{bmatrix} \begin{Bmatrix} \underline{\dot{q}} \\ \underline{\ddot{q}} \end{Bmatrix} - \begin{bmatrix} 0 & I \\ -\left(\rho V^2 C + E\right) & -(\rho VB + D) \end{bmatrix} \begin{Bmatrix} \underline{q} \\ \underline{\dot{q}} \end{Bmatrix} = \begin{Bmatrix} 0 \\ 0 \end{Bmatrix} \tag{3.39}$$

In order to convert equation (3.39) to classical eigensolution form, it is multiplied with $\begin{bmatrix} I & 0 \\ 0 & A \end{bmatrix}^{-1}$ to its both sides, which by inspection is equal to $\begin{bmatrix} I & 0 \\ 0 & A^{-1} \end{bmatrix}$,leads to

$$\begin{Bmatrix} \dot{q} \\ \ddot{q} \end{Bmatrix} - \begin{bmatrix} 0 & I \\ -A^{-1}\left(\rho V^2 C + E\right) & -A^{-1}(\rho VB + D) \end{bmatrix} \begin{Bmatrix} q \\ \dot{q} \end{Bmatrix} = \begin{Bmatrix} 0 \\ 0 \end{Bmatrix} \tag{3.40}$$

Equation (3.40) is in first order form but the 'Q' matrix (often called as system matrix) is double the size of the matrices compared with individual matrices defined in the aeroelastic equation(3.37). In order to solve the equation(3.40), let us assume $x = x_0 e^{\lambda t}$ (and differentiation of which yields $\dot{x} = x_0 \lambda e^{\lambda t}$).Substitution of 'x' and '$\dot{x}$' in the equation(3.40), one can obtain

$$I\lambda x_0 e^{\lambda t} - Q x_0 e^{\lambda t} = 0 \Rightarrow \left(I\lambda - Q\right) x_0 = 0 \Rightarrow \left(Q - I\lambda\right) x_0 = 0 \tag{3.41}$$

and equation (3.41) is the classical eigensolution form $(A - I\lambda)x = 0$. Furthermore, eigenvalues of the system matrix 'Q' appear in the complex conjugate pairs and can be written by assuming they are oscillatory roots as [1]

$$\lambda_j = -\zeta_j \omega_j \pm i\omega_j \sqrt{(1-\zeta_j^2)}, \qquad j = 1,2,...,N \tag{3.42}$$

In equation (3.42) ω_j and ζ_j are natural frequencies and damping ratios respectively and 'N' is the number of modes. In a similar way corresponding eigen vectors, which also exist in complex conjugate pairs, can be written as [1]

$$x_j = \begin{Bmatrix} q_j \\ \lambda q_j \end{Bmatrix}, \qquad j = 1,2,3,4,...N. \tag{3.43}$$

General inferences from the equation(3.42), after writing it into the form of $\lambda = a \pm jb$, are presented as follows

1. When $b \neq 0$, the roots are oscillatory otherwise these are non-oscillatory (i.e. for $b = 0$).
2. For $a > 0$, the system is unstable whereas for $a < 0$, the system is stable.

3.6.1 'P-K' method- A Frequency Matching Method

The eigenvalue solution to the equation (3.41) can give us the frequencies values provided we know the [B] and [C] matrices, but for the case when aerodynamics is the frequency dependent, [B] and [C] matrices are not known and are function of the reduced frequency (k) and hence, frequencies values. Therefore, the eigenvalue solution to the

equation (3.41) is not known unless frequencies values are calculated. In this scenario, an iterative technique such as the 'P-K' method (a frequency matching method) is employed. The key steps involved in the 'P-K' method can be summarised as follows:

1. Choose an airspeed, V.
2. Choose the i^{th} degree of freedom (i=1,….,n), when i=1, it is the first mode.
3. Set an initial value for ω_i (which is here considered as the wind-off frequency and calculated from the composite wing vibration analysis) and, hence, a '*k*'.
4. Here either simplified unsteady aerodynamic model (defined in the equation (3.23) and(3.24)) or the full unsteady aerodynamic model (defined in equation(3.19)) can be employed. For the case of simplified aerodynamic model, $M_{\theta^{\cdot}}$ is calculated from the equation (3.20) and then matrix [B] is evaluated, whereas for the full unsteady aerodynamic, Theodorson function, may be calculated and then matrices [B] and [C] are evaluated.
5. Once [B] and [C] matrices are known then solve eigenvalue solution of the first order form defined in the equation(3.41), and then compare the ω_i with the old one.
6. If the difference of ω_i between i and i+1 iteration is less then 1e-4(say), then stop and note down the corresponding damping value otherwise repeat from step 4.
7. In a similar way, repeat from step 2 for the other modes of interest.
8. Once this is complete, then increase the speed and repeat these steps up to the desired speed range.
9. Assemble the saved damping values and plot the v-g and v-ω plots to find the flutter speed from where the damping becomes negative value.

To demonstrate the 'P-K' method, consider the composite wing model 1 with lay-up scheme of $(-45/-45/0)_s$. Simplified Unsteady aerodynamics with M_θ term (which is now function of the reduced frequency, k) is used. V-g and v-ω plot is shown in Figure 3.8. Predicted flutter speed and frequency values are 21.94 m/sec and 27.0 Hz respectively.

3.7 Divergence of the Composite Wing

Divergence is a static aeroelastic phenomenon and occurs when structural stiffness is not enough to sustain further aerodynamic load or moment. It is extremely important to check the divergence condition, for example in the aircraft design, because it is unlikely on real aircraft that divergence occurs first before flutter. The divergence speed value can be determined from the solution of (by taking the static terms of the aeroelastic equation) [1]

$$\left|\rho V^2 C + E\right| = 0 \tag{3.44}$$

Divergence phenomenon can also be identified from the v-g and v-ω plot by using the constant $M_\theta$term aerodynamic model. To demonstrate the divergence speed prediction, consider the same composite wing model 1 used in the 'P-K' method with the lay-up scheme of $(45/45/0)_s$). The reason to change fibre angle from $(-45/-45/0)_s$ to $(45/45/0)_s$ is because for $(-45/-45/0)_s$ layup scheme no divergence root is predicted. Divergence speed value obtained from the solution of the equation (3.44) is 10.54 m/sec whereas from real and imaginary part of eigenvalues plot its value is 10.57 m/sec as shown in Figure 3.9. Examination of the real and imaginary parts of the eigenvalues plot shows that one of the modes reduces in frequency with an increase of speed and splits into non-oscillatory solutions around 9.25 m/sec and at this speed value, its imaginary part becomes zero. The divergence

condition is obtained when the real part of one of the non-oscillatory eigenvalues becomes positive with further increase in the air speed as shown in Figure 3.9. The flutter speed value obtained for this wing case is 21.45 m/sec and is shown in Figure 3.10.

3.8 '1-Cosine' Discrete Gust Modelling

Aircraft regularly encounter atmospheric turbulence, which in turn generate internal loads of various levels. Turbulence can be either idealised as discrete gusts or continuous, and is one of the critical aircraft design criteria. Here, a "1-cosine" discrete vertical gust model is incorporated into equation (3.37) that is used to predict the root bending moment and the tip deflection. A "1-cosine" discrete vertical gust model as a function of time can be defined as

$$w_g(t) = \frac{w_{g0}}{2}\left(1 - \cos\frac{2\pi\ V}{L_g}t\right) \tag{3.45}$$

in which w_{g0} is the value of peak or design gust velocity and L_g is the gust length. Recalling the lift expression for each strip (having width of 'dx') of the wing but with inclusion of the lift force contribution due to gust as

$$dL = \frac{1}{2}\rho V^2 c dx a_w \left\{\frac{x^2\dot{q}_1}{V} + \frac{x^3\dot{q}_4}{V} + \frac{x^4\dot{q}_7}{V} + x^2 q_2 + x^3 q_5 + x^4 q_8 + \underbrace{\frac{w_g}{V}}_{Gust\ term}\right\} \tag{3.46}$$

The generalised forces, for example, Q_{q1} and Q_{q2} can be written as

$$Q_{q1} = \frac{\partial}{\partial}\frac{\delta W}{\delta q_1} = \int_0^s \left(-x^2 dL\right)$$

$$= -\frac{1}{2}\rho V^2 c a_w \int_0^s x^2 \left\{\frac{x^2 q_1^{\bullet}}{V} + \frac{x^3 q_4^{\bullet}}{V} + \frac{x^4 q_7^{\bullet}}{V} + x^2 q_2 + x^3 q_5 + x^4 q_8 + \frac{w_g}{V}\right\} dx$$

$$= -\frac{1}{2}\rho V^2 c a_w \left\{\frac{s^5 q_1^{\bullet}}{5V} + \frac{s^6 q_4^{\bullet}}{6V} + \frac{s^7 q_7^{\bullet}}{7V} + \frac{s^5}{5} q_2 + \frac{s^6}{6} q_5 + \frac{s^7}{7} q_8 + \frac{s^3 w_g}{3V}\right\}$$

$$Q_{q2} = \frac{\partial}{\partial}\frac{\delta W}{\delta q_2} = \int_0^s \left\{\begin{array}{l} \frac{1}{2}\rho V^2 e c^2 a_w \left\{\frac{x^2 q_1^{\bullet}}{V} + \frac{x^3 q_4^{\bullet}}{V} + \frac{x^4 q_7^{\bullet}}{V} + x^2 q_2 + x^3 q_5 + x^4 q_8 + \frac{w_g}{V}\right\} + \\ \frac{1}{2}\rho V^2 e c^2 a_w \left\{\frac{M_{0^{\circ}} c}{4V}\left(x^2 q_2^{\bullet} + x^3 q_5^{\bullet} + x^4 q_8^{\bullet}\right)\right\} \end{array}\right\} x^2 dx \qquad (3.47)$$

$$= \frac{1}{2}\rho V^2 e c^2 a_w \left\{\begin{array}{l} \left\{\frac{s^5 q_1^{\bullet}}{5V} + \frac{s^6 q_4^{\bullet}}{6V} + \frac{s^7 q_7^{\bullet}}{7V} + \frac{s^5}{5} q_2 + \frac{s^6}{6} q_5 + \frac{s^7}{7} q_8 + \frac{s^3 w_g}{3V}\right\} + \\ \frac{M_{0^{\circ}} c}{4V}\left\{\frac{s^5 q_2^{\bullet}}{5} + \frac{s^6 q_5^{\bullet}}{6} + \frac{s^7 q_8^{\bullet}}{7}\right\} \end{array}\right\}$$

By adopting the same procedure, remaining terms of the gust excitation matrix can be determined. Using Lagrange equation(3.16) eventually leads to the gust terms that appear on the right hand side of the equations (3.37) as [1]

$$A\underline{\ddot{q}} + (\rho VB + D)\underline{\dot{q}} + \left(\rho V^2 C + E\right)\underline{q} = \underline{h} w_g \qquad (3.48)$$

where 'h' is the gust excitation matrix and it is a column matrix with nine rows (equal to the number of modes) and in matrix form it can be written as

$$\underline{h} = \frac{1}{2}\rho V a_w c \left[\frac{s^3}{3} \quad \frac{ecs^3}{3} \quad 0 \quad \frac{s^4}{4} \quad \frac{ecs^4}{4} \quad 0 \quad \frac{s^5}{5} \quad \frac{ecs^5}{5} \quad 0\right]^T_{1x9} \qquad (3.49)$$

and the Root Bending Moment (RBM) can be calculated as

$$RBM = \int_0^{tip} xdL = \frac{1}{2}\rho V^2 ca_w \int_0^s x\left\{\frac{x^2\dot{q_1}}{V} + \frac{x^3\dot{q_4}}{V} + \frac{x^4\dot{q_7}}{V} + x^2q_2 + x^3q_5 + x^4q_8 + \frac{w_g}{V}\right\}dx \quad (3.50)$$
$$= \frac{1}{2}\rho V^2 ca_w \left\{\frac{s^4\dot{q_1}}{4V} + \frac{s^5\dot{q_4}}{5V} + \frac{s^6\dot{q_7}}{6V} + \frac{s^4}{4}q_2 + \frac{s^5}{5}q_5 + \frac{s^6}{6}q_8 + \frac{s^2 w_g}{2V}\right\}$$

in which $\dot{q_i}$ (for i=1,4,7) and q_i (for i=2,5,8) are related to wing velocity and displacement at any instant of time and are determined utilizing the Simulink module available in Matlab. Simulink model and input gust signal are shown in Figure 3.11. Gain1, Gain and Gain2 values are equal to $A^{-1}(\rho VB)$, $A^{-1}(\rho V^2C + E), and$ $A^{-1}h$ respectively, and the gust signal is generated in Matlab. At each time step, the velocity and displacement terms are calculated and, hence, the RBM and tip deflections can be determined.

To demonstrate the gust response, consider the composite wing model 1 with lay-up scheme of $(-45/-45/0)_s$. This wing plate model is taken from ref [74]. 14 m/sec is the flight speed assumed. The tip deflection and the root bending moment are shown in Figure 3.12. It is interesting to note that the deflection at the trailing edge tip is more compared to the deflection at the leading edge tip (in positive z-direction, which is downward) thereby increasing the effective angle of attack that results in more lift and, hence, causes the higher root bending moment.

3.9 Parametric Study- Aeroelastic Analysis of the Composite Wing

In this section, the affect of fibre orientation angles on the composite wing model 1 stability speed is studied. For example, in this composite wing model total layers are six, the angle of each layer is 'θ' whereas lay-up configuration is represented with $\left((\theta)_3\right)_s$. In this example, fibre

orientation angle θ is a variable and is allowed to vary from -90° to +90° with an increment of 10°.

3.9.1 Results of Aeroelastic analysis of the composite wing

Figure 3.15 and Figure 3.16 show a section of solution space obtained by varying θ_1 and θ_2 while keeping θ_3 constant (=0°). These figures comprise a number of local optima and also rather low instability speeds regions which correspond to solutions where largely the divergence and rarely the flutter speed is the critical case.

3.10 Aero-Servo-Elastic Modelling for the Active Gust Control

The wing aeroelastic model is extended to the Aero-Servo-Elastic (ASE) model by incorporating a control surface that runs all way from the root section to the tip section as shown in Figure 3.13. Lift and moment contributions due to the control surface can be written as [1]

$$dL_{con} = \frac{1}{2}\rho V^2 c dx a_w \{a_c \beta\}$$
$$dM_{con} = (dL_{con})ec = \frac{1}{2}\rho V^2 c^2 e dx a_w \{b_c \beta\} \quad (3.51)$$

Where 'a_c', 'b_c' and 'x_b' can be determined as [8]

$$a_c = \frac{a_w}{2\pi}\left[\cos^{-1}(1-2E) + 2\sqrt{E(1-E)}\right], b_c = \frac{-a_w}{2\pi}\left[(1-E)\sqrt{E(1-E)}\right],$$
$$Ec = c - x_b, \qquad E = 1 - \frac{x_b}{c}$$

The generalised forces $Q_{q1con}, Q_{q2con}, Q_{q3con}, Q_{q4con}, Q_{q5con}, Q_{q6con}, Q_{q7con}$,

Q_{q8con} and Q_{q9con} can be written as

$$
\begin{aligned}
Q_{q1con} &= \frac{\partial}{\partial}\frac{\delta W}{\delta q_1} = \int_0^s\left(-x^2 dL_{con}\right) = -\frac{1}{2}\rho V^2 c a_w a_c \beta \int_0^s x^2 dx = -\frac{1}{2}\rho V^2 c a_w a_c \beta \left\{\frac{s^3}{3}\right\} \\
Q_{q2con} &= \frac{\partial}{\partial}\frac{\delta W}{\delta q_2} = \int_0^s\left(-x^2 dL_{con}\right) ec = -\frac{1}{2}\rho V^2 ec^2 a_w b_c \beta \int_0^s x^2 dx = -\frac{1}{2}\rho V^2 ec^2 a_w b_c \beta \left\{\frac{s^3}{3}\right\} \\
Q_{q4con} &= \frac{\partial}{\partial}\frac{\delta W}{\delta q_4} = \int_0^s\left(-x^3 dL_{con}\right) = -\frac{1}{2}\rho V^2 c a_w a_c \beta \int_0^s x^3 dx = -\frac{1}{2}\rho V^2 c a_w a_c \beta \left\{\frac{s^4}{4}\right\} \\
Q_{q5con} &= \frac{\partial}{\partial}\frac{\delta W}{\delta q_5} = \int_0^s\left(-x^3 dL_{con}\right) ec = -\frac{1}{2}\rho V^2 ec^2 a_w b_c \beta \int_0^s x^3 dx = -\frac{1}{2}\rho V^2 ec^2 a_w b_c \beta \left\{\frac{s^4}{4}\right\} \\
Q_{q7con} &= \frac{\partial}{\partial}\frac{\delta W}{\delta q_7} = \int_0^s\left(-x^4 dL_{con}\right) = -\frac{1}{2}\rho V^2 c a_w a_c \beta \int_0^s x^4 dx = -\frac{1}{2}\rho V^2 c a_w a_c \beta \left\{\frac{s^5}{5}\right\} \\
Q_{q8con} &= \frac{\partial}{\partial}\frac{\delta W}{\delta q_8} = \int_0^s\left(-x^4 dL_{con}\right) ec = -\frac{1}{2}\rho V^2 ec^2 a_w b_c \beta \int_0^s x^4 dx = -\frac{1}{2}\rho V^2 ec^2 a_w b_c \beta \left\{\frac{s^5}{5}\right\}
\end{aligned}
\tag{3.52}
$$

Q_{q3con}, Q_{q6con} *and* Q_{q9con} are equal to zero. In matrix form, these generalised forces, can be arranged as

$$
\underline{g} = -\frac{1}{2}\rho V^2 c a_w \beta \left[a_c \frac{s^3}{3} \quad ecb_c \frac{s^3}{3} \quad 0 \quad a_c \frac{s^4}{4} \quad ecb_c \frac{s^4}{4} \quad 0 \quad a_c \frac{s^5}{5} \quad ecb_c \frac{s^5}{5} \quad 0 \right]^T_{1x9} \tag{3.53}
$$

Let us introduce PI (Proportional and Integral controller), in which control surface angle (β) is proportional to the wing velocity and displacement terms at any time. These velocity and displacement terms can be calculated from the feedback signal of transducer that can be attached at the wing's leading edge (say at x= s_0, y=0,y_f=c/2). Suppose the distance of this transducer from the wing root is 's_0' (see Figure 3.13).

Mathematically, the control surface angle (β), for PI controller, can be written as

$$
\beta = kv\left(\dot{w}\right) + kd\left(w\right) \tag{3.54}
$$

where 'kv' and 'kd' are feedback gains applied to the velocity and the displacement terms respectively. Substituting the out of plane deflection 'w' from equation (3.22) into equation (3.54), expression for the control surface angle can be obtained as

$$\beta = kv\begin{pmatrix} x^2\dot{q}_1 + x^2(y-y_f)\dot{q}_2 + x^2(y-y_f)^2\dot{q}_3 + x^3\dot{q}_4 + x^3(y-y_f)\dot{q}_5 + \ldots \\ x^3(y-y_f)^2\dot{q}_6 + x^4\dot{q}_7 + x^4(y-y_f)\dot{q}_8 + x^4(y-y_f)^2\dot{q}_9 \end{pmatrix}$$
$$+kd\begin{pmatrix} x^2 q_1 + x^2(y-y_f)q_2 + x^2(y-y_f)^2 q_3 + x^3 q_4 + x^3(y-y_f)q_5 + \ldots \\ x^3(y-y_f)^2 q_6 + x^4 q_7 + x^4(y-y_f)q_8 + x^4(y-y_f)^2 q_9 \end{pmatrix} \qquad (3.55)$$

After substituting x= s_0, y=0,y_f=c/2 in the equation (3.55), yields the control surface angle in the matrix form as

$$\beta = kv\left[s_0^2 \quad -\frac{c}{2}s_0^2 \quad \frac{c^2}{4}s_0^2 \quad s_0^3 \quad -\frac{c}{2}s_0^3 \quad \frac{c^2}{4}s_0^3 \quad s_0^4 \quad -\frac{c}{2}s_0^4 \quad \frac{c^2}{4}s_0^4\right]\begin{Bmatrix}\dot{q}_1\\ \dot{q}_2\\ \dot{q}_3\\ \dot{q}_4\\ \dot{q}_5\\ \dot{q}_6\\ \dot{q}_7\\ \dot{q}_8\\ \dot{q}_9\end{Bmatrix} +$$
$$kd\left[s_0^2 \quad -\frac{c}{2}s_0^2 \quad \frac{c^2}{4}s_0^2 \quad s_0^3 \quad -\frac{c}{2}s_0^3 \quad \frac{c^2}{4}s_0^3 \quad s_0^4 \quad -\frac{c}{2}s_0^4 \quad \frac{c^2}{4}s_0^4\right]\begin{Bmatrix}q_1\\ q_2\\ q_3\\ q_4\\ q_5\\ q_6\\ q_7\\ q_8\\ q_9\end{Bmatrix} \qquad (3.56)$$

The ASE equation can then be formulated as

$$A\ddot{\underline{q}} + (\rho VB + D)\dot{\underline{q}} + (\rho V^2 C + E)\underline{q} = \underline{g}\beta \qquad (3.57)$$

Where 'g' is defined in the equation(3.53), 'β' is defined in the equation (3.56) and substituting these matrices, leads to formulation of the final ASE equation to [1]

$$A\ddot{\underline{q}}+(\rho VB+D)\dot{\underline{q}}+\left(\rho V^2C+E\right)\underline{q}=F\dot{\underline{q}}+G\underline{q}\Rightarrow$$
$$A\ddot{\underline{q}}+(\rho VB+D-F)\dot{\underline{q}}+\left(\rho V^2C+E-G\right)\underline{q}=0 \qquad (3.58)$$

in which [F] and [G] are the feedback matrices and change with the change in control gains ('kv' and 'kd'), density and airspeed. It is interesting to note that [F] and [G] matrices (arise due to the control surface) alter the system damping and stiffness matrices respectively.

The system stability can be examined by solving the closed-loop ASE equation(3.58) for any given values of 'kv' and 'kd'. Once 'kv' and 'kd' are known 'β', which is the control surface angle, can be calculated from the equation(3.56) against any gust signal.

To demonstrate the underlying concept in the ASE model, the composite wing model 2 is assumed. Lay-up scheme considered here is$((-20.5468)_2/(36.1805)_2/(48.3433)_2)_s$ as it gives the maximum flutter speed value of 34.871m/sec.Various results for the cases of with and without aileron engagement are presented in Figure 3.14.

3.11 Conclusions

1. An efficient assumed mode model (as it requires less degree of freedoms compared with the reference FEM model) is developed to predict the vibration response of the composite wing by utilizing the Rayleigh Ritz method and is capable of accounting for the bend-twist coupling terms for the symmetric lay-up schemes.

2. Vibration frequencies results obtained from the present model have shown excellent agreement with the published results. Maximum percentage error for the torsion mode is less than 1.5 and for the bending modes, it is less than 1.0 percent.

3. Vibration frequency plots are symmetric about the 0^o(see Figure 3.6) even though $(45^o)_{3s}$ has positive D_{16} and D_{26} values and $(-45^o)_{3s}$ has negative D_{16} and D_{26} values.

4. Two versions of aeroelastic models are developed, one with the constant M_{θ} term (can be called as the frequency independent aeroelastic model) and other when M_{θ} is the function of the reduced frequency (frequency dependent aeroelastic model). When M_{θ} is the function of the reduced frequency, the 'P-K' method is adopted and its result (flutter speed is 21.94 m/sec) is not very different from when compared with the result of the constant M_{θ} model (flutter speed is 21.45 m/sec).

5. ASE model is derived to control the root bending moment in an active manner caused due to the gust; however, it requires two gain values that need to be explored such that system remains stable.

Property	Values
E_1(GPa)	98.
E_2(GPa)	7.9
υ_{12}	0.28
G_{12}(GPa)	5.6
G_{13}(GPa)	5.6
G_{23}(GPa)	5.6
Ply thickness	0.134 (mm)
Density	1520(Kg/m^3)

Table 3.1: Material properties for Hercules AS1/3501-6 graphite/Epoxy

Laminate	D_{11}	D_{12}	D_{16}	D_{22}	D_{26}	D_{66}
$[0_2/90]s$	4.1259	0.0964	0	0.4898	0	0.2425
$[30_2/0]s$	2.7026	0.7198	1.1787	0.6663	0.4588	0.8659
$[45_2/0]s$	1.5494	0.9276	0.9454	1.4039	0.9454	1.0737
$[60_2/0]s$	0.8118	0.7198	0.4588	2.5571	1.1787	0.8659
$[90_2/0]s$	0.4898	0.0964	0	4.1259	0	0.2425
Aluminium	3.3315	0.9995	0	3.3315	0	1.1659

Table 3.2: Flexural moduli for laminates and Aluminium

	Lay-up Scheme	**Total Thickness (mm)**	**Material Properties**	**Value**
Front Spar	$((-45^o)_4)_s$	1.00	E_1	140(GPa)
Rear Spar	$((-45^o)_4)_s$	1.00	E_2	10.0(GPa)
Top Skin	$((-45^o)_2 / (45^o)_3 /90^o)_s$	1.50	υ_{12}	0.3
Bottom Skin	$((-45^o)_2 /(45^o)_3 /90^o)_s$	1.50	G_{12}	5.0(GPa)
Ribs	$((-45^o)_2)_s$	0.50	Ply thickness	0.125 (mm)
			Density	1570(Kg/m^3)

Table 3.3: Lay-up Scheme for Composite Wing

No of BM	No of TM	No of CWBM	Frequency values(Hz)	
			Case1=$(0/0/90)_s$	Case2=$(45/45/0)_s$
1	0	0	14.08	8.63
2	0	0	11.12, 109.56	6.81,67.14
3	0	0	11.07, 69.99,371.89	6.78,42.89,227.89
4	0	0	11.07,69.75,199.40	6.78,42.74,122.19
5	0	0	11.07,69.36,199.06	6.78,42.50,121.98
2	1	0	11.12,56.39,109.56	6.32,45.39,125.42
3	1	0	11.07,56.39,69.99	6.30,35.69,97.86
4	1	0	11.07,56.39,69.75	6.30,35.65,93.16
2	2	0	11.12,41.96,109.56	5.55,45.10,83.71
3	2	0	11.07,41.96,69.99	5.40,34.53,83.38
4	2	0	11.07,41.96,69.75	5.40,34.50,83.2
4	2	1	11.07,41.96,69.71	5.39,34.50,74.00
4	2	2	11.06,41.96,69.66	5.37,34.47,60.81
3	**3**	**3**	**11.06, 39.74, 69.89**	**5.16, 32.63, 55.11**
4	**4**	**8**	**11.06,39.61, 69.65**	**4.96,31.29, 51.97**

BM=Bending Mode, TM=Torsion Mode, CWBM=Chord-wise Bending Mode

Table 3.4: Convergence Study for the first three frequency values of the composite plate

Lay-up	Mode	FEM (365 DOF) Reference[74](Hz)	Analytical (36 DOF) Present(Hz)	Percentage Error
$(0_2/90)s$	1B	11.1	11.05	0.45
	2B	69.5	69.26	0.34
	1T	39.5	39.55	-0.12
$(15_2/0)s$	1B	8.9	8.94	-0.45
	1B	62.7	62.69	0.02
	1T	42.9	42.90	0.0
$(30_2/0)s$	1B	6.3	6.31	-0.15
	1B	37.3	37.29	0.03
	1T	56.9	57.32	-0.73
$(45_2/0)s$	1B	4.9	4.89	0.2
	2B	30.1	30.1	0.0
	1T	49.4	50.1	-1.4
$(60_2/0)s$	1B	4.2	4.19	0.24
	2B	26.1	26.11	0.04
	1T	41.7	42.26	-1.3
$(75_2/0)s$	1B	3.9	3.88	0.5
	2B	24.3	24.31	-0.04
	1T	36.7	37.03	-0.9
$(90_2/0)s$	1B	3.8	3.8	0.0
	2B	23.9	23.85	0.2
	1T	35.1	35.16	-0.17

Table 3.5: Composite Wing vibration Results(1B: First Bending, 2B: 2nd Bending, 1T: First Torsion)

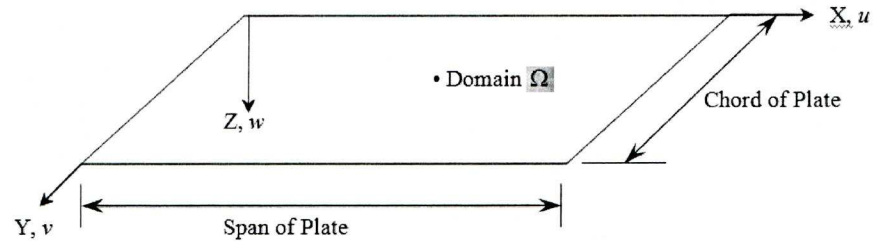

a) Geometry and Axes Definition of Plate

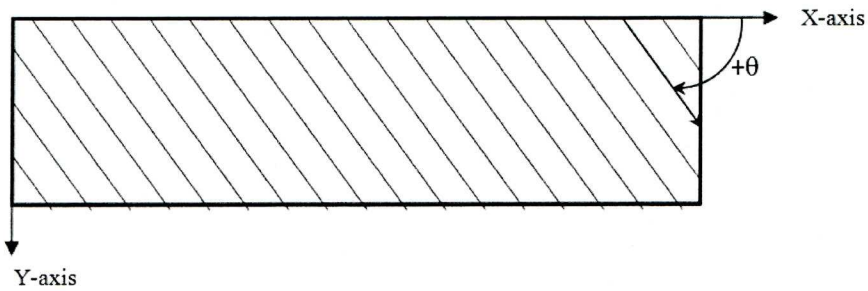

b) Positive rotation of fibre axis from X-Y plane

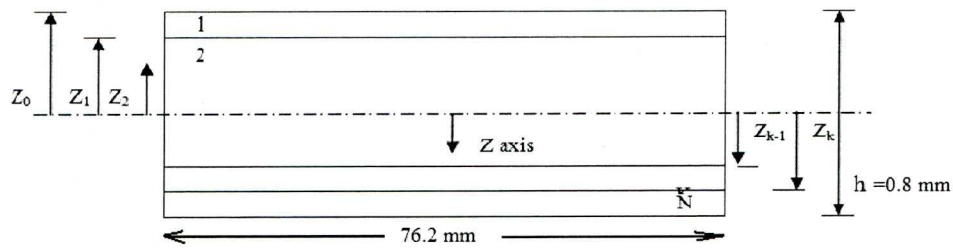

c) Definition of Z-coordinate and N layer laminate

Figure 3.1: Definitions of geometry and axis, fibre angle and Z-coordinate of N layer laminate plate

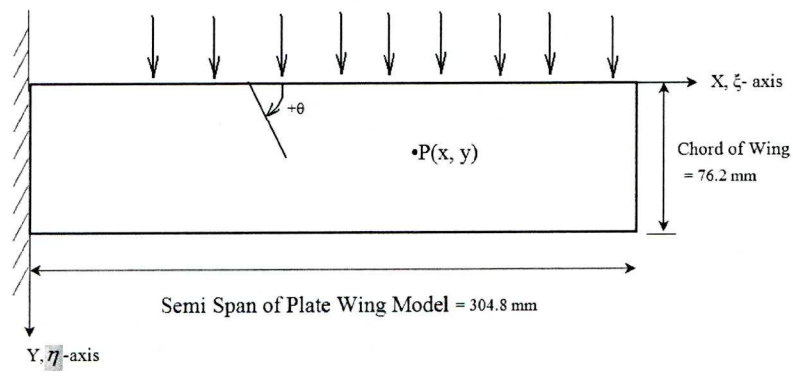

Figure 3.2: Out of plane Deflection of Point P(x,y) on surface of Wing

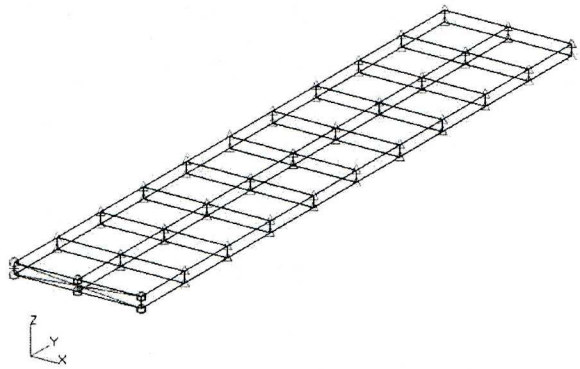

Figure 3.3: Finite Element Model of the Goland Wing

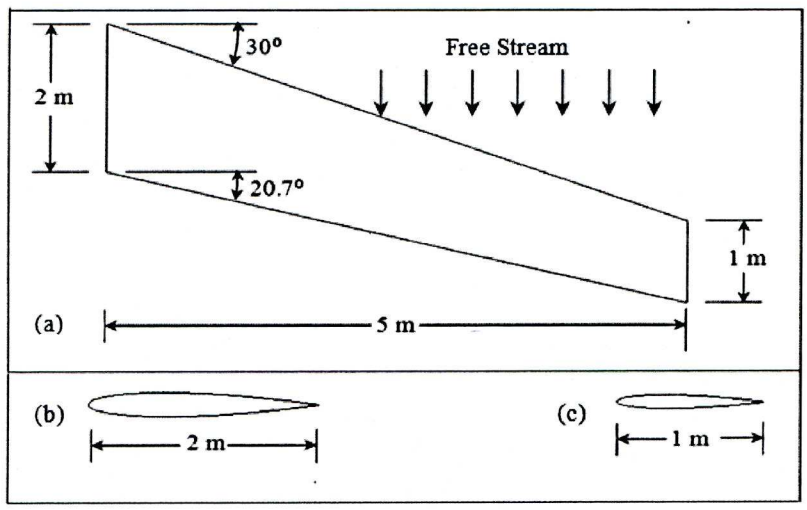

Figure 3.4: (a) Wing semi-span and sweep angle (b) Root Chord (c) Tip chord

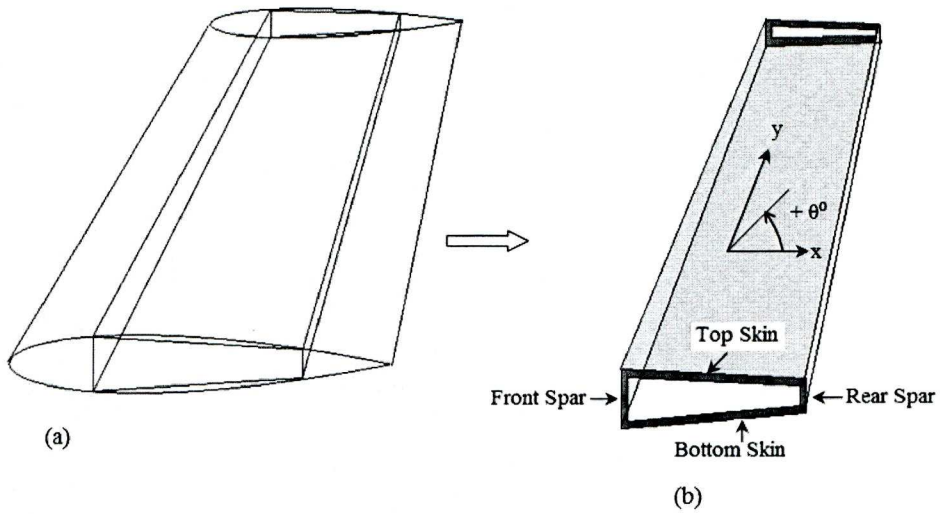

Figure 3.5: (a) Wing Box starts at 25% and 75% chord. (b) Wing Box Definition

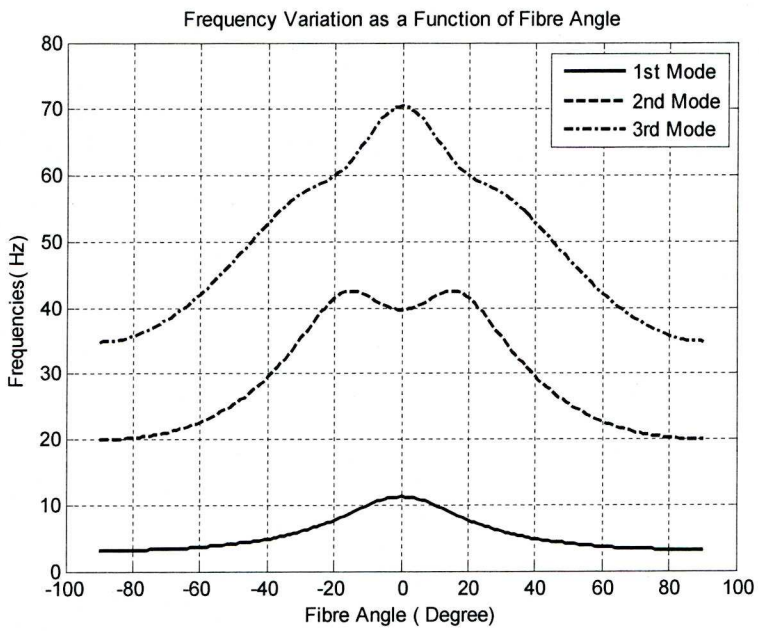

a) Frequencies trends with the change of the fibre angles

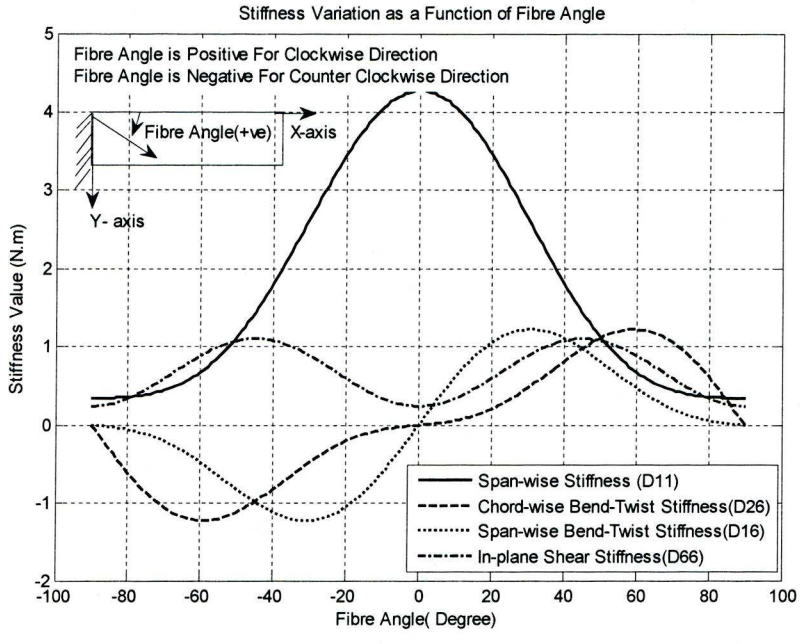

b) Stiffness trends with the change of the fibre angles

Figure 3.6: Frequencies and Stiffness trends with the change of the fibre angles

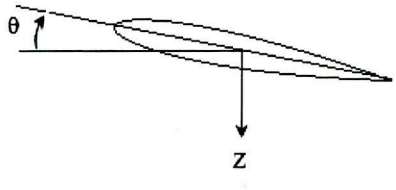

Figure 3.7: Pitch and Plunge motion of the aerofoil

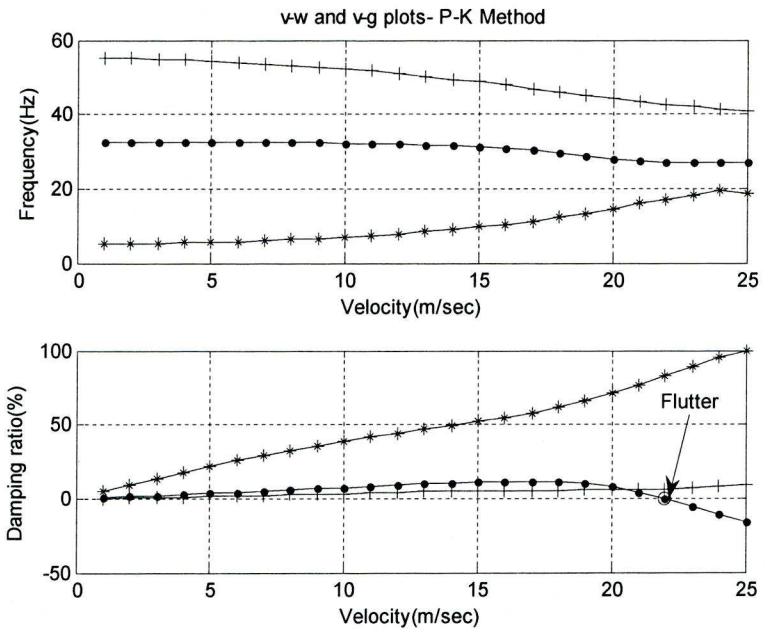

Figure 3.8: v-g and v-ω plot- 'PK' Frequency Matching Method

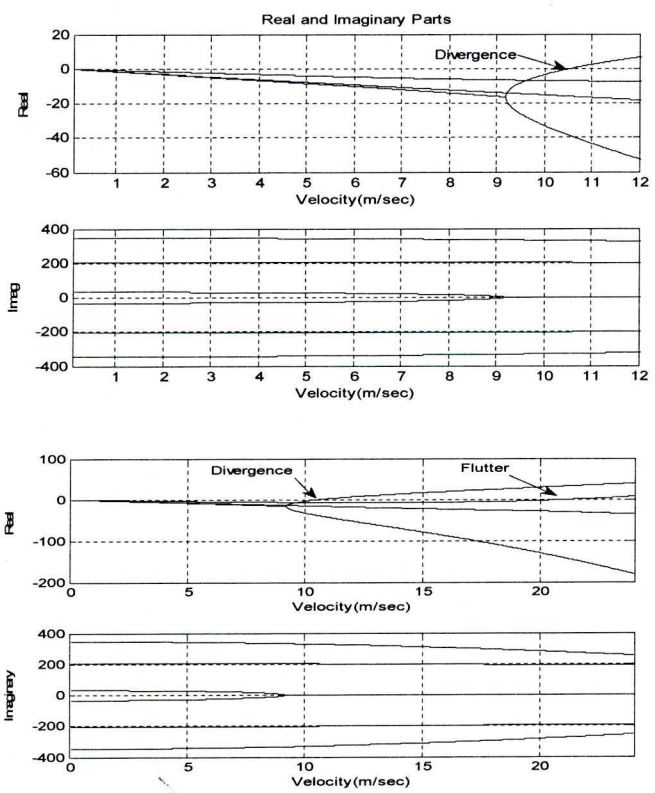

Figure 3.9: Trends of real and imaginary parts of the eigenvalues for the composite wing

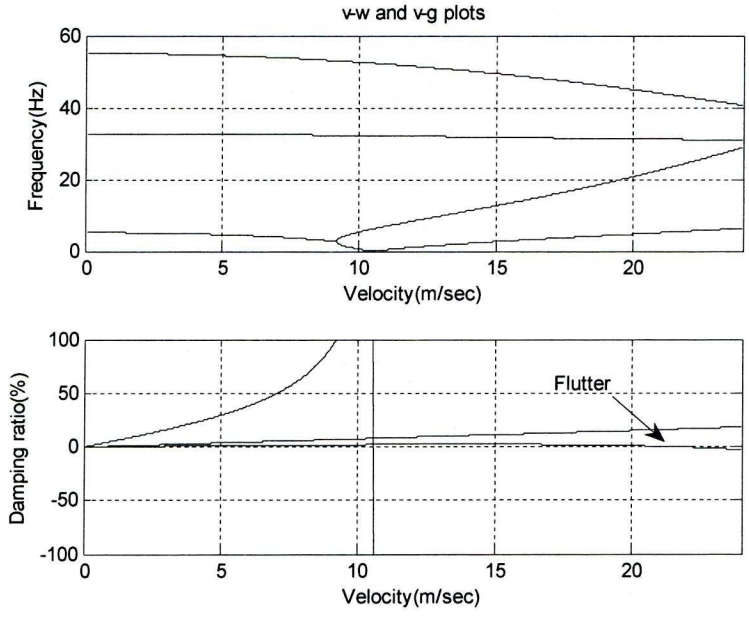

Figure 3.10: v-g and v-ω plot for the composite wing

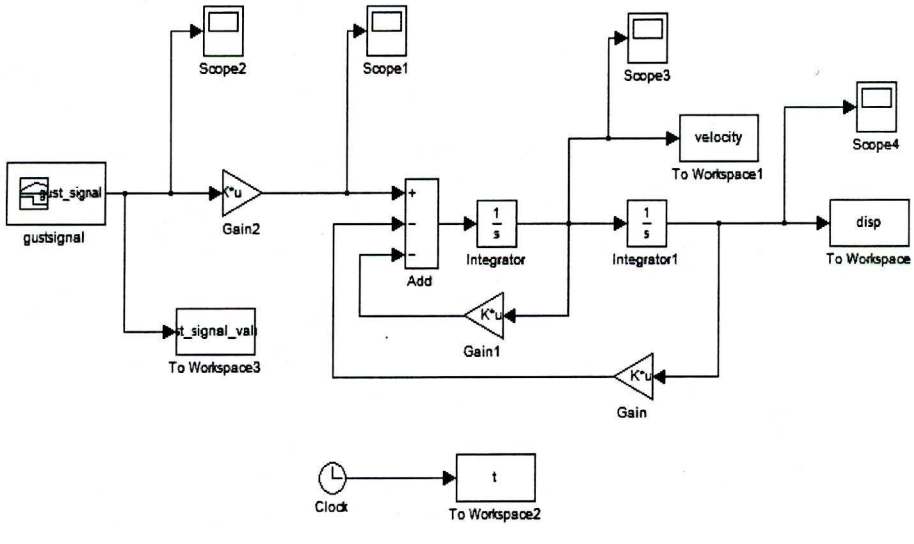

a) The Simulink Model

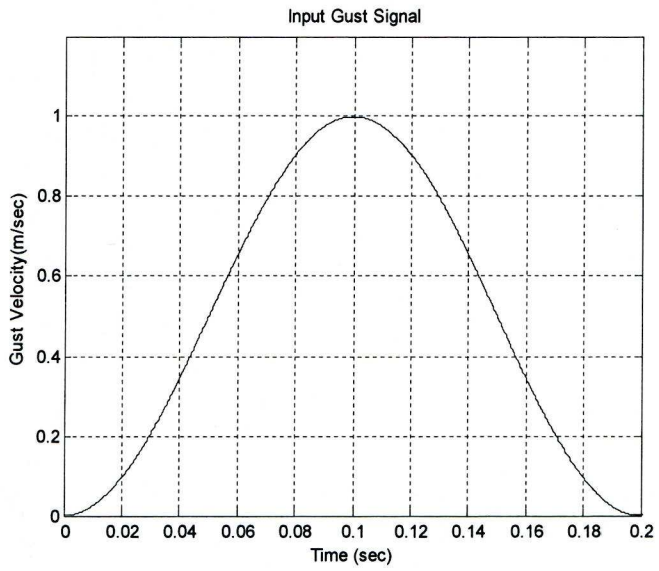

b) Input gust signal

Figure 3.11: The Simulink Model and input gust signal

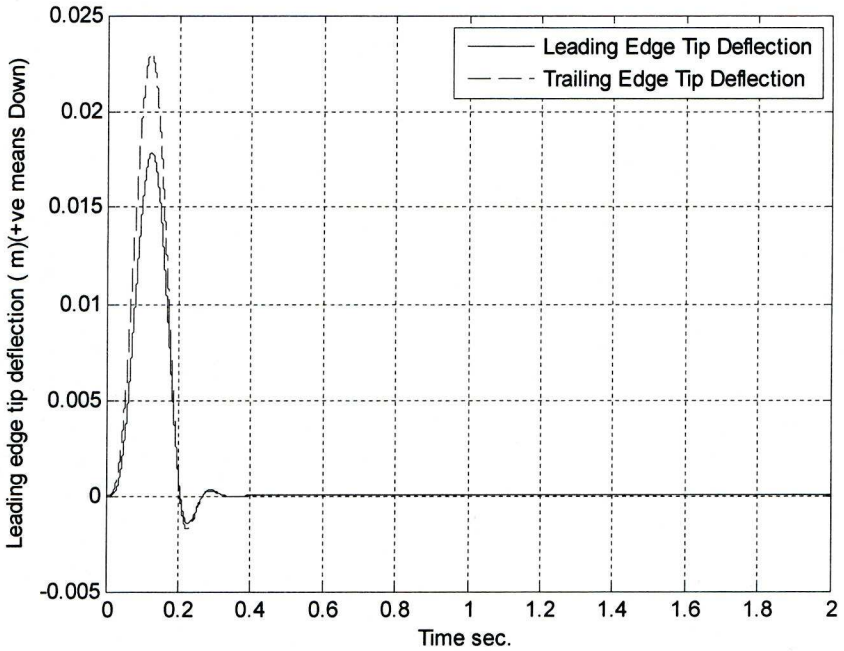

a) Leading and the trailing edge tip deflection (in meters)

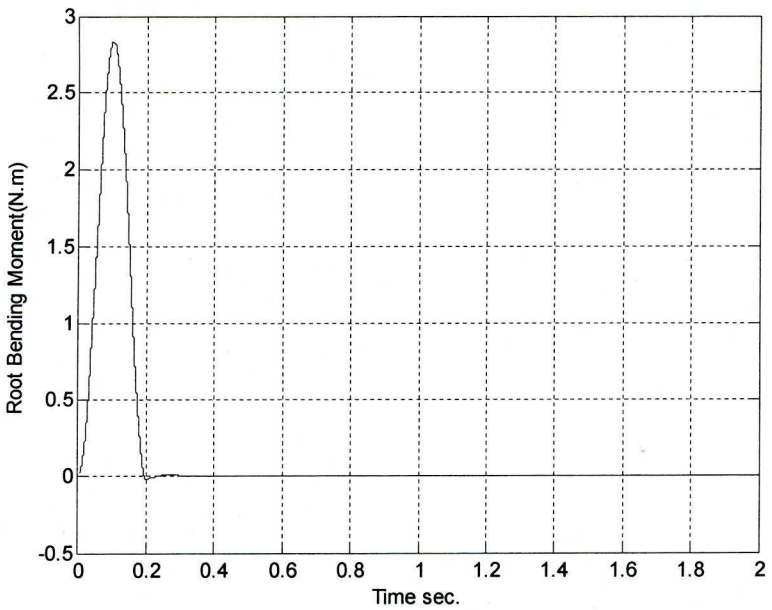

b) The Root Bending Moment (in N.m)

Figure 3.12: LE and TE tip deflection and Root Bending Moment

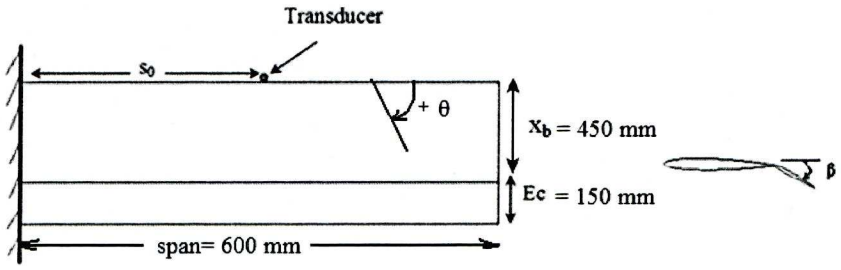

Figure 3.13: Composite Wing with the Control Surface

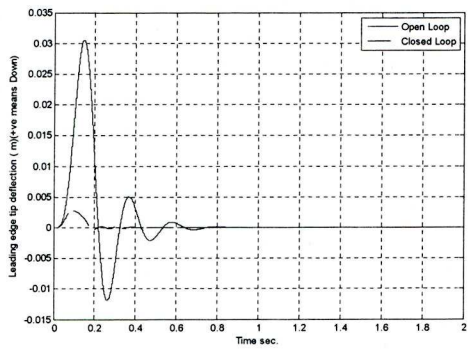

a) LE and TE tip deflection(m)

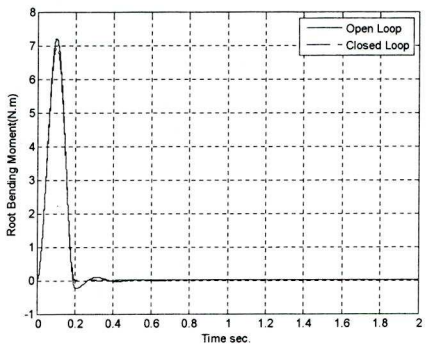

b) Root Bending Moment (N.m)

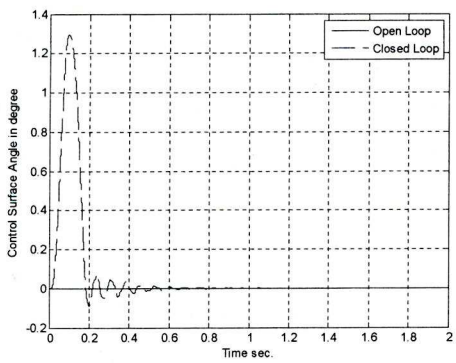

c) Control Surface Angle(deg)

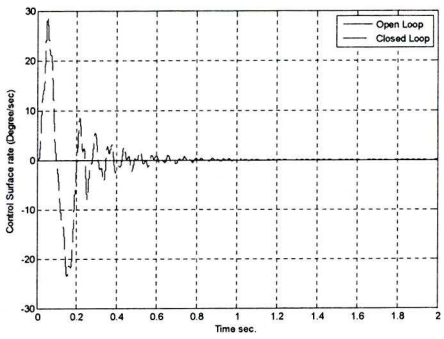

d) Control Surface Rate(deg/sec)

Figure 3.14: Various results for closed and open loop simulations

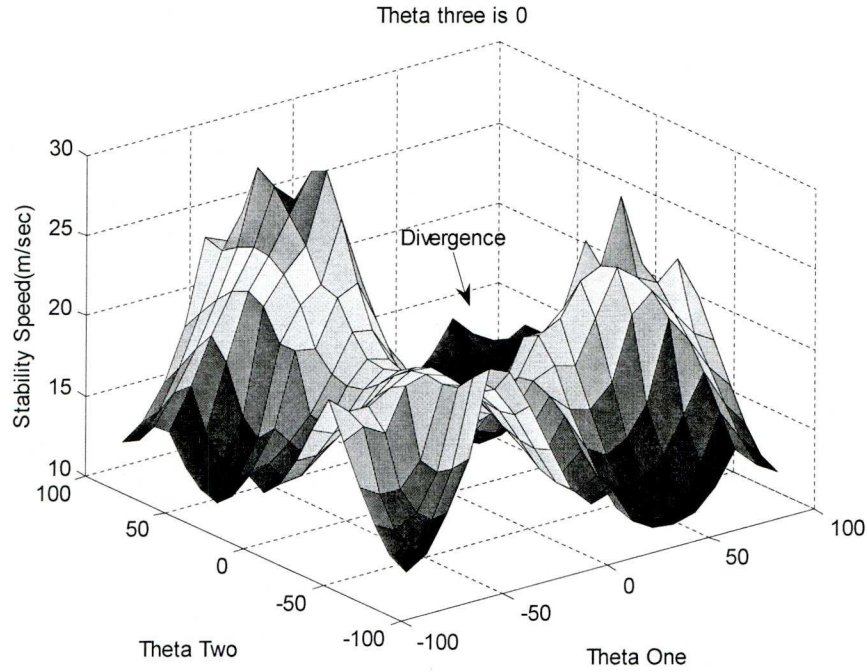

Figure 3.15: Stability speed plot- Theta one and the theta two are variable (Theta three is 0)

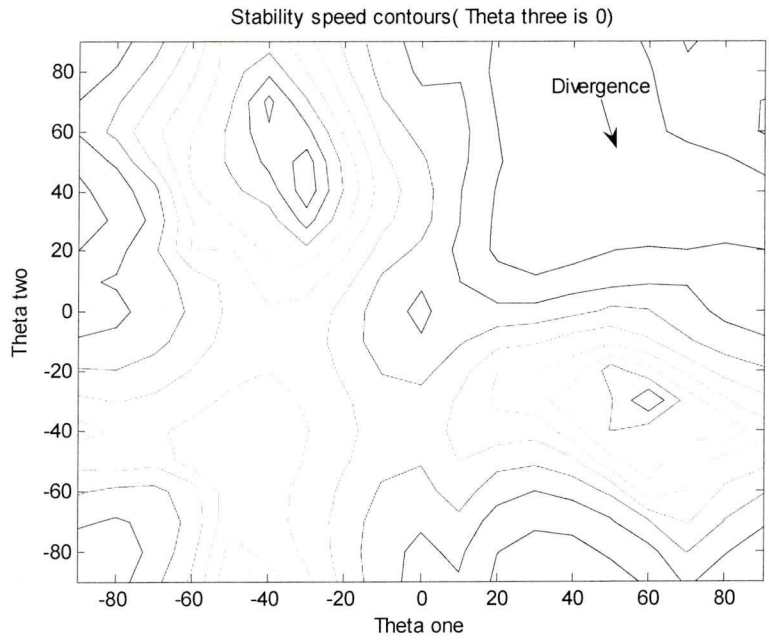

Figure 3.16: Contour plot to identify the higher stability speed zones

Chapter 4

Aeroelastic Tailoring and Evolutionary Algorithms

4.1 Introduction

Aeroelastic tailoring is an approach in which the composite fibre orientation is adjusted to control the static and/or dynamic aeroelastic behaviour of the composite lifting surface in a passive manner[29]. The fibre orientation influences the various coupling terms with both symmetric and non-symmetric lay-ups, which not only provides design flexibility but also at times poses an optimisation challenge.

Various approaches can be applied for aeroelastic tailoring of a wing. One course could be to divide the wing structural members into various sections and search for the fibre orientations independently for each section to meet the desired aeroelastic constraints. In the present work a simplified approach is applied i.e. the composite wing of a known geometry is aeroelasticity tailored by varying the fibre orientation angles for the entire wing.

The objective of this chapter is to apply both GA and PSO evolutionary algorithms to maximise the flutter/divergence speed and to minimise the root bending moment caused by a "1-Cosine" discrete gust in a passive manner. In this regard, three types of optimisation problems are defined to find the optimum fibre orientation angles:

- Maximisation of the flutter/divergence speed.
- Minimisation of the root bending moment caused by a gust in a passive manner.

- Maximisation of the flutter/divergence speed and minimisation of the root bending moment caused due to gust- a multi objective problem.

4.2 Evolutionary Optimisation Methods

Two evolutionary algorithms, namely, Binary Genetic Algorithm (GA) and Particle Swarm Optimisation (PSO) method are presented herein and applied to the aeroelastic optimisation problems. GA is based on the Darwinian Theory of natural selection and works on the survival of the fittest principle, whereas the PSO concept mimics the behaviour of the swarm of birds. In PSO, the particles compete and communicate between each other and change their positions and speeds accordingly and eventually achieve some desired objective(s).

Such methods produce a near optimum solution when applied in various engineering fields (such as in the flutter problem) in much quicker time for large parameter space solutions compared to an exhaustive search; however, these methods do not guarantee that the solution is the global optimum. The underlying concepts of these methods are discussed in the next section.

4.2.1 Binary Genetic Algorithm-Basic Concepts

The basic concepts involved in BGA are as follows [76, 77]:

1. In a binary GA, the parameters of any system to be optimised need to be represented by a series of 1s and 0s (based on binary code) and called as a gene. Each element of the gene is often called a cell, for example, the following represents a gene with nine cells

Gene 0 1 1 0 1 1 0 1 0.

Randomly, a pool of genes (the 'parent' genes) is created, each gene representing a random solution.

2. The fitness of each random solution (the 'parent' gene) is calculated, which is defined with a fitness function, for example, the flutter speed of a wing.

3. Genes are then paired up randomly for the mating process and this selection is biased towards the fitter genes of the population.

4. Crossover process (a main process) is performed on the paired genes to generate a new set of genes ('offspring') with each 'offspring' representing a new set of possible solutions. The crossover process, for example, for the two nine-cell genes can be represented as, where partition line is generated randomly,

	Gene one	Gene two
Before Crossover	0 1 1 0 1 1 0 1 0	1 1 1 0 1 0 1 0 1
After Crossover	0 1 1 0 1 0 1 0 1	1 1 1 0 1 1 0 1 0

5. Mutation and translation are two low probability operations (their probability is defined by the user, often assumed between 0.05-0.1), which are performed after crossover operation, effectively to input new information in the solution. In mutation, randomly a cell (or bit) is changed whereas in the translation operation, cells (or bits) translate their position and change the order within the gene randomly defined by a partition line, highlighted as follows

	Gene one
Before Mutation	0 1 1 0 1 1 0 1 0
After Mutation	0 1 1 1 1 1 0 1 0

	Gene one
Before Translation	0 1 1 0 1 1 0 1 0
After Translation	1 1 0 1 0 0 1 1 0

6. In the BGA, the best genes (elite genes) are carried forward to the next generation to avoid losing a best solution.

7. New blood can be introduced by replacing the worst gene(s) in the previous pool of genes. Concept behind it is to introduce completely a new set of offspring that has not inherited any aspect of previous generations (parents); and can be envisaged as to explore the design space unbiased from the previous parents.

8. The same process is repeated for the subsequent generations to obtain the best cost function (i.e. flutter speed). User can define termination criterion either to search some predefined number of generations or when best cost does not vary after a certain number of iterations.

The flow chart of BGA indicating various processes is shown in Figure 4.1.

4.2.2 Particle Swarm Optimisation

Particle Swarm Optimization (PSO) is a heuristic search method which is based on a simplified social model that is closely tied to swarming theory and intelligence in which each particle of the swarm has memory and can also communicate with each other[78]. Such particle knows the best value it has achieved and that position, and the swarm knows what has the best value and the position. The position and velocity of each

particle is updated by knowing the previous best values of each particle and overall swarm such that for the kth iteration[78]

$$v_i(k+1) = wv_i(k) + c_1\varphi_1(p_i(k) - x_i(k)) + c_2\varphi_2(g_i(k) - x_i(k)) \quad (2.1)$$

$$x_i(k+1) = x_i(k) + v_i(k) \quad (2.2)$$

where v_i and x_i are the velocity and position of particle i , p_i and g_i are the best positions found by each particle and the entire population; φ_1 and φ_2 are independent uniformly distributed random numbers and are generated independently. w, c_1 and c_2 are the user defined inertia factor (=1), particle belief factor (=2) and swarm belief factor (=2) respectively.

w, c_1 and c_2 are inertia, self belief and swarm belief factors respectively. These factors can be either constant or variable, selection of which is the user discretion. A higher value of w changes the next position of particle with a large value and creates a chance to miss the (near) optimum point and lower value of which can make the search for optimum an exhaustive one. Similarly, c_2 can be gradually increased from lower value meaning that after certain number of iterations belief on swarm results increases. However, their sum must not increase more then 4 [78]. In the present code, w=1 and c_1=c_2=2 i.e. a constant fifty/fifty belief factor is assumed. Note that this PSO implementation is a continuous search method, which means that it can pick any fibre angle value.

4.3 Aeroelastic Tailoring of the Composite Wing

The composite wing was optimised by applying both binary GA and PSO methods. Three types of design optimisation problems were investigated, namely

1) Aeroelastic tailoring to maximise Flutter/ Divergence Speed
2) Aeroelastic tailoring to search passive Gust Alleviated Design
3) Maximisation of the flutter/divergence speed and minimisation of the root bending moment caused due to gust- a multi objective problem.

The aeroelastic codes developed in Chapter 3 were utilised for these aeroelastic-tailoring problems.

4.3.1 Wing model and problem Definition

A baseline wind tunnel rectangular composite wing model 1 of six layers with three orientation variables i.e. $(\theta_1/\theta_2/\theta_3)_s$, and composite wing model 2 of ten layers with three orientation variables i.e. $\left(\theta_1/(\theta_2)_2/(\theta_3)_2\right)_s$ are considered for optimisation.

Problem Definition

The fibre orientation angles are the optimisation parameters and because of the symmetric layup assumption, number of angles is three $(\theta_1/\theta_2/\theta_3)_s$ for the wing model 1. Although this might seems to be a trivial problem with only three parameters$(\theta_1/\theta_2/\theta_3)_s$ needing to be determined, because of the highly coupled nature of the aeroelastic system (see Figure 3.15), the optimised lay-up configuration is not easy to find[79].

In total, 20 solutions (genes or particles) were used for each approach. For each solution case, the methods was run for a maximum of 100 generations/iterations, with convergence was considered to occur if best solution did not vary for 20 iterations. Objective to run such an exhaustive search was to analyse the optimised $(\theta_1/\theta_2/\theta_3)_s$ values predicted by both the approaches. Such an exhaustive search was applied for the maximisation of flutter/divergence case only.

4.3.2 Aeroelastic Tailoring to Maximise Stability Speed-Application of Binary GA

A binary representation of the composite lay-up assigned 5 cells (32 possible orientations were chosen) to each layer, giving a gene length of 15 cells. The binary GA method already explained in the previous section was employed, with 20 genes being included in the gene pool, the 4 best genes saved after each iteration, a 90 % probability of crossover, a 5% probability of mutation and a 10% likelihood of translation.

The best speed and Orientations from 100 generations/iteration case is shown in Table 4.2. Figure 4.2 shows the best flutter speed solutions and corresponding ply angles from 100 iterations for the wing model 1. From results we see that for majority of converged solutions, θ_1 is ~-33.75° where as θ_2 has some scatter. θ_3 has shown a large scatter owing to the fact that it is closest to the neutral axis and hence participates least to the overall bending stiffness values of the composite wing.

The overall stiffness values for the optimum lay-up configuration are also shown in Table 4.3, in which we see that the torsion stiffness term is ~50% of the bending stiffness and the bend-torsion stiffness is 30% of the bending stiffness.

4.3.3 Aeroelastic Tailoring to Maximise Stability Speed-Application of PSO

For the PSO approach, 20 particles were selected to make it consistent with the BGA in which 20 genes were used. Convergence criterion also remained the same and the PSO process continued for 100 iterations or until convergence occurred.

The best speed and orientations from 100 iterations case is shown in Table 4.4. Figure 4.2 shows the best flutter speed solutions and corresponding ply angles from 100 iterations for wing model 1. From results we see that for majority of converged solutions, θ_1 is ~-33° where as θ_2 has very small scatter around 45° compared to binary GA. θ_3 has a very little effect on the flutter speed.

It is interesting to note the clustering effect on the solution, scatter for PSO is much less compared to BGA.

The overall stiffness values for the optimum lay-up configuration is also revealed in Table 4.5, in which we see that the torsion stiffness term is ~50% of the bending stiffness and the bend-torsion stiffness is 30% of the bending stiffness and are very similar to the BGA results.

4.3.4 Passive Gust Alleviated Design

Passive gust alleviated designs are the one for which the wing effective angle of attack is lowered passively against the gust lift force. In order to optimise the passive gust alleviated designs, the wing model two (see section4.3.1) was employed. The objective was to find fibre angle lay-up configurations for which Root Bending Moment caused by a "1-cosine" discrete gust is minimal. The gust model as developed in equation (3.48) was applied for this purpose. PSO was employed to find

the optimum solution. Root Bending Moment and instability speed for the optimised fibre orientations are presented in Table 4.6.

The Root Bending Moment and leading and trailing edge tip deflection are shown in Figure 4.4and Figure 4.5 respectively for the both baseline and optimised designs against an input gust signal (see Figure 4.3). It is interesting to note that, for the optimised design, leading edge tip deflects more downward compared to the trailing edge indicating that wing tries to lower the effective angle of attack and hence we observe minimal Root Bending Moment.

Flutter/Divergence speed for these fibre orientations is very poor compared with the baseline design. Therefore, it can be said that best passive gust alleviated design is poor in flutter/divergence response and multi-objective design optimisation is required to address such type of problems.

4.4 Multi-Objective Aeroelastic Tailoring

The fibre placement requirement in the composite structure to increase the flutter/divergence speed conflicts that used to attain maximum gust alleviation (increased downwash). Consequently, if the wing is optimised considering just one of these parameters, it is likely that the performance of the other will be poor. Consider a multi-objective cost function Ω_{det} that combines both requirements such that

$$\Omega_{det} = \min(w_f * \frac{V_d}{V_{max}} + w_g * \frac{R_{min}}{R_d}) \tag{2.3}$$

in which w_f , w_g are weight factors whose sum equals unity, V_d and V_{max} are the design and maximum flutter/divergence speed, and R_d and R_{min} are the design and minimum root bending moment. Setting either

of the weight factors to unity gives the cases where one of the objective functions is inactive, and by setting the weightings for various values between 0 and 1 leads to the determination of the Pareto Frontier [80]that defines the best multi-objective flutter speed and root bending moment solution for different weight factors.

The wing model two was considered and PSO was employed with 20 particles in each loop and a maximum total of 50 iterations conducted, in order to optimise the lay-up for each set of weighting values. Maximum flutter speeds and bending moments for different weighting values are given in Table 4.7 and the points making up the Pareto Optimal Curve are shown in Figure 4.6. As might be expected, the maximum instability speed is obtained when the gust constraint is inactive, and the minimum root bending moment obtained when the flutter constraint is inactive. Note that the instability speed drops significantly when only the gust response is considered, in this case divergence instability is found. The ideal case would be when flutter speed is 25.07 m/sec (which is flutter only case) and RBM is 7.157 N.m (which is the Gust only case). Here an average principle is applied which means that sum of ratio of the flutter speed to the maximum flutter speed and the RBM value to the minimum RBM value should be close to 2(2 value is the ideal case). Based on this criterion, the $w_f = 0.1$ $w_g = 0.9$ case can be taken as the optimum deterministic lay-up configuration.

Furthermore, it is interesting to note in Table 4.8 that the flutter speed is 23.83 m/sec for w_f =0.9, 0.8, 0.7 and 0.6 even though these points correspond to a large spread of orientations θ_1 ,θ_2 and θ_3. For all these w_f values, similar ratios of torsional stiffness (D_{66}) to bending stiffness

(D_{11}) ~0.33, and bend-torsional stiffness (D_{16}) to bending stiffness (D_{11}) ~ -0.4, can be seen leading to the same flutter speed.

4.5 Conclusions

1. Binary GA and PSO codes are derived and employed individually to optimise the Flutter/Divergence speed. In either approach, we get quite a similar value of D_{66}/D_{11} and D_{16}/D_{11} for the optimised designs.
2. PSO is adopted to predict passive Gust Alleviated design and it has been found that these designs have poor flutter/divergence speed. One of the reason is lack of the torsional stiffness i.e. ratio of D_{66}/D_{11} and D_{16}/D_{11} is small compared to other designs.
3. Passive Gust Alleviated design (fibre lay-up which has D_{16}/D_{11} positive sign) exhibit that when gust is encountered then the leading edge deflection is more compared to the trailing edge such phenomenon is often called as washout phenomenon.
4. BGA showed higher scatter of fibre angles results compared with the PSO results; hence, PSO is a better method compared with BGA.
5. A multi-objective (objective one is to maximise the Flutter/Divergence speed and objective two is to minimise the Root Bending Moment) is formulated in the same cost function to find a best design which came from the best Pareto Frontier Design.

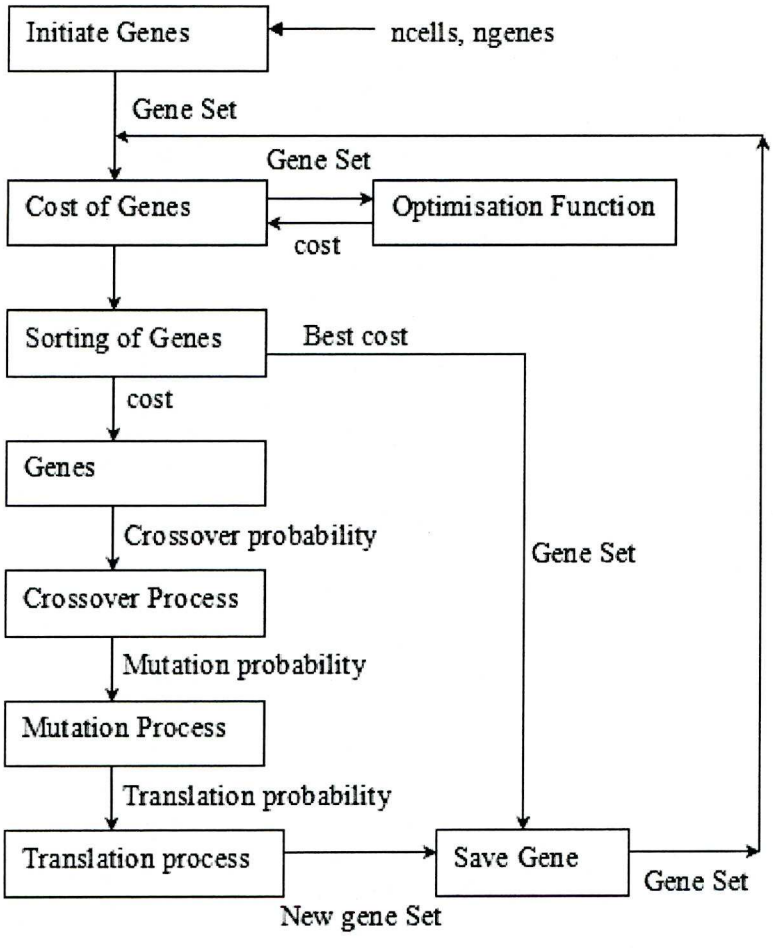

Figure 4.1: Flow chart of the BGA

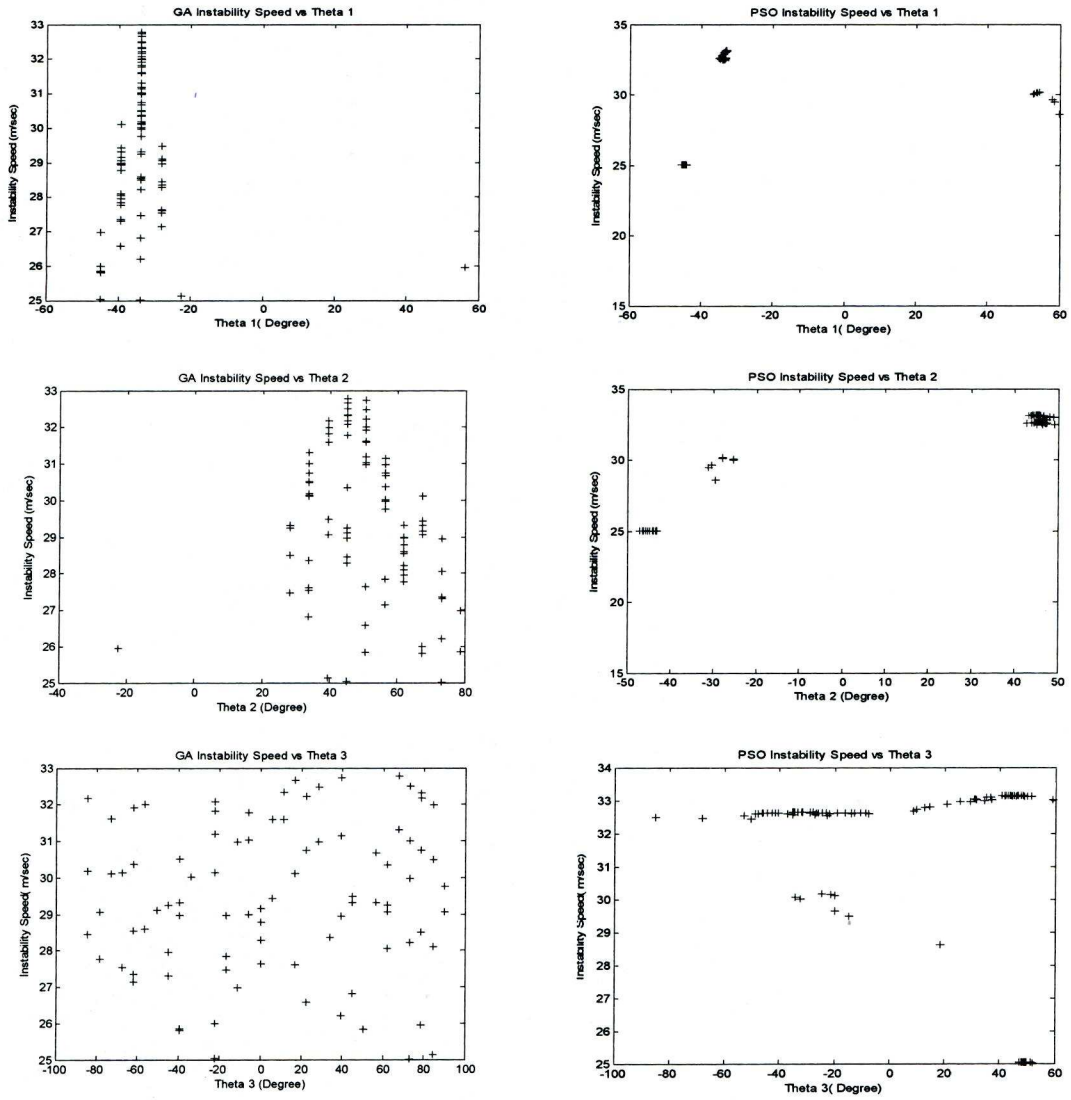

Figure 4.2: BGA and PSO Maximum Flutter Speeds for θ_1, θ_2 and θ_3

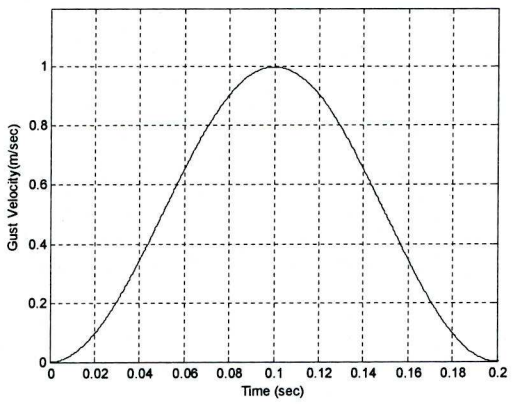

Figure 4.3: Gust Signal

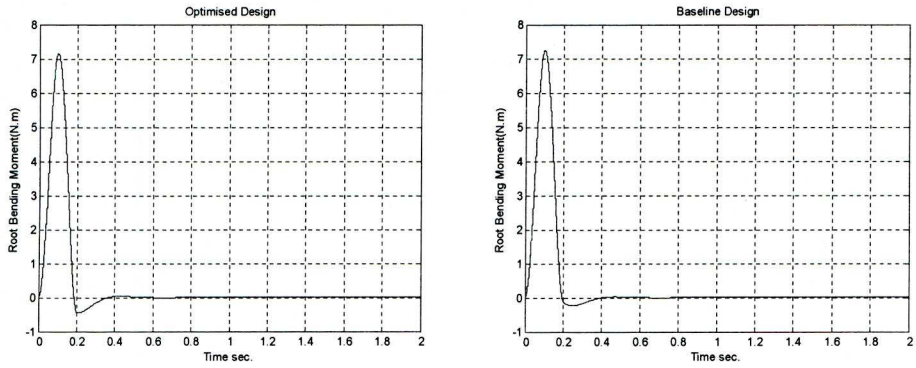

Figure 4.4: Root Bending Moment due to Gust

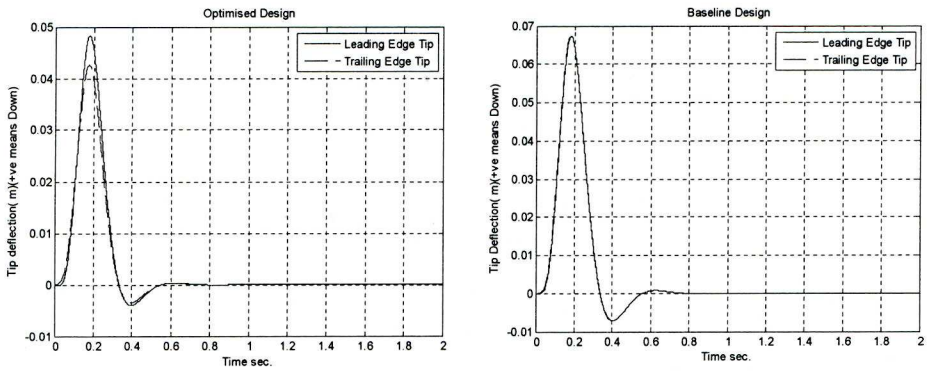

Figure 4.5: Leading and Trailing Edge Deflections

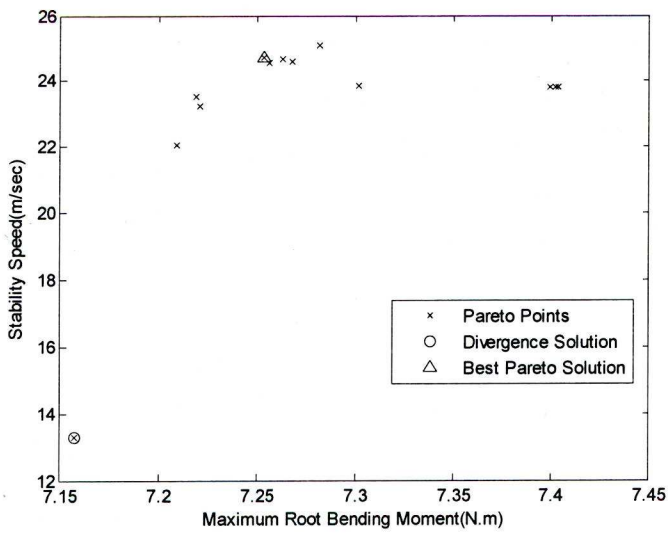

Figure 4.6: Deterministic Pareto Curve

Real	0	1	2	3	4	5	6	7
Binary	000	001	010	011	100	101	110	111
Theta(°)	-67.5	-45	-22.5	0	22.5	45	67.5	90

Table 4.1: Real, binary and theta representation for Ply angle

Best Speed (m/sec)	Θ_1 (deg)	θ_2(deg)	θ_3 (deg)
32.7660	-33.75	45	67.5

Table 4.2: Best Speed and Orientation $[(-33.75/45/67.5)_s]$for 100 solutions (Binary GA).

	D_{11}	D_{16}	D_{66}
BGA	2.0269	-0.5888	1.0008

Table 4.3: Bending, Bend-Torsion and Torsion Stiffness terms(BGA)

Best Speed (m/sec)	Θ_1 (deg)	θ_2(deg)	θ_3 (deg)
33.1330	-33.08	44.26	48.34

Table 4.4: Best Speed and Orientations$[(-33.08/44.26/48.34)_s]$ for 100 solutions (PSO)

	D_{11}	D_{16}	D_{66}
PSO	2.1078	-0.5638	1.0059

Table 4.5: Bending, Bend-Torsion and Torsion stiffness terms (PSO)

Flutter/Div Speed (m/sec)	RBM (N.m)	θ_1 (°)	θ_2 (°)	θ_3 (°)
13.29	7.157	18.47	1.64	-62.47
24.4*	7.26*	-45*	45*	0*

* Represents baseline design

Table 4.6: Passive Gust Alleviated Design (PSO)

w_f	w_g	Flutter/Div. Speed (m/sec)	Root Bending Moment (N.m)	θ_1 (°)	θ_2 (°)	θ_3 (°)
1.0	0.0	25.07	7.282	-42.4	47.96	-44.13
0.9	0.1	23.83	7.402	-23.52	-35.3	47.52
0.8	0.2	23.83	7.403	-24.31	-34.34	47.034
0.7	0.3	23.83	7.399	-34.94	-22.55	45.64
0.6	0.4	23.83	7.403	-33.11	-24.52	45.27
0.5	0.5	24.66	7.263	-45.35	43.55	-20.14
0.4	0.6	24.56	7.256	43.52	-45.41	-12.82
0.3	0.7	24.60	7.268	-43.53	44.85	-13.46
0.2	0.8	23.86	7.302	-38.69	1.60	55.60
0.1	**0.9**	**24.73**	**7.253**	**-45.73**	**40.08**	**-45.72**
0.03	0.97	23.54	7.219	31.10	-36.57	30.96
0.02	0.98	23.22	7.221	-38.66	29.03	28.36
0.01	0.99	22.06	7.209	24.50	-35.94	24.30
0.0	1.0	13.29	7.157	18.47	1.64	-62.47

Table 4.7: Results of Deterministic Pareto Curve

w_f	w_g	D_{11} (N.m)	D_{16} (N.m)	D_{66} (N.m)	D_{66} / D_{11}	D_{16} / D_{11}
0.9	0.0	12.1184	-4.8096	4.0137	0.331	-0.397
0.8	0.2	12.1513	-4.8628	4.0286	0.331	-0.400
0.7	0.3	12.1918	-4.7651	3.9964	0.328	-0.391
0.6	0.4	12.2265	-4.8848	4.0329	0.33	-0.40

Table 4.8: Stiffness terms for Optimum Design

Chapter 5

Uncertainty Theories, Modelling and their Application

5.1 Introduction

Traditional deterministic aeroelastic design approaches use safety factors and worst-case design scenarios to account for uncertainties, consequently produce designs which are either conservative (inefficient and overcompensated) or unknowingly dangerous designs[35] due to inherent uncertainties. Shortcomings of the deterministic approaches can be addressed through the use of either probabilistic or non-probabilistic approaches by including the uncertainties and then quantifying the measure of stability of the aeroelastic systems[25, 81, 82].

Various uncertainty theories [36-38, 41]can be applied to account for uncertainties in the structural properties. The selection of which uncertainty theory to use depends mainly upon the available information; if the uncertainty can be modelled as following some sort of distribution then probabilistic theory can be applied. When information is scarce, or only bounds of the uncertainty are known, then non-probabilistic theory can be a choice. In either of these probabilistic or non-probabilistic approaches, bounds on aeroelastic stability and response can be calculated which then can be utilized to produce a reliable and robust design [25, 81].

In this chapter, two approaches are developed to predict the bounds on aeroelastic stability and response, namely

- Polynomial Chaos Expansion Method(PCE)- A probabilistic Approach
    - PCE- Regression Analysis
    - PCE- Statistically Averaging Method(SAM)
- Interval Analysis Approach
    - Non-probabilistic Approach
    - Probabilistic Approach

These approaches will then be tested on various types of the wing models to predict the bounds on the Flutter/ Divergence Speed and variation in the Root Bending Moment (RBM) arising due to "1-Cosine" discrete gust by considering uncertainties in the material properties, fibre angle and thickness. Frequency Response Function bounds are also predicted using the PCE approach. Results predicted by these approaches are compared with Monte Carlo Simulation for validation.

5.2 Polynomial Chaos Expansion Method

Polynomial chaos is an approach that exploits a polynomial based stochastic space for the uncertainty representation and propagation defined with the PDFs. Norbert Weiner [42], first introduced this concept by representing the irregularities of the process (such as Brownian motion of the pollen particles on the surface of water) with homogenous chaos.

Ghanem and Spanos [43, 44] proposed a convergent series for the definition of the Polynomial Chaos Expansion (PCE) in the form

$$u(\theta) = a_0\Gamma_0 + \sum_{i1=1}^{\infty} a_{i1}\Gamma_1(\xi_{i1}(\theta)) + \sum_{i1=1}^{\infty}\sum_{i2=1}^{i1} a_{i1i2}\Gamma_2[\xi_{i1}(\theta),\xi_{i2}(\theta)] + \sum_{i1=1}^{\infty}\sum_{i2=1}^{i1}\sum_{i3=1}^{i2} a_{i1i2i3}\Gamma_3[\xi_{i1}(\theta),\xi_{i2}(\theta),\xi_{i3}(\theta)] + \ldots \quad (5.1)$$

in which $\{\xi_{i1}(\theta)\}_1^{\infty}$ denotes a set of independent standard Gaussian random variables and $\Gamma_p[\xi_{i1}(\theta).....\xi_{ip}(\theta)]$ is a set of multidimensional Hermite polynomials of order p, $a_{i1}.....a_{ip}$ are deterministic coefficients and θ is used to represent the randomness. We write PCE expression defined in Equation(5.1) as using only the first five terms

$$u = \beta_0 + \beta_1\xi + \beta_2(\xi^2 - 1) + \beta_3(\xi^3 - 3\xi) + \beta_4(\xi^4 - 6\xi^2 + 3) + \ldots\ldots \quad (5.2)$$

in which $a_{i1}.....a_{ip}$ are represented by β_i terms (i=1,2,3...N) and $\Gamma_p[\xi_{i1}(\theta).....\xi_{ip}(\theta)]$ represented with ξ terms. In equation(5.2), the first two terms are Gaussian and rest are non-Gaussian. When the input uncertain variables are Gaussian then equation(5.2) reduces to

$$u = \beta_0 + \beta_1\xi \quad (5.3)$$

and rearranging it leads to

$$\xi = \frac{(u-\beta_0)}{\beta_1} \quad (5.4)$$

where β_0 and β_1 are mean and standard deviation of random variable respectively. It can also be envisaged as unit normalization of the input random variable. The standard deviation represents scatter of the

variable, and hence defines the maximum and minimum values of ξ can be determined for some given probability.

In a similar way, the output response of the system can be assumed to contain the same Polynomial Chaos Expansion already defined in equation(5.2). If we retain only first two terms of PCE (i.e. involving β_0 and β_1 terms) this means that the output response is Gaussian. However, if we include higher terms also, then this means that the output response is non-Gaussian.

Furthermore, if the PDF of the uncertain variables are Gaussian then we can use a Hermit Polynomial to represent these variables. In case, PDF is not Gaussian, other polynomials may be used [45]such as Legendre and Jacobi polynomial etc.(See Table 5.1)

5.2.1 Generation of Hermite Polynomial Expressions

The work here first defines the meaning of the Chaos dimension. Chaos with one uncertain variable (such as the longitudinal Young's modulus) is 1-D while with two uncertain variables it is referred to as a 2-D Chaos. n-D Chaos will then be for "n" number of uncertain variables (such as fibre orientation angle, laminate thickness, longitudinal, transverse and shear moduli, crack density etc.). Since the chaos is represented with polynomials, the model developed will be referred to as a Polynomial Chaos Expansion (PCE) Model.

The order of the PCE model, whether it is 1-D, 2-D or n-D Chaos, is identified from the maximum power of ξ. ξ here represents the array of the uncertain variables. With ξ a of power two, it is a second order PCE model and so on.

To derive the PCE model for the output response of any dimension and order, polynomials Γ_p, which are orthogonal, are required in the from, [43]

$$\Gamma_p\left[\xi_{i1},.....\xi_{ip}\right]=(-1)^p e^{\frac{1}{2}\xi^T\xi}\frac{\partial^p}{\partial\xi_{i1},...\partial\xi_{ip}}\left[e^{-\frac{1}{2}\xi^T\xi}\right] \tag{5.5}$$

where $\{\xi\}$ contains a vector of "n" variables i.e. $\{\xi_k\}^n_{k=1}$ and k=1,2,3..n and p is the order of the Chaos.

1-Dimensional Polynomial Chaos model

In order to demonstrate the PCE models that are required for different dimensions and order, consider first the 1-D Polynomial Chaos model obtained by expanding equation (5.5) there only the first three terms (p=0, 1, 2) are calculated, and further terms can be determined in a similar way)[43]

$$\Gamma_0=1$$

$$\Gamma_1=(-1)^1 e^{\frac{1}{2}\xi_1^T\xi_1}\frac{\partial}{\partial\xi_1}e^{-\frac{1}{2}\xi_1^T\xi_1}=(-1)^1 e^{\frac{1}{2}\xi_1^2}\frac{\partial}{\partial\xi_1}e^{-\frac{1}{2}\xi_1^2}=(-1)^1\frac{\partial}{\partial\xi_1}(-\frac{1}{2}\xi_1^2)=\xi_1$$

$$\Gamma_2=(-1)^2 e^{\frac{1}{2}\xi_1^T\xi_1}\frac{\partial^2}{\partial^2\xi_1}e^{-\frac{1}{2}\xi_1^T\xi_1}=-e^{\frac{1}{2}\xi_1^2}\left(\frac{\partial}{\partial\xi_1}\left(\xi_1 e^{-\frac{1}{2}\xi_1^2}\right)\right)=-e^{\frac{1}{2}\xi_1^2}\left[e^{-\frac{1}{2}\xi_1^2}+\xi_1 e^{-\frac{1}{2}\xi_1^2}\frac{\partial}{\partial\xi_1}\left(-\frac{1}{2}\xi_1^2\right)\right] \tag{5.6}$$

$$=-e^{\frac{1}{2}\xi_1^2}\left[e^{-\frac{1}{2}\xi_1^2}-\xi_1^2 e^{-\frac{1}{2}\xi_1^2}\right]=\xi_1^2-1$$

Similarly, $\Gamma_3=\xi_1^3-3\xi_1$, $\Gamma_4=\xi_1^4-6\xi_1^2+3$, $\Gamma_5=\xi_1^5-10\xi_1^3+15\xi_1$ and $\Gamma_6=\xi_1^6-15\xi_1^4+45\xi_1^2-15$. From these calculated polynomials, we can formulate by multiplying each polynomial by unknown coefficients β_i the 1-D PCE models of order=1, 2, 3,4,5,6 as follows (say output

response is the flutter speed "$V_{f_{ij}}$") where i=Order of chaos and j=Dimension of chaos

1st Order 1-D PCE Model

$$V_{f_{11}} = \beta_0 + \beta_1 \xi_1$$

2nd Order 1-D PCE Model

$$V_{f_{21}} = \beta_0 + \beta_1 \xi_1 + \beta_2 \left(\xi_1^2 - 1\right)$$

3rd Order 1-D PCE Model

$$V_{f_{31}} = \beta_0 + \beta_1 \xi_1 + \beta_2 \left(\xi_1^2 - 1\right) + \beta_3 \left(\xi_1^3 - 3\xi_1\right)$$

4th Order 1-D PCE Model

$$V_{f_{41}} = \beta_0 + \beta_1 \xi_1 + \beta_2 \left(\xi_1^2 - 1\right) + \beta_3 \left(\xi_1^3 - 3\xi_1\right) + \beta_4 \left(\xi_1^4 - 6\xi_1^2 + 3\right)$$

5th Order 1-D PCE Model

$$V_{f_{51}} = \beta_0 + \beta_1 \xi_1 + \beta_2 \left(\xi_1 - 1\right) + \beta_3 \left(\xi_1^3 - 3\xi_1\right) + \beta_4 \left(\xi_1^4 - 6\xi_1^2 + 3\right) + \beta_5 \left(\xi_1^5 - 10\xi_1^3 + 15\xi_1\right)$$

6th Order 1-D PCE Model

$$V_{f_{61}} = \beta_0 + \beta_1 \xi_1 + \beta_2 \left(\xi_1^2 - 1\right) + \beta_3 \left(\xi_1^3 - 3\xi_1\right) + \beta_4 \left(\xi_1^4 - 6\xi_1^2 + 3\right) + \beta_5 \left(\xi_1^5 - 10\xi_1^3 + 15\xi_1\right) + \ldots$$
$$\beta_6 \left(\xi_1^6 - 15\xi_1^4 + 45\xi_1^2 - 15\right)$$

2-Dimensional Polynomial Chaos model

Consider the case when there are two uncertain variables (say longitudinal Young's modulus and thickness of the plate represented by ξ_1 and ξ_2), then equation (5.5) reduces to (only the first six terms (p=0, 1, 2) are calculated, and further terms can be determined in a similar way)[43], when there is more than one variable, interaction terms can arise, for example, for ξ_1 and ξ_2),[43]. Interaction terms are representing the interaction of uncertain parameters and likely to capture the effect (if any) on the overall response of the system. β coefficients (obtained after the regression analysis) relating to these

terms are likely to be of minimal value(s) when the contribution of such interaction towards the overall response is small.

$$\Gamma_0 = 1$$

$$\Gamma_1(\xi_1) = (-1)^1 e^{\frac{1}{2}(\xi_1^2+\xi_2^2)} \frac{\partial}{\partial \xi_1} e^{-\frac{1}{2}(\xi_1^2+\xi_2^2)} = (-1)^1 e^{\frac{1}{2}(\xi_1^2+\xi_2^2)} \frac{\partial}{\partial \xi_1} e^{-\frac{1}{2}(\xi_1^2+\xi_2^2)} = (-1)^1 \frac{\partial}{\partial \xi_1}(-\frac{1}{2}\xi_1^2) = \xi_1$$

$$\Gamma_1(\xi_2) = (-1)^1 e^{\frac{1}{2}(\xi_1^2+\xi_2^2)} \frac{\partial}{\partial \xi_2} e^{-\frac{1}{2}(\xi_1^2+\xi_2^2)} = (-1)^1 e^{\frac{1}{2}(\xi_1^2+\xi_2^2)} \frac{\partial}{\partial \xi_2} e^{-\frac{1}{2}(\xi_1^2+\xi_2^2)} = (-1)^1 \frac{\partial}{\partial \xi_2}(-\frac{1}{2}\xi_2^2) = \xi_2$$

$$\Gamma_2(\xi_1) = (-1)^2 e^{\frac{1}{2}(\xi_1^2+\xi_2^2)} \frac{\partial^2}{\partial^2 \xi_1} e^{-\frac{1}{2}(\xi_1^2+\xi_2^2)} = -e^{\frac{1}{2}(\xi_1^2+\xi_2^2)} \left(\frac{\partial}{\partial \xi_1} \left(\xi_1 e^{-\frac{1}{2}(\xi_1^2+\xi_2^2)} \right) \right)$$

$$= -e^{\frac{1}{2}(\xi_1^2+\xi_2^2)} \left[e^{-\frac{1}{2}(\xi_1^2+\xi_2^2)} + \xi_1 e^{-\frac{1}{2}(\xi_1^2+\xi_2^2)} \frac{\partial}{\partial \xi_1} \left(-\frac{1}{2}\left(\xi_1^2+\xi_2^2\right) \right) \right]$$

$$= -e^{\frac{1}{2}(\xi_1^2+\xi_2^2)} \left[e^{-\frac{1}{2}(\xi_1^2+\xi_2^2)} - \xi_1^2 e^{-\frac{1}{2}(\xi_1^2+\xi_2^2)} \right] = \xi_1^2 - 1$$

$$\Gamma_2(\xi_1,\xi_2) = (-1)^2 e^{\frac{1}{2}(\xi_1^2+\xi_2^2)} \frac{\partial^2}{\partial \xi_1 \xi_2} e^{-\frac{1}{2}(\xi_1^2+\xi_2^2)} = -e^{\frac{1}{2}(\xi_1^2+\xi_2^2)} \left(\frac{\partial}{\partial \xi_1} \left(\xi_2 e^{-\frac{1}{2}(\xi_1^2+\xi_2^2)} \right) \right)$$

$$= -e^{\frac{1}{2}(\xi_1^2+\xi_2^2)} \left[\xi_2 e^{-\frac{1}{2}(\xi_1^2+\xi_2^2)} \frac{\partial}{\partial \xi_1} \left(-\frac{1}{2}\left(\xi_1^2+\xi_2^2\right) \right) \right] = \xi_1 \xi_2$$

$$\Gamma_2(\xi_2) = (-1)^2 e^{\frac{1}{2}(\xi_1^2+\xi_2^2)} \frac{\partial^2}{\partial^2 \xi_2} e^{-\frac{1}{2}(\xi_1^2+\xi_2^2)} = -e^{\frac{1}{2}(\xi_1^2+\xi_2^2)} \left(\frac{\partial}{\partial \xi_2} \left(\xi_2 e^{-\frac{1}{2}(\xi_1^2+\xi_2^2)} \right) \right)$$

$$= -e^{\frac{1}{2}(\xi_1^2+\xi_2^2)} \left[e^{-\frac{1}{2}(\xi_1^2+\xi_2^2)} + \xi_2 e^{-\frac{1}{2}(\xi_1^2+\xi_2^2)} \frac{\partial}{\partial \xi_2} \left(-\frac{1}{2}\left(\xi_1^2+\xi_2^2\right) \right) \right]$$

$$= -e^{\frac{1}{2}(\xi_1^2+\xi_2^2)} \left[e^{-\frac{1}{2}(\xi_1^2+\xi_2^2)} - \xi_2^2 e^{-\frac{1}{2}(\xi_1^2+\xi_2^2)} \right] = \xi_2^2 - 1$$

Similarly, $\Gamma_3(\xi_1) = \xi_1^3 - 3\xi_1$, $\Gamma_3(\xi_1,\xi_2) = \xi_2\left(\xi_1^2-1\right) and \;\; \xi_1\left(\xi_2^2-1\right)$, and $\Gamma_3(\xi_2) = \xi_2^3 - 3\xi_2$. For the 3rd order case, but note that there are now two interaction terms depending upon whether the differentiation is $\frac{\partial^3}{\partial^2 \xi_1 \partial \xi_2}$ or $\frac{\partial^3}{\partial^2 \xi_2 \partial \xi_1}$.

From these calculated polynomials, we can then formulate by multiplying each polynomial by unknown coefficient β_i, the 2-D PCE models of order=1, 2, 3 as follows (say output response is the flutter speed "$V_{f_{ij}}$")

1st Order 2-D PCE Model

$$V_{f_{12}} = \beta_0 + \beta_1\xi_1 + \beta_2\xi_2$$

2nd Order 2-D PCE Model

$$V_{f_{22}} = \beta_0 + \beta_1\xi_1 + \beta_2\xi_2 + \beta_3\left(\xi_1^2 - 1\right) + \beta_4\xi_1\xi_2 + \beta_5\left(\xi_2^2 - 1\right)$$

3rd Order 2-D PCE Model

$$V_{f_{32}} = \beta_0 + \beta_1\xi_1 + \beta_2\xi_2 + \beta_3\left(\xi_1^2 - 1\right) + \beta_4\xi_1\xi_2 + \beta_5\left(\xi_2^2 - 1\right) + \ldots$$
$$+\beta_6\left(\xi_1^3 - 3\xi_1\right) + \beta_7\left(\xi_2\left(\xi_1^2 - 1\right)\right) + \beta_8\left(\xi_1\left(\xi_2^2 - 1\right)\right) + \beta_9\left(\xi_2^3 - 3\xi_2\right)$$

Generalisation of n-D and 1, 2 and 3rd Order PCE Models

For the case of n-D and 1st Order PCE model, one can write in general form as

$$V_{f_{1n}} = \beta_0 + \sum_{i=1}^{n}\left(\beta_i\xi_i\right) \tag{5.7}$$

Similarly, generalisation of n-D and 2nd Order PCE model can be written as

$$V_{f_{2n}} = \beta_0 + \sum_{i=1}^{n}\beta_i\xi_i + \sum_{i=1}^{n}\beta_{n+i}\left(\xi_i^2 - 1\right) + \left(\sum_{i=1}^{n}\beta_{2n+i}\ \ \xi_i\right)\left(\sum_{\substack{j=2 \\ j>i \\ j\neq i}}^{n}\xi_j\right) \tag{5.8}$$

n-D and 3rd Order PCE model will take the form as

$$V_{f_{3n}} = \beta_0 + \sum_{i=1}^{n} \beta_i \xi_i + \sum_{i=1}^{n} \beta_{n+i} \left(\xi_i^2 - 1\right) + \left(\sum_{i=1}^{n} \beta_{2n+i} \quad \xi_i \right) \left(\sum_{\substack{j=2 \\ j>i \\ j \neq i}}^{n} \xi_j \right) + \ldots$$

$$\sum_{i=1}^{n} \beta_{2n+i} \left(\xi_i^3 - 3\xi_i\right) + \left(\sum_{i=1}^{n} \beta_{3n+i} \quad \xi_i \right) \left(\sum_{\substack{j=1 \\ i \neq j}}^{n} \left(\xi_j^2 - 1\right) \right) + \ldots \qquad (5.9)$$

$$\left(\sum_{i=1}^{n} \beta_{5n+i} \quad \xi_i \right) \left(\sum_{j=2}^{n} \xi_j \right) \left(\sum_{\substack{l=3 \\ j \neq l \\ j>i \\ j \neq l \\ l>j}}^{n} \xi_l \right)$$

The equation (5.9) needs two vector arrays $\{\beta_i\}$ and $\{\xi_i\}$, in which $\{\xi_i\}$ is known (due to the known input Gaussian distribution based uncertainty) and $\{\beta_i\}$ is unknown. The sample based techniques such as the regression analysis or the statistically averaging method can be applied to calculate the unknown $\{\beta_i\}$ coefficients to finally know the PCE models[44, 47].From the various available sampling methods, an efficient Latin Hyper Cube sampling technique is applied and explained in the following section.

5.2.2 Latin Hypercube Sampling Technique

A regression analysis[47], for example, can predict the $\{\beta_i\}$ coefficients of the PCE model. The difficulty in this process is that we need a large number of $\{\xi_i\}$ samples and could be a problem for large order of the systems, because it is very much possible that the samples are clustered on any part of the PDF whereas we are interested on the high probability area and tails of the PDF as shown in Figure 5.1. We adopt Latin Hypercube sampling technique to overcome this difficulty. Latin

Hypercube samples take equal probability points on PDF ensuring to capture response on all PDF points and introduce minimum variance in the response[83].

However, if we are interested to produce PDF with a confidence level of 99 %, we can then emulate equation (5.2) after calculating $\{\beta_i\}$ terms as shown in Figure 5.2. Here regression analysis and statistical averaging method are presented to predict $\{\beta_i\}$ coefficients.

5.2.3 Determination of $\{\beta_i\}$ Coefficients-Regression Analysis

A regression model [47]is fitted based on the computed data to determine the unknown $\{\beta_i\}$ coefficients described, for example, in equation (5.9) relating the flutter speed or root bending moment to variations in Young's modulus. An efficient Latin Hypercube sampling technique was applied to ensure that the test cases cover all portions of the input variable range, produce relatively small variances of the response and that only relatively few cases need to be considered. The key steps are as follow

Step1: Latin Hypercube Sampling for input parameter

Suppose we have Longitudinal Young's modulus as an uncertain variable and are interested in the effect this has on the flutter speed, let us first generate its LHS samples. For every value of ξ, Longitudinal Young's modulus is calculated from equation(5.3).

Step2: Calculation of β_i coefficients

Having established ξ and corresponding Longitudinal Young's modulus, flutter speed of the wing is calculated by using the aeroelastic code developed in Chapter 3 or Finite Element Aeroelastic Model developed in NASTRAN. Suppose, we fit 2nd Order 1-D PCE model then following expression holds

$$V_{f_{21}} = \beta_0 + \beta_1 \xi_1 + \beta_2 \left(\xi_1^2 - 1\right) \tag{5.10}$$

In matrix form we can arrange it as

$$\begin{bmatrix} f_1 \\ f_2 \\ f_3 \\ f_4 \\ .. \\ f_n \end{bmatrix} = \begin{bmatrix} 1 & \xi_{s1} & \xi_{s1}^2 - 1 \\ 1 & \xi_{s2} & \xi_{s2}^2 - 1 \\ 1 & \xi_{s3} & \xi_{s3}^2 - 1 \\ 1 & \xi_{s4} & \xi_{s4}^2 - 1 \\ .. & .. & .. \\ 1 & \xi_{sn} & \xi_{sn}^2 - 1 \end{bmatrix} \begin{bmatrix} \beta_0 \\ \beta_1 \\ \beta_2 \end{bmatrix} \tag{5.11}$$

where n is number of samples and ξ_{s1} represents the 1st sample value of ξ_1. In equation(5.11), we know first ($[f_n]$) and ($\left[\Gamma(\xi)\right]$) second matrices, from which the unknown $\{\beta_i\}$ values can be calculated by solving the simultaneous linear equations.

Step 3: Formulation of the PCE Model

Having determined the regression model coefficients and then substituting these coefficients into equation(5.10), it is computationally efficient (increasingly so for more complicated FE structure or aerodynamic models) to use this model to emulate many different cases covering the variation of the uncertainty (different ξ values). A PDF of the resulting variation, say of the root bending moment or flutter speed,

can then be determined. The flow diagram shown in Figure 5.3 highlights the key steps involved in this method. Note that there is no restriction on the resulting distribution.

5.2.4 Determination of $\{\beta_i\}$ Coefficients- Statistical Averaging Method

The structure of the orthogonal polynomials can be exploited to find the $\{\beta_i\}$ coefficients by statistically averaging the response [44]. For example, consider 2^{nd} Order 1-D PCE model $V_{f21} = \beta_0 + \beta_1\xi_1 + \beta_2\left(\xi_1^2 - 1\right)$. In this model, $\Gamma_p = 1, \xi_1, \xi_1^2 - 1$ and three unknown $\{\beta_i\}$ coefficients are $\beta_0, \beta_1, \beta_2$. In order to find these coefficients, we need three equations, which can be formulated by multiplying one by one each Γ_p to the V_{f21} model and then taking the expected value operation of the product as follows

$$\begin{aligned}
&(1)\beta_0 = (1)V_{f21} - (1)\beta_1\xi_1 - (1)\beta_2\left(\xi_1^2 - 1\right) \Rightarrow \\
&\langle\beta_0\rangle = \langle V_{f21}\rangle - \langle\beta_1\xi_1\rangle - \langle\beta_2\left(\xi_1^2 - 1\right)\rangle \Rightarrow \\
&\beta_0 = \langle V_{f21}\rangle - 0 - 0 = \langle V_{f21}\rangle
\end{aligned} \tag{5.12}$$

Where $\langle\ \rangle$ represents the expected value operation and $\langle\xi_1\rangle = 0$, $\langle\xi_1^2\rangle = 1$.

The equation (5.12) means that take the mean value of V_{f21} obtained from all the Latin Hyper Cube Samples.

Similarly, we can write β_1 as follows (in this case $\Gamma_1 = \xi_1$ which will be multiplied to the V_{f21} model)

$$(\beta_1\xi_1)\xi_1 = (\xi_1)V_{f21} - (\xi_1)(1)\beta_0 - \beta_2(\xi_1)(\xi_1^2 - 1) \Rightarrow$$

$$\beta_1 = \frac{\langle(\xi_1)(V_{f21})\rangle}{\langle\xi_1^2\rangle} \tag{5.13}$$

Denominator of the equation (5.13) is known exactly (=1) whereas numerator can be calculated by taking the expected value operation of the product of each realisation of LHS and the corresponding flutter speed.

By following the same procedure we can write the β_2 as follows

$$\beta_2(\xi_1^2 - 1)(\xi_1^2 - 1) = (\xi_1^2 - 1)V_{f21} - \beta_0(\xi_1^2 - 1)(1) - \beta_1(\xi_1)(\xi_1^2 - 1) \Rightarrow$$

$$\beta_2 = \frac{\langle(\xi_1^2 - 1)(V_{f21})\rangle}{\langle(\xi_1^2 - 1)^2\rangle} \tag{5.14}$$

Denominator of equation (5.14) is known exactly (=2) and numerator can be calculated by taking the expected value operation of the involved product variables.

The denominator conditions are tested against the sample size i.e. when the LHS are 120, $\langle\xi_1^2\rangle = 0.9917$ and $\langle(\xi_1^2 - 1)^2\rangle = 1.7247$, whereas these should be 1 and 2 respectively. The difference becomes almost zero for 20,000 samples i.e. both comes out to be 0.9999 and 2.0003 respectively. Consequently, one obvious reason of taking less samples is that the β_2 coefficient will have a discrepancy whereas for β_1 it should be minimal.

Convergence study for regression and SAM approaches

A convergence study for the $\{\beta_i\}$ coefficients obtained from the PCE-regression and PCE-SAM approaches is conducted. A wind tunnel model of the composite wing model 2 with the lay-up configuration of $(-40,-20,15,0,-45,-45)_s$ is chosen as a test case. The longitudinal Young's Modulus is the uncertain variable, has a Gaussian PDF with a 0.03 coefficient of variation. Results for the $\{\beta_i\}$ coefficients for the various values of LHS are shown in Table 5.2. β_0 coefficient is same in both the approaches, while β_1 has a minimal and β_2 has a large discrepancies. It can be concluded that the PCE-SAM must have β_0 and β_1 terms only, as an approximation, if applied to predict the flutter PDF.

5.2.5 Application of PCE Method- A Regression Analysis Approach

In this section, the PCE method with regression analysis is applied to following wing models

- Wind tunnel model of the composite wing
- More realistic full scale aircraft composite wing FE model
- The Goland wing

Example 1a: Flutter and RBM PDF for wind tunnel model of the composite wing

In order to demonstrate the concept, we analyse the wind tunnel composite wing model 2 with a total of 12 composite layers with lay-up

configuration of $(-40,-20,15,0,-45,-45)_s$. The longitudinal Young's Modulus is the uncertain variable with a coefficient of variation of 0.03, mean value 98GPa and has a Gaussian distribution. Various Orders of PCE models were tested for prediction of the flutter speed PDF, such as

$$V_{f11} = \beta_0 + \beta_1\xi_1 ;\ V_{f21} = \beta_0 + \beta_1\xi_1 + \beta_2\left(\xi_1^2 - 1\right) ;$$

$$V_{f31} = \beta_0 + \beta_1\xi_1 + \beta_2\left(\xi_1^2 - 1\right) + \beta_3\left(\xi_1^3 - 3\xi_1\right);$$

$$V_{f41} = \beta_0 + \beta_1\xi_1 + \beta_2\left(\xi_1^2 - 1\right) + \beta_3\left(\xi_1^3 - 3\xi_1\right) + \beta_4\left(\xi_1^4 - 6\xi_1^2 + 3\right) \qquad (5.15)$$

The $\{\beta_i\}$ coefficients were calculated for 20 LHS realisations and are given in Table 5.3. PDF plots are shown in Figure 5.4a and we get similar PDF plots for various orders of PCE models.10,000 Monte Carlo Simulation were conducted to validate the results predicted by the PCE-Regression Models and a very good agreement of PDF predicted by 2nd Order PCE and MCS (10,000) is observed (see Figure 5.4b).

Various Orders of the PCE models for prediction of the Root Bending Moment (RBM) PDF were also tested (same as defined in the equation (5.15) except that the RBM is now on the left hand side). The input gust signal is shown in the Figure 3.11b.

$\{\beta_i\}$ coefficients are calculated for 20 LHS realisations and are given in Table 5.4.PDF plots are shown in Figure 5.5a and we obtain similar PDF plots for various orders of PCE models. Monte Carlo Simulation is conducted to validate the RBM results predicted by PCE-Regression Model and a very good agreement of PDF predicted by 2nd Order PCE and MCS (10,000) is observed (see Figure 5.5b)

Example 2: Flutter PDF for full-scale aircraft composite wing

As a more realistic test case, the full-scale composite wing finite element model 4 was implemented. Table 3.3 defines the lay-up orientation and material properties of the composite layers that were used. The longitudinal Young's modulus was treated as uncertain variable with coefficient of variation of 0.02 and mean value of 140GPa. 20 LHS samples were considered to build PCE model. 1200 MCS were conducted and the PDFs of the PCE model and MCS are shown in Figure 5.6. Mean flutter speed and standard deviation are shown in Table 5.5. The results showed an excellent agreement.

Example 3: Flutter PDF for the Goland wing

Finally, the PCE Method was applied to the Goland wing model 3 (see Figure 3.3. A 7-D chaos model is required as there are seven uncertain variables, their upper, lower and mean values are given in Table 5.6. Three PCE models are fitted;

1st Order

$$V_{f17} = \beta_0 + \beta_1\xi_1 + \beta_2\xi_2 + \beta_3\xi_3 + \beta_4\xi_4 + \beta_5\xi_5 + \beta_6\xi_6 + \beta_7\xi_7 \qquad (5.16)$$

2nd Order PCE

$$\begin{aligned} V_{f27} = {} & \beta_0 + \beta_1\xi_1 + \beta_2\xi_2 + \beta_3\xi_3 + \beta_4\xi_4 + \beta_5\xi_5 + \beta_6\xi_6 + \beta_7\xi_7 + \beta_8\left(\xi_1^2 - 1\right) + \ldots \\ & \beta_9\xi_1\xi_2 + \beta_{10}\xi_1\xi_3 + \beta_{11}\xi_1\xi_4 + \beta_{12}\xi_1\xi_5 + \beta_{13}\xi_1\xi_6 + \beta_{14}\xi_1\xi_7 + \beta_{15}\left(\xi_2^2 - 1\right) + \ldots \\ & \beta_{16}\xi_2\xi_3 + \beta_{17}\xi_2\xi_4 + \beta_{18}\xi_2\xi_5 + \beta_{19}\xi_2\xi_6 + \beta_{20}\xi_2\xi_7 + \beta_{21}\left(\xi_3^2 - 1\right) + \ldots \\ & \beta_{22}\xi_3\xi_4 + \beta_{23}\xi_3\xi_5 + \beta_{24}\xi_3\xi_6 + \beta_{25}\xi_3\xi_7 + \beta_{26}\left(\xi_4^2 - 1\right) + \beta_{27}\xi_4\xi_5 + \ldots \\ & \beta_{28}\xi_4\xi_6 + \beta_{29}\xi_4\xi_7 + \beta_{30}\left(\xi_5^2 - 1\right) + \beta_{31}\xi_5\xi_6 + \beta_{32}\xi_5\xi_7 + \beta_{33}\left(\xi_6^2 - 1\right) + \ldots \\ & \beta_{34}\xi_6\xi_7 + \beta_{35}\left(\xi_7^2 - 1\right) \end{aligned} \qquad (5.17)$$

In order to examine the effects of more $\{\beta_i\}$ coefficient terms on the tails of flutter speed PDF, PCE model is extended to the 3rd order. Because of involved seven uncertain variables, its expression is quite long and is given below

$$
\begin{aligned}
V_{f_{37}} &= \beta_0 + \beta_1\xi_1 + \beta_2\xi_2 + \beta_3\xi_3 + \beta_4\xi_4 + \beta_5\xi_5 + \beta_6\xi_6 + \beta_7\xi_7 + \beta_8\left(\xi_1^2 - 1\right) + \beta_9\xi_1\xi_2 + \ldots \\
&\beta_{10}\xi_1\xi_3 + \beta_{11}\xi_1\xi_4 + \beta_{12}\xi_1\xi_5 + \beta_{13}\xi_1\xi_6 + \beta_{14}\xi_1\xi_7 + \beta_{15}\left(\xi_2^2 - 1\right) + \beta_{16}\xi_2\xi_3 + \beta_{17}\xi_2\xi_4 + \ldots \\
&\beta_{18}\xi_2\xi_5 + \beta_{19}\xi_2\xi_6 + \beta_{20}\xi_2\xi_7 + \beta_{21}\left(\xi_3^2 - 1\right) + \beta_{22}\xi_3\xi_4 + \beta_{23}\xi_3\xi_5 + \beta_{24}\xi_3\xi_6 + \beta_{25}\xi_3\xi_7 + \ldots \\
&\beta_{26}\left(\xi_4^2 - 1\right) + \beta_{27}\xi_4\xi_5 + \beta_{28}\xi_4\xi_6 + \beta_{29}\xi_4\xi_7 + \beta_{30}\left(\xi_5^2 - 1\right) + \beta_{31}\xi_5\xi_6 + \beta_{32}\xi_5\xi_7 + \ldots \\
&\beta_{33}\left(\xi_6^2 - 1\right) + \beta_{34}\xi_6\xi_7 + \beta_{35}\left(\xi_7^2 - 1\right) + \beta_{36}\left(\xi_1^3 - 3\xi_1\right) + \beta_{37}\left(\xi_1^2\xi_2 - \xi_2\right) + \beta_{38}\left(\xi_1^2\xi_3 - \xi_3\right) + \ldots \\
&\beta_{39}\left(\xi_1^2\xi_4 - \xi_4\right) + \beta_{40}\left(\xi_1^2\xi_5 - \xi_5\right) + \beta_{41}\left(\xi_1^2\xi_6 - \xi_6\right) + \beta_{42}\left(\xi_1^2\xi_7 - \xi_7\right) + \beta_{43}\left(\xi_2^3 - 3\xi_2\right) + \ldots \\
&\beta_{44}\left(\xi_2^2\xi_1 - \xi_1\right) + \beta_{45}\left(\xi_2^2\xi_3 - \xi_3\right) + \beta_{46}\left(\xi_2^2\xi_4 - \xi_4\right) + \beta_{47}\left(\xi_2^2\xi_5 - \xi_5\right) + \beta_{48}\left(\xi_2^2\xi_6 - \xi_6\right) + \ldots \\
&\beta_{49}\left(\xi_2^2\xi_7 - \xi_7\right) + \beta_{50}\left(\xi_3^3 - 3\xi_3\right) + \beta_{51}\left(\xi_3^2\xi_1 - \xi_1\right) + \beta_{52}\left(\xi_3^2\xi_2 - \xi_2\right) + \beta_{53}\left(\xi_3^2\xi_4 - \xi_4\right) + \ldots \\
&\beta_{54}\left(\xi_3^2\xi_5 - \xi_5\right) + \beta_{55}\left(\xi_3^2\xi_6 - \xi_6\right) + \beta_{56}\left(\xi_3^2\xi_7 - \xi_7\right) + \beta_{57}\left(\xi_4^3 - 3\xi_4\right) + \beta_{58}\left(\xi_4^2\xi_1 - \xi_1\right) + \ldots \\
&\beta_{59}\left(\xi_4^2\xi_2 - \xi_2\right) + \beta_{60}\left(\xi_4^2\xi_3 - \xi_3\right) + \beta_{61}\left(\xi_4^2\xi_5 - \xi_5\right) + \beta_{62}\left(\xi_4^2\xi_6 - \xi_6\right) + \beta_{63}\left(\xi_4^2\xi_7 - \xi_7\right) + \ldots \\
&\beta_{64}\left(\xi_5^3 - 3\xi_5\right) + \beta_{65}\left(\xi_5^2\xi_1 - \xi_1\right) + \beta_{66}\left(\xi_5^2\xi_2 - \xi_2\right) + \beta_{67}\left(\xi_5^2\xi_3 - \xi_3\right) + \beta_{68}\left(\xi_5^2\xi_4 - \xi_4\right) + \ldots \\
&\beta_{69}\left(\xi_5^2\xi_6 - \xi_6\right) + \beta_{70}\left(\xi_5^2\xi_7 - \xi_7\right) + \beta_{71}\left(\xi_6^3 - 3\xi_6\right) + \beta_{72}\left(\xi_6^2\xi_1 - \xi_1\right) + \beta_{73}\left(\xi_6^2\xi_2 - \xi_2\right) + \ldots \\
&\beta_{74}\left(\xi_6^2\xi_3 - \xi_3\right) + \beta_{75}\left(\xi_6^2\xi_4 - \xi_4\right) + \beta_{76}\left(\xi_6^2\xi_5 - \xi_5\right) + \beta_{77}\left(\xi_6^2\xi_7 - \xi_7\right) + \beta_{78}\left(\xi_7^3 - 3\xi_7\right) + \ldots \\
&\beta_{79}\left(\xi_7^2\xi_1 - \xi_1\right) + \beta_{80}\left(\xi_7^2\xi_2 - \xi_2\right) + \beta_{81}\left(\xi_7^2\xi_3 - \xi_3\right) + \beta_{82}\left(\xi_7^2\xi_4 - \xi_4\right) + \beta_{83}\left(\xi_7^2\xi_5 - \xi_5\right) + \ldots \\
&\beta_{84}\left(\xi_7^2\xi_6 - \xi_6\right) + \beta_{85}\left(\xi_1\xi_2\xi_3\right) + \beta_{86}\left(\xi_1\xi_2\xi_4\right) + \beta_{87}\left(\xi_1\xi_2\xi_5\right) + \beta_{88}\left(\xi_1\xi_2\xi_6\right) + \beta_{89}\left(\xi_1\xi_2\xi_7\right) + \ldots \\
&\beta_{90}\left(\xi_1\xi_3\xi_4\right) + \beta_{91}\left(\xi_1\xi_3\xi_5\right) + \beta_{92}\left(\xi_1\xi_3\xi_6\right) + \beta_{93}\left(\xi_1\xi_3\xi_7\right) + \beta_{94}\left(\xi_1\xi_4\xi_5\right) + \beta_{95}\left(\xi_1\xi_4\xi_6\right) + \ldots \\
&\beta_{96}\left(\xi_1\xi_4\xi_7\right) + \beta_{97}\left(\xi_1\xi_5\xi_6\right) + \beta_{98}\left(\xi_1\xi_5\xi_7\right) + \beta_{99}\left(\xi_1\xi_6\xi_7\right) + \beta_{100}\left(\xi_2\xi_3\xi_4\right) + \beta_{101}\left(\xi_2\xi_3\xi_5\right) + \ldots \\
&\beta_{102}\left(\xi_2\xi_3\xi_6\right) + \beta_{103}\left(\xi_2\xi_3\xi_7\right) + \beta_{104}\left(\xi_2\xi_4\xi_5\right) + \beta_{105}\left(\xi_2\xi_4\xi_6\right) + \beta_{106}\left(\xi_2\xi_4\xi_7\right) + \beta_{107}\left(\xi_2\xi_5\xi_6\right) + \ldots \\
&\beta_{108}\left(\xi_2\xi_5\xi_7\right) + \beta_{109}\left(\xi_2\xi_6\xi_7\right) + \beta_{110}\left(\xi_3\xi_4\xi_5\right) + \beta_{111}\left(\xi_3\xi_4\xi_6\right) + \beta_{112}\left(\xi_3\xi_4\xi_7\right) + \beta_{113}\left(\xi_3\xi_5\xi_6\right) + \ldots \\
&\beta_{114}\left(\xi_3\xi_5\xi_7\right) + \beta_{115}\left(\xi_4\xi_5\xi_6\right) + \beta_{116}\left(\xi_4\xi_5\xi_7\right) + \beta_{117}\left(\xi_4\xi_6\xi_7\right) + \beta_{118}\left(\xi_5\xi_6\xi_7\right)
\end{aligned}
\tag{5.18}
$$

As we increase order of the PCE model, the $\{\beta_i\}$ coefficients increase from 8 (for 1st Order PCE) to 119(for 3rd Order PCE). Generally, minimum numbers of LHS required are of generally the order of 3[63], which means that for the1st Order PCE model we need 24 LHS and for the 3rd Order PCE model we require 357 LHS. The $\{\beta_i\}$ coefficients from the PCE-Regression analysis are shown in Table 5.7 whereas the remaining $\{\beta_i\}$ coefficients for 3rd Oder PCE are shown in Table 5.8. PDF for 1st, 2nd and 3rd Order PCE-Regression models are shown in Figure 5.7 for 360 LHS. The mean flutter speed predicted by various orders of PCE models showed similar results. One of the main reasons

for this is that the $\{\beta_i\}$ coefficients for the higher order terms of the uncertain variables are of very small values.

5.2.6 Application of PCE Method- Statistical Averaging Method (SAM)

Example 1: Flutter PDF for the Goland wing model 3

Apply the PCE-SAM to the Goland wing with 120 and 360 LHS. PDF predicted by PCE-Regression and PCE-SAM are shown in Figure 5.8a and Figure 5.8b and an excellent agreement is noticed. In this case, increase in LHS size has not any significant affect on the flutter PDF. In case of 120 LHS, 2nd Order PCE, PCE-SAM and MCS are shown in Figure 5.8c. A very good agreement can be seen. PCE-SAM may be adopted as a quicker approximation.

5.3 Prediction of Uncertain Frequency Response Function Bounds-PCE Method

The frequency response function is the representation of the dynamic characteristic of the mechanical structure. The case considered here is the prediction of the bounds of the Frequency Response Function (FRF) of a given structure.

A Polynomial Chaos Expansion (PCE-Regression) method is used to predict uncertainty regression models of the various parameters that make up a curvefit of the FRF : natural frequencies, damping ratios, complex amplitudes, mass and stiffness residuals, by making use of an efficient Latin Hypercube technique. These uncertainty models are then combined to efficiently determine PDFs of the parameters and also the uncertainty bounds of the FRFs. The approach is demonstrated using two examples; a simple beam containing uncertainty in Young's

Modules, and a full-scale aircraft composite wing model containing uncertainties in both Young's modulus and the shear modulus. The results were compared with Monte Carlo Simulation (MCS) and it was found that the parameter PDFs and FRF error bounds obtained using a 2nd order PCE model agreed very well whilst requiring significantly less computation.

5.3.1 Mathematical Model- Formulation of Deterministic Frequency Response Function (FRF)

The equations of motion of a multi-degree of freedom vibration system can be modelled in the classical form [84] for response y to input force f as

$$[M]\underline{\ddot{y}} + [C]\underline{\dot{y}} + [K]\underline{y} = \underline{f} \tag{5.19}$$

where [M], [C] and [K] are the mass, damping and stiffness matrices respectively. The solution of the homogenous form of equation (5.19) can be used to determine the natural frequencies, damping ratios and corresponding mode shapes. However, assuming a harmonic input and response, the Frequency Response Function matrix H between sinusoidal forcing position f at frequency ω and output y is found as [84]

$$y(\omega) = H(\omega) f(\omega) \tag{5.20}$$

where the FRF matrix is defined as

$$H(\omega) = \left[K + i\omega C - \omega^2 M\right]^{-1} \tag{5.21}$$

It is common practice to fit the FRF between each input and output for the first n dominant modes in the form

$$H_f(\omega) \cong \sum_{i=1}^{n} \frac{A_i}{\omega_i^2 - \omega^2 + 2j\zeta_i\omega_i\omega} + A_r + \frac{B_r}{\omega^2} \tag{5.22}$$

in which A_i are the complex residues, and A_r and B_r are mass and stiffness residuals respectively and $H_f(\omega)$ is the fitted FRF. It is usual to perform a two stage procedure to identify the above model, firstly the frequencies and damping ratios are calculated either from the eigensolution of the system equations (5.21) or by using a curvefitting technique such as the Rational Fraction Polynomial method[85] applied to measured input-output data. Then a linear curve-fit is performed on equation (5.22) in order to determine the residual and residue coefficients.

If we have two uncertain variables, for instance the longitudinal Young's modulus and shear modulus, then it is referred to as a 2-D Polynomial Chaos model. The order of the model is inferred from the maximum power of ξ. Using equation(5.1), the expanded form for a 2-D Polynomial Chaos model in which ξ_1 and ξ_2 are uncertain parameters, can be written as

$$u_{2nd} = \beta_0 + \beta_1\xi_1 + \beta_2\xi_2 + \beta_3(\xi_1^2 - 1) + \beta_4\xi_1\xi_2 + \beta_5(\xi_2^2 - 1) \tag{5.23}$$

The complex amplitude PCE model can be expressed in terms of real and imaginary parts such that

$$\begin{aligned} u_{2nd} = {} & \beta_{0r} + \beta_{1r}\xi_1 + \beta_{2r}\xi_2 + \beta_{3r}(\xi_1^2 - 1) + \beta_{4r}\xi_1\xi_2 + \beta_{5r}(\xi_2^2 - 1) + \ldots \\ & j\left(\beta_{0i} + \beta_{1i}\xi_1 + \beta_{2i}\xi_2 + \beta_{3i}(\xi_1^2 - 1) + \beta_{4i}\xi_1\xi_2 + \beta_{5i}(\xi_2^2 - 1)\right) \end{aligned} \tag{5.24}$$

This complex PCE model was converted to amplitude and phase by taking the magnitude and angle between the real and imaginary parts. Here β_{ir} are coefficients of the real part of PCE model and β_{ii} are coefficients of the imaginary part of the PCE model.

5.3.2 Determination of PCE-FRF Models

PCE regression models are developed by applying the uncertainty models in section 5.2 to the FRF representation described in section 5.3.1 as follows.

1) Determine a range of test cases based upon Latin Hypercube sampling[83] for the variable parameters (e.g. Young's Modulus)
2) Compute the required FRFs for each test case using the FE model with the prescribed parameters defined in equation (5.20)
3) Curve-fit each FRF in two steps:

   i. Using the eigenvalue solution or the Rational Fraction Polynomial method [84, 85] to determine the frequency and damping of each mode
   ii. Estimate the residues and residuals using the Least Squares Frequency Domain approach[84]

4) Perform a regression analysis [47] to build individual PCE models, as described in section 5.2, based upon the estimated parameters from each FRF (frequencies, dampings, residues and residuals)
5) The PCE representations can be used to efficiently emulate the PDF of each parameter, or directly applied to equation (5.20) for the FRF bounds.

Note that there is no restriction on the resulting distribution. If required, it is feasible to curve-fit the PDFs to determine the type and coefficients of the distribution.

5.3.3 Simple Beam Model Example

As a first example, a simple uniform beam finite element model which accounts for bending only in one plane (and without shear deformation or torsion) is developed to predict the dynamic response of a simple cantilever beam. The beam element is expressed as a cubic polynomial which leads to the well known expressions for the local element mass and stiffness matrices

$$m = \frac{m_L L}{420}\begin{bmatrix} 156 & 22L & 54 & -13L \\ 22L & 4L^2 & 13L & -3L^2 \\ 54 & 13L & 156 & -22L \\ -13L & -3L^2 & -22L & 4L^2 \end{bmatrix}; k = \frac{EI}{L^3}\begin{bmatrix} 12 & 6L & 12 & 6L \\ 6L & 4L^2 & -6L & 2L^2 \\ -12 & -6L & 12 & -6L \\ 6L & 2L^2 & -6L & 4L^2 \end{bmatrix} \quad (5.25)$$

where L is the element length, m_L is mass per unit length and EI is the flexural rigidity. A total of 10 elements were used to assemble the global mass and stiffness matrices, with proportional damping being introduced in the equation of motion in the usual manner such that

$$[C] = \alpha[M] + \beta[K] \quad (5.26)$$

where α and β were taken as 0.2 and 0.0001 respectively.

The deterministic FRF, obtained between two points the simple cantilever FE model, is shown in Figure 5.9 along with a typical curve-fit. Note that the apparent large differences in the phase plot are erroneous and are due to the phase being plotted between $\pm 180^{\circ}$ so that, for example, -181° is plotted as 179°. This type of phase variation often occurs on commercial software and is not due to inaccuracies in the fitting process. A 1-D chaos model with variable Young's modulus of coefficient of variation of 0.05 was used to impart uncertainty into the

model. A total of 15 Latin Hypercube Samples were taken to provide data for the second order regression fit. PDF plots, as predicted by PCE model, for the first three frequencies and damping ratios are shown in Figure 5.10,Figure 5.11,Figure 5.12,Figure 5.13 and Figure 5.14 along with PDFs of the complex residues in terms of magnitude and phase, and also the residuals. To assess the quality of these PDFs, Monte Carlo Simulations were conducted with a total of 10,000 samples to construct equivalent PDFs. Excellent agreement is observed in each of the PDF plots for the various parameters as demonstrated with very similar mean and standard deviation results given in Table 5.11.

Based on these models, a PCE model for the FRF was developed by taking 15 Latin Hypercube samples across the entire frequency range. The FRF-PCE model was then emulated to predict 99% confidence bounds on the FRF, which were compared with 10,000 MCS results as shown in Figure 5.15. An excellent comparison was achieved for the mean values and also the upper and lower bounds.

5.3.4 More Realistic Full Scale Aircraft Composite Wing Example

As a more realistic test, the composite wing finite element model 4 was implemented. A Finite Element Model of this wing was developed using NASTRAN with the FRF analysis performed assuming 2 percent structural damping. A typical FRF between the leading and trailing edge wing tips shown in Figure5.16. Again the curve-fitting procedure gives good results.

A PCE model for FRF by taking 60 Latin Hypercube Samples was developed in which 2-D chaos was introduced via longitudinal Young's modulus and shear modulus of wing's spars, skins and ribs. Coefficient of variation on longitudinal Young's modulus and shear modulus is 0.02 with mean of 140GPa and 5.0GPa respectively. Both variables have a

normal distribution. The individual-PCE models were then emulated producing PDF plots which are shown in Figure 5.17,Figure 5.18,Figure 5.19and Figure 5.20. A Monte Carlo Simulation was conducted with a total of 1000 samples to assess the PDFs predicted using the PCE method and it can be seen that there is a good agreement, although it must be remembered that there are far fewer MCS calculations with this example which have resulted in a more disjointed amplitude behaviour of the MCS PDFs compared to the first example, but in all cases the frequency distribution is similar. Table 5.12 shows the excellent agreement between the mean and standard deviation for all of the individual modal parameters. Finally, when the individual PCE regression models are combined to give the FRF-PCE model, Figure 5.21 shows that the FRF confidence bands have a very good agreement.

5.4 Interval Analysis Approach

In this section, an interval analysis with probabilistic and non-probabilistic approaches is derived and demonstrated by using the same aeroelastic examples as before.

5.4.1 Interval Analysis Approach

When information of the uncertain parameters is imprecise, or the data distributions are not available but only their bounds are known, the interval analysis approach can be a suitable choice to predict the bounds on the response e.g. on the flutter speed. In such scenario, uncertain parameters can be defined in the interval notation as [39, 40]

$$[\underline{up},\overline{up}] = [up_o - \Delta up, up_o + \Delta up] \tag{5.27}$$

where $\underline{up}$, $\overline{up}$, up_o and Δup represents lower bound, upper bound, mean and variation in each uncertain parameter vectors respectively. Variation in each uncertain parameter can be written as

$$\frac{\overline{up}-\underline{up}}{2}=\Delta up \tag{5.28}$$

For example, if up_o=100, $\overline{up}$=101 and $\underline{up}$=99, then Δup=1.

The aeroelastic equations for N-dof are solved by converting them into the classical eigensolution form ($(Q-I\lambda)x_0=0$), in which the system matrix 'Q' is not deterministic but has some bounds as the structural parameters such as the material properties, fibre orientation angle and laminate thickness have bounds defined in equation (5.27). Consequently, the eigenvalue and eigenvectors will also have bounds and can be approximated with their Taylor series expansion[48, 49, 86, 87]. For example, the eigenvalue and root bending moment expressions become for n uncertain terms

$$\mathrm{Re}(\lambda)=\mathrm{Re}(\lambda)|_{up_0}+\sum_{i=1}^{n}\frac{\partial \mathrm{Re}(\lambda)}{\partial up_i}(\delta up_i) \quad and \quad R_{bm}=R_{bm}|_{up_0}+\sum_{i=1}^{n}\frac{\partial R_{bm}}{\partial up_i}(\delta up_i) \tag{5.29}$$

where $\mathrm{Re}(\lambda)|_{up_0}$ and $R_{bm}|_{up_0}$ are the real part of the eignenvalue and the root bending moment at the mean of the uncertain parameter vector containing 'i=1,2,..n' uncertain variables respectively and $\frac{\partial(\mathrm{Re}(\lambda))}{\partial up_i}$ and $\frac{\partial R_{bm}}{\partial up_i}$ are the gradient of the real part of the eigenvalue and the root bending moment due to each uncertain variables respectively evaluated at their mean values.

Key steps and explanation to find the flutter speed bounds are as follows:

1. Perform a deterministic analysis and note the $\mathrm{Re}(\lambda(V))|_{up_0}$ against a number of speeds below and above the deterministic flutter speed. The deterministic flutter speed corresponds to the speed value where $\mathrm{Re}(\lambda(V))|_{up_0} = 0$.

2. Repeat step 1 but with $up_0 + \delta up_i$, where δup_i is a very small value.

3. Work out $\dfrac{\partial(\mathrm{Re}(\lambda(V)))}{\partial up_i} \cong \left(\dfrac{\mathrm{Re}(\lambda(V))|_{up_0+\delta up_i} - \mathrm{Re}(\lambda(V)|_{up_0})}{\delta up_i} \right)$ (5.30)

Such scheme is often called as the forward difference scheme for evaluating the approximate gradient values. Backward or central difference scheme, the Nelson method [88-90]or NASTRAN 200 sensitivity solver can also be utilised instead. NASTRAN 200 sensitivity solver calculates the gradient exactly. Note by doing so, the gradients are found at a number of speeds below and above the deterministic flutter speed. In the present work, NASTRAN solver 200 and the forward difference scheme both are utilised.

4. Examination of $\mathrm{Re}(\lambda) = \mathrm{Re}(\lambda)|_{up_0} + \sum_{i=1}^{n} \dfrac{\partial \mathrm{Re}(\lambda)}{\partial \mathrm{up_i}} (\delta \mathrm{up_i})$ shows that maxima and minima of $\mathrm{Re}(\lambda)$ lies in an interval of $\overline{\mathrm{up_i}} < \mathrm{up_i} < \underline{\mathrm{up_i}}$. This then means that at each speed, the maximum and minimum values of $\mathrm{Re}(\lambda)$ can be obtained by setting up the global optimisation problem

for $\mathrm{Re}(\lambda)$ within $\overline{up_i} < up_i < \underline{up_i}$ and consequently becomes a computationally expensive approach. In the present study, a linear approximation is made by assuming that the maximum and minimum of $\mathrm{Re}(\lambda)$ lies at the maximum and minimum values of up_i. Such an assumption may not likely to produce the exact maximum and minimum of $\mathrm{Re}(\lambda)$ and some discrepancy may be noted compared with the maxima and minima results of $\mathrm{Re}(\lambda)$ obtained from the computationally inefficient global optimisation problem as stated earlier. Applying the interval theory [39, 40, 82] to the real part of the eigenvalue 'λ' and the root bending moment R_{bm} defined in the equation (5.29) as

$$\mathrm{Re}(\lambda)^I = \mathrm{Re}(\lambda)|_{up_0} + \sum_{i=1}^{n}\left|\frac{\partial(\mathrm{Re}(\lambda))}{\partial up_i}\right|\left(\Delta up_i^I\right) \quad and \quad R_{bm}{}^I = R_{bm}|_{up_0} + \sum_{i=1}^{n}\left|\frac{\partial R_{bm}}{\partial up_i}\right|\left(\Delta up_i^I\right) \tag{5.31}$$

where $\left(\Delta up_i^I\right)$ is the interval values of the uncertain parameter 'i'. Maximum and minimum of $\mathrm{Re}(\lambda)$ can be written as

$$\mathrm{Re}_{max}(\lambda) = \mathrm{Re}(\lambda)|_{up_0} + \sum_{i=1}^{n}\left|\frac{\partial(\mathrm{Re}(\lambda))}{\partial up_i}\right|(\Delta up_i) \;;\; \mathrm{Re}_{min}(\lambda) = \mathrm{Re}(\lambda)|_{up_0} - \sum_{i=1}^{n}\left|\frac{\partial(\mathrm{Re}(\lambda))}{\partial up_i}\right|(\Delta up_i) \tag{5.32}$$

It is to mention here that the upper and lower bounds of the real part defined in the equation (5.31) change with speed, whereas the upper and lower bound of the root bending moment defined in the equation (5.31) are constant values defined at particular flight condition. Equating equation (5.31) to zero, gives upper and lower bound of the flutter speed.

It is also possible to extend the non-probabilistic interval analysis approach [49]by adopting probability theory. Uncertain parameters treated earlier in the non-probabilistic way are now assumed to have a Gaussian distribution with 0 mean and σ_{up} being their standard deviation. Applying expected value operations to equation (5.29) leads to

$$E\langle \mathrm{Re}(\lambda)\rangle \cong E\langle \mathrm{Re}(\lambda)|_{up_0}\rangle + E\left\langle \sum_{i=1}^{n} \frac{\partial \lambda}{\partial up_i}(\delta up_i)\right\rangle \Rightarrow E\langle \mathrm{Re}(\lambda)\rangle \cong E\langle \mathrm{Re}(\lambda)|_{up_0}\rangle + E\left\langle \sum_{i=1}^{n} \frac{\partial(\mathrm{Re}(\lambda))}{\partial up_i}\right\rangle E\langle(\delta up_i)\rangle \Rightarrow \quad (5.33)$$

$$E\langle \mathrm{Re}(\lambda)\rangle \cong E\langle \mathrm{Re}(\lambda)|_{up_0}\rangle$$

and

$$E\langle R_{bm}\rangle \cong E\langle R_{bm}|_{up_0}\rangle + E\left\langle \sum_{i=1}^{n} \frac{\partial R_{bm}}{\partial up_i}(\delta up_i)\right\rangle \Rightarrow E\langle R_{bm}\rangle \cong E\langle R_{bm}|_{up_0}\rangle + E\left\langle \sum_{i=1}^{n} \frac{\partial R_{bm}}{\partial up_i}\right\rangle E\langle(\delta up_i)\rangle \Rightarrow$$

$$E\langle R_{bm}\rangle \cong E\langle R_{bm}|_{up_0}\rangle$$

in which $E\langle(\delta up_i)\rangle = 0$. This shows that mean value of the real part of the eigenvalue is same as the deterministic case

The variance of $\mathrm{Re}(\lambda)$ [48, 49] can be written as

$$\mathrm{Var}(\mathrm{Re}(\lambda)) = \sum_{i=1}^{n}\left(\frac{\partial(\mathrm{Re}(\lambda))}{\partial up_i}\right)^2 \mathrm{Var}(up_i) + \sum_{i=1}^{n}\sum_{j=1}^{n} \frac{\partial(\mathrm{Re}(\lambda))}{\partial up_i}\frac{\partial(\mathrm{Re}(\lambda))}{\partial up_j}\mathrm{Cov}(up_i, up_j) \quad (5.34)$$

where $\mathrm{Cov}(up_i, up_j)$ is the covariance matrix of the random variables and for the uncorrelated variables it is zero, and the variance reduces to

$$\mathrm{Var}(\mathrm{Re}(\lambda)) = \sum_{i=1}^{n}\left(\frac{\partial(\mathrm{Re}(\lambda))}{\partial up_i}\right)^2 \mathrm{Var}(up_i) \quad (5.35)$$

Once the mean and variance are calculated from the equations (5.33) and(5.35), the upper and lower bounds of the real part of eigenvalue can be predicted from[49]

$$\begin{aligned} \mathrm{Re}\left(\overline{\lambda}\right) &= E\left\langle \mathrm{Re}(\lambda)\,|_{up_0} \right\rangle + \sqrt{\mathrm{Var}(\mathrm{Re}(\lambda))} \\ \mathrm{Re}\left(\underline{\lambda}\right) &= E\left\langle \mathrm{Re}(\lambda)\,|_{up_0} \right\rangle - \sqrt{\mathrm{Var}(\mathrm{Re}(\lambda))} \end{aligned} \tag{5.36}$$

In a similar way, the upper and lower bounds of the root bending moment are calculated.

Example 1: Flutter speed bounds for the full-scale aircraft composite wing

The more realistic full-scale composite wing model example (used in section 5.2.5) is analysed with the non-probabilistic interval analysis approach. The longitudinal Young's modulus has been treated as an uncertain variable with bound values of [127.4GPa-152.6GPa] and mean value of 140GPa. NASTRAN solver 200 was used to calculate the gradients. After setting equation (5.31)equal to zero, the upper flutter speed (175.023m/sec) and lower flutter speed (163.448m/sec) were found. V-g plot is shown in Figure 5.22. These results are in excellent agreement with PCE and MCS methods (see Table 5.9).

Example 2: Wind tunnel composite wing model with six uncertain variables

In this example, 2nd Order PCE, probabilistic and non-probabilistic Interval approaches are tested for the wind tunnel composite wing model 2 with fibre angles of $((\theta_1 = -20)_2, (\theta_2 = 15)_2, (\theta_3 = -45)_2)_s$ and which has six uncertain variables was considered. In this example, E_1 , G_{12} , total thickness, θ_1, θ_2 and θ_3 are treated as uncertain parameters. The bound on longitudinal Young's modulus was taken as [90.65GPa, 105.35GPa] with a mean of 98 GPa, and the bounds on shear modulus was [5.18GPa, 6.02GPa] with mean of 5.6GPa, the bounds on total

thickness were [1.584mm, 1.632mm] with mean of 1.608mm, the bounds on θ_1 were [-19°,-21°] with mean of -20°, the bounds on θ_2 was [14.25°,15.75°] with mean of 15° and finally the bounds on θ_3 were [-42°,-48°] with mean of -45°. Predicted bounds on flutter speed and root bending moment with probabilistic and non-probabilistic approaches are shown in Figure 5.23. It has been observed that the probabilistic approach predicted tighter bands compared to the non-probabilistic approach. 6-D chaos was introduced into a 2nd Order PCE model to predict PDF with same uncertain parameters (shown in Figure 5.23). 60 LHS samples were taken to predict the β_i coefficients. Bounds are calculated and presented in Table 5.10. Results of the probabilistic Interval Analysis Method are generally in good agreement with the Polynomial Chaos Expansion Method. It has also been observed that non-probabilistic Interval Analysis Method predicted higher bounds compared to either PCE or the probabilistic Interval Methods.

5.5 Conclusions

1. The PCE approach has been explored in the various engineering fields but in the present work is adopted and applied for the first time to analyse the aeroelastic stability and response of various types of the wing models.

2. The developed PCE approach has two versions of models i.e. PCE-regression[47] and PCE-SAM. In PCE-regression, a regression analysis and LHS technique is adopted to predict involved beta coefficients, which were then utilized to produce PDF estimates. In PCE-SAM, the beta coefficients are predicted by performing the statistical averaging method, which was possible due to the orthogonal structure of PCE.

3. In the PCE-regression approach, systems of linear equations are solved to predict the beta coefficients, whereas in the PCE-SAM orthogonal structure of the polynomials are used to predict the beta coefficients by solving each coefficient equation independently to build the PDF.

4. PCE-SAM predicts the Gaussian part of the response and if non-Gaussian part is required, then large number of samples is required. In doing so the essence of computational efficiency is lost, therefore, PCE-SAM is limited to the 1^{st} order terms i.e. Gaussian part of the response only. For the flutter speed bounds of the Goland wing having seven uncertain variables, both PCE-regression and PCE-SAM showed similar results.

5. The PCE approach has been tested on the wind tunnel wing model, the Goland wing and full-scale aircraft FE composite wing model to quantify their aeroelastic stability by including uncertainties; and results predicted by the PCE approach are in excellent agreement with the Monte Carlo simulation results and with much less computational time.

6. The Interval Analysis approach (probabilistic and non-probabilistic) has been derived by using the perturbation and interval theory[39, 40, 48, 49]. The real part of the eigenvalues are approximated with the First order Taylor series expansion, in which gradient of each real part of eigenvalue is calculated with a finite difference scheme and also by performing the sensitivity analysis in NASTRAN. A further approximation is made by assuming that maximum (minimum) of the response variation is at the maximum (minimum) of the uncertain variables.

7. Non-probabilistic Interval Analysis Approach produced higher bounds (when uncertain variables are six) on the flutter speed compared with probabilistic Interval Analysis approach, whereas interestingly the PCE and probabilistic Interval Analysis approaches produced approximately the similar results. The main reason is that both approaches are based on the probability theory.

8. The PCE approach is also applied for the first time to determine a probabilistic FRF model. PCE models are developed for the modal parameters determined from curve-fitting FRFs obtained from a Finite Element model using a Latin Hypercube technique to define the test cases. The individual probabilistic frequency, damping ratio and complex amplitude PCE models are then combined to define the probabilistic FRF-PCE model. This methodology is illustrated on a simple cantilever beam example and with variations in Young's modulus and also an aircraft composite wing FE model in which the longitudinal and shear modulus are allowed to vary. For considered case, the PDF estimates using the PCE approach for the modal parameters, and also the overall FRF scatter bounds, compare well with those obtained from extensive Monte Carlo simulations even though the PCE based model is much more computationally efficient.

	Uncertain Variable	Polynomials	Support
Continuous	Gaussian	Hermite	$-\infty, +\infty$
	Gamma	Laguerre	$0, +\infty$
	Beta	Jacobi	[a,b]
	Uniform	Lagendre	[a,b]
Discrete	Poisson	Charlier	{1, 2 ...}
	Binomial	Krawtchock	{0,1,2...N}
	Negative Binomial	Meixner	{0,1,2...N}
	Hypergeometric	Hahn	{0,1,2...N}

Table 5.1: Types of PDF and their corresponding Polynomials [46]

Samples	β_0		β_1		β_2	
	Reg.	SAM	REG.	SAM	REG	SAM
30	29.596	29.596	0.1983	0.1917	-0.002	**-0.4931**
40	29.596	29.596	0.1982	0.1936	-0.002	**-0.3919**
50	29.596	29.596	0.1987	0.1946	-0.0018	**-0.2862**
120	29.596	29.596	0.1987	0.1970	0.0021	**-0.1227**

Table 5.2: Convergence Study of PCE-Reg. and PCE-SAM $\{\beta_i\}$

	β_0	β_1	β_2	β_3	β_4	Σ
1st Order PCE	29.596	0.1990				0.1990
2ndOrder PCE	29.596	0.1986	-0.0019			0.1986
3rd Order PCE	29.596	0.1989	-0.0013	0.0007		0.1989
4th Order PCE	29.596	0.1986	-0.0017	0.0005	-0.0002	0.1986
MCS	29.596					0.1987

Table 5.3: β_i coefficients by various order of PCE models (for the flutter asspeed) and MCS results

	β_0	β_1	β_2	β_3	β_4	Σ
1st Order PCE	7.2368	-0.0031	--	--	--	0.0031
2nd Order PCE	7.2368	-0.0031	0.00	--	--	0.0031
3rd Order PCE	7.2368	-0.0031	0.00	-0.00	--	0.0031
4th Order PCE	7.2368	-0.0031	0.00	-0.00	0.00	0.0031
MCS	7.2368	--	--	--	--	0.0031

Table 5.4: β_i coefficients by various order of PCE models (for RBM) and MCS results

	Mean Flutter Speed(μ) (m/sec)	Standard Deviation(σ) (m/sec)
2nd Order PCE	169.6664	1.8824
MCS	169.6654	1.8494

Table 5.5: Mean flutter speed and standard deviation of aircraft composite wing by PCE and MCS approaches

Parameter(Dimension)	Upper Value	Lower Value	Mean
Upper Wing skin(ft)	0.017825	0.013175	0.0155
Lower Wing Skin(ft)	0.017825	0.013175	0.0155
Leading Edge Spar(ft)	0.00069	0.00051	0.0006
Trailing Edge Spar(ft)	0.00069	0.00051	0.0006
Leading Edge Spar Caps(ft^2)	0.04784	0.03536	0.0416
Trailing Edge Spar Caps(ft^2)	0.17204	0.12716	0.1496
Centre Spar Cap(ft^2)	0.04784	0.03536	0.0416

Table 5.6: Structural Parameters mean and bounds of the Goland Wing

β Coefficient	1st Order PCE-SAM	1st Order PCE-Regression	2nd Order PCE	3rd Order PCE
β_0	417.7892	417.7892	417.7883	417.7880
β_1	2.9137	2.9218	2.9017	2.9015
β_2	2.8681	2.8761	2.8999	2.9037
β_3	4.0298	4.0410	4.0351	4.0353
β_4	4.3912	4.4035	4.4009	4.4040
β_5	-0.4050	-0.4061	-0.3945	-0.3937
β_6	-2.6996	-2.7072	-2.7238	-2.7231
β_7	-0.5724	-0.5740	-0.5715	-0.5755
β_8			-0.1255	-0.1279
β_9			0.0877	0.0912
β_{10}			0.0351	0.0405
β_{11}			0.0438	0.0442
β_{12}			0.0099	0.0090
β_{13}			-0.0002	0.0025
β_{14}			-0.0001	0.0040
β_{15}			-0.1245	-0.1260
β_{16}			0.0263	0.0311
β_{17}			0.0437	0.0495
β_{18}			0.0093	0.0100
β_{19}			-0.0027	-0.0019
β_{20}			0.0029	-0.0014
β_{21}			-0.0615	-0.0609
β_{22}			-0.0271	-0.0281
β_{23}			-0.0217	-0.0235
β_{24}			0.0068	0.0086
β_{25}			0.0047	0.0048
β_{26}			-0.0497	-0.0502
β_{27}			0.0037	0.0023
β_{28}			-0.0421	-0.0444
β_{29}			-0.0344	-0.0329
β_{30}			0.0007	0.0038
β_{31}			0.0017	-0.0032
β_{32}			0.0006	0.0031
β_{33}			0.0364	0.0360
β_{34}			0.0243	0.0303
β_{35}			0.0034	0.0057

Table 5.7: Beta Coefficients from PCE-Regression and PCE-SAM

β Coefficient	Value	β Coefficient	Value	β Coefficient	Value
β_{36}	0.0041	β_{72}	-0.0010	β_{108}	-0.0018
β_{37}	0.0027	β_{73}	-0.0053	β_{109}	0.0045
β_{38}	-0.0038	β_{74}	-0.0002	β_{110}	0.0009
β_{39}	-0.0024	β_{75}	-0.0027	β_{111}	0.0029
β_{40}	-0.0042	β_{76}	-0.0004	β_{112}	-0.0042
β_{41}	-0.0048	β_{77}	-0.0046	β_{113}	0.0015
β_{42}	0.0057	β_{78}	-0.0036	β_{114}	0.0008
β_{43}	0.0044	β_{79}	-0.0076	β_{115}	0.0035
β_{44}	-0.0002	β_{80}	0.0007	β_{116}	-0.0010
β_{45}	-0.0008	β_{81}	-0.0013	β_{117}	-0.0009
β_{46}	-0.0074	β_{82}	-0.0021	β_{118}	-0.0042
β_{47}	0.0073	β_{83}	-0.0033		
β_{48}	0.0027	β_{84}	-0.0032		
β_{49}	-0.0017	β_{85}	-0.0046		
β_{50}	0.0047	β_{86}	-0.0011		
β_{51}	0.0013	β_{87}	0.0099		
β_{52}	-0.0001	β_{88}	0.0072		
β_{53}	0.0044	β_{89}	0.0021		
β_{54}	0.0013	β_{90}	0.0004		
β_{55}	0.0035	β_{91}	0.0017		
β_{56}	-0.0045	β_{92}	0.0042		
β_{57}	0.0018	β_{93}	0.0055		
β_{58}	0.0063	β_{94}	0.0003		
β_{59}	0.0017	β_{95}	0.0037		
β_{60}	0.0022	β_{96}	-0.0019		
β_{61}	-0.0016	β_{97}	-0.0004		
β_{62}	0.0002	β_{98}	0.0041		
β_{63}	0.0013	β_{99}	-0.0035		
β_{64}	-0.0026	β_{100}	-0.0003		
β_{65}	-0.0022	β_{101}	0.0030		
β_{66}	0.0017	β_{102}	0.0007		
β_{67}	-0.0037	β_{103}	-0.0057		
β_{68}	0.0002	β_{104}	-0.0002		
β_{69}	-0.0022	β_{105}	0.0003		
β_{70}	0.0030	β_{106}	-0.0036		
β_{71}	0.0034	β_{107}	-0.0013		

Table 5.8: Remaining beta coefficients for 3rd Order PCE

	Mean (μ) (m/sec)	Minimum (m/sec)	Maximum (m/sec)	Standard Deviation(σ) (m/sec)
PCE	169.666	163.926	175.276	1.882
MCS	169.665	164.414	175.157	1.849
Interval Analysis	169.688	163.448	175.023	-

Table 5.9: Mean, minimum, maximum and standard deviation of flutter speed by various approaches

		Interval Model (Probabilistic)	Interval Model (Non -Probabilistic)	PCE Model
Example2	Upper Bound (m/sec)	28.1280	29.1840	28.1056
	Lower Bound (m/sec)	26.1370	25.3560	25.9318
	Standard Deviation	0.356	-	0.3623
	Total Bound (m/sec)	1.991	3.828	2.1738

a) Bounds on Flutter Speed by various Approaches

		Interval Model (Probabilistic)	Interval Model (Non -Probabilistic.)	PCE Model
Example2	Upper Bound (N.m)	7.2335	7.2429	7.2327
	Lower Bound (N.m)	7.2089	7.1996	7.2075
	Standard Deviation	0.0041	-	0.0042
	Total Bound (N.m)	0.0246	0.0433	0.0252

b) Bounds on Root Bending Moment by various Approaches

Table 5.10: Bounds on flutter speed and Root bending moment by various Approaches

Method	Mode 1				Mode 2				Mode 3			
	Frequency(Hz)		**Damping**		**Frequency(Hz)**		**Damping**		**Frequency(Hz)**		**Damping**	
	M	σ	μ	σ	μ	σ	μ	σ	μ	σ	μ	σ
PCE	2.0931	0.0524	0.0083	1.744e-4	13.1180	0.3283	0.0053	7.271e-5	36.7388	0.9195	0.0120	2.780e-4
MCS	2.0931	0.0524	0.0083	1.748e-4	13.1179	0.3284	0.0053	7.269e-5	36.7387	0.9198	0.0120	2.781e-4
	Amplitude		**Phase**		**Amplitude**		**Phase**		**Amplitude**		**Phase**	
PCE	8.89e-5	5.863e-6	-0.0543	0.0077	1.032e-4	2.636e-6	-0.0314	0.0027	0.0016	1.456e-6	6.589e-4	1.461e-4
MCS	8.89e-5	5.991e-6	-0.0543	0.0077	1.032e-4	2.646e-6	-0.0314	0.0027	0.0016	1.462e-6	6.587e-4	1.454e-4
	Mass Residual		**Stiffness Residual**									
PCE	7.68e-9	5.688e-10	-8.897e-8	2.518e-8								
MCS	7.68e-9	5.720e-10	-8.912e-8	2.592e-8								

Table 5.11: Beam Model Statistics of Parameters using PCE and Monte Carlo methods

Method	Mode 1				Mode 2				Mode 3			
	Frequency(Hz)		**Damping**		**Frequency(Hz)**		**Damping**		**Frequency(Hz)**		**Damping**	
	M	σ	μ	σ	μ	σ	μ	σ	μ	σ	μ	σ
PCE	2.6043	0.0177	0.0100	2.5214e-6	12.6898	0.0874	0.0100	3.948e-6	31.8241	0.2195	0.0100	6.5887e-7
MCS	2.6043	0.0177	0.0100	2.5942e-6	12.6898	0.0878	0.0100	3.961e-6	31.8241	0.2204	0.0100	6.6126e-7
	Amplitude		**Phase**		**Amplitude**		**Phase**		**Amplitude**		**Phase**	
PCE	0.2783	0.0018	0.0071	0.0011	0.3055	0.0018	0.0064	9.221e-4	0.3007	5.5852e-4	0.0029	4.5186e-4
MCS	0.2783	0.0018	0.0071	0.0011	0.3055	0.0018	0.0064	9.263e-4	0.3007	5.6051e-4	0.0029	4.5381e-4
	Mass Residual		**Stiffness Residual**									
PCE	-2.76e-6	2.1453e-7	3.6785e-5	4.7319e-6								
MCS	-2.76e-6	2.1553e-7	3.6785e-5	4.7427e-6								

Table 5.12: Composite Wing Model Statistics of Parameters using PCE and Monte Carlo methods

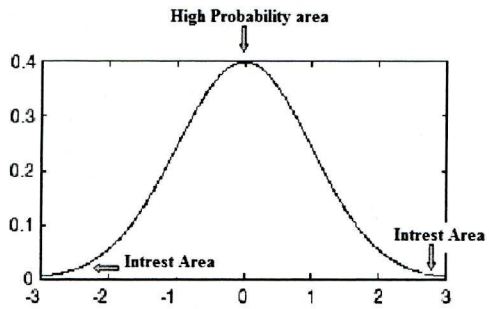

Figure 5.1: PDF interest areas

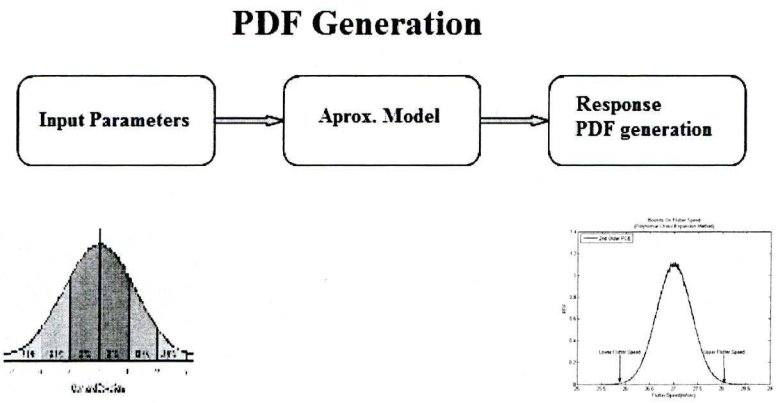

Figure 5.2: Efficient PDF Generation Process

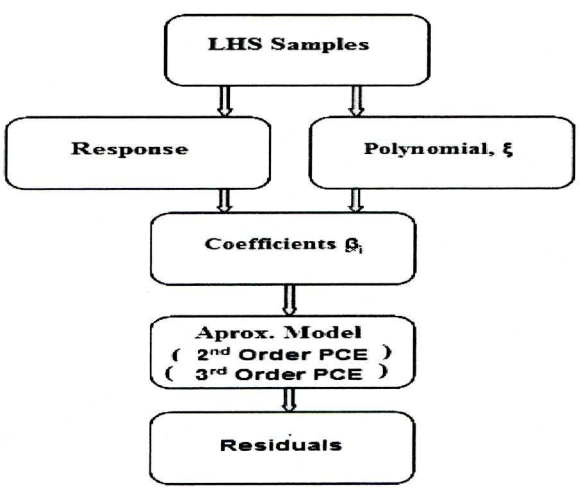

Figure 5.3: Flow Diagram of Regression Analysis

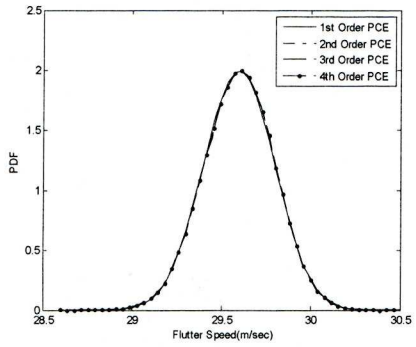

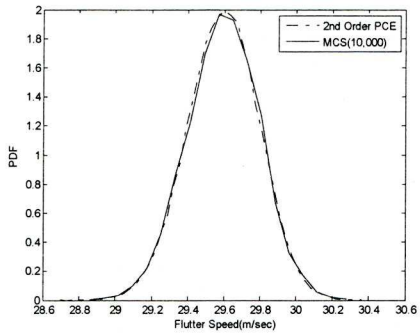

a) 1^{st},2^{nd} ,3^{rd} and 4^{th} Order PCE-Regression Models

b) Order PCE-Regression and MCS (10,000)

Figure 5.4: PDF predicted by various models

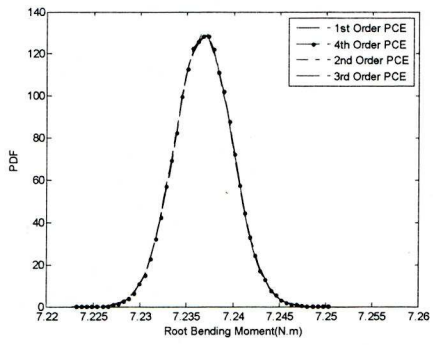

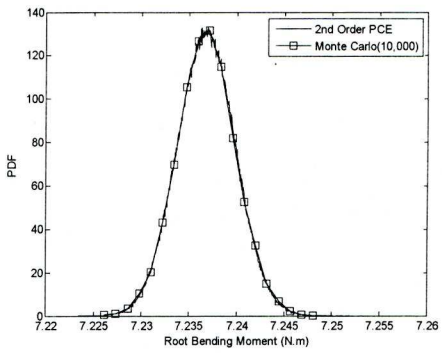

a) 1^{st},2^{nd} ,3^{rd} and 4^{th} Order PCE-Regression Models

b) MCS and 2^{nd} Order PCE-Reg

Figure 5.5: PDF by various orders of PCE and MCS

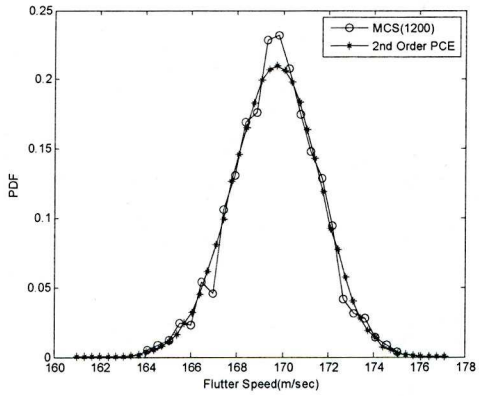

Figure 5.6: PDF of Full Scale aircraft FE Model (E_1 uncertain)

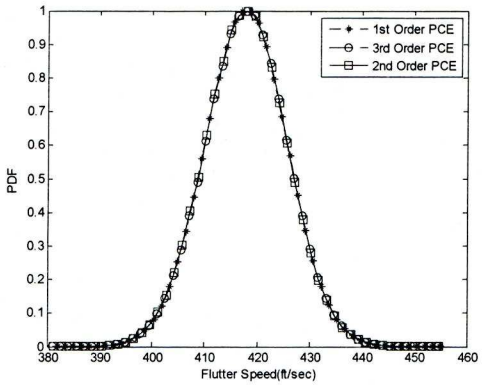

Figure 5.7: 1st, 2nd and 3rd Order PCE-Regression model for the Goland Wing(360 LHS)

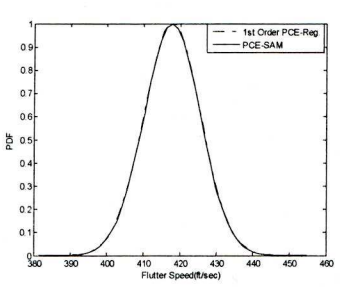

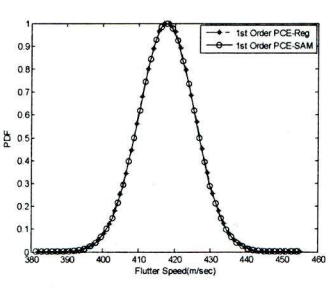

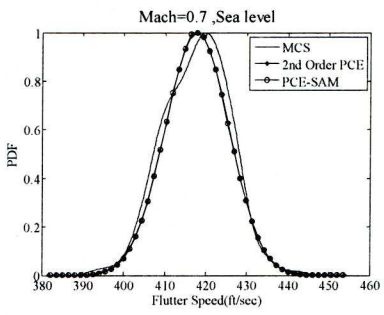

a) PCE-Regression & PCE-SAM PDF(120 LHS)

b) PCE-Regression & PCE-SAM(360 LHS)

c) PCE-Regression, PCE-SAM & MCS Approaches

Figure 5.8: Normalised PDF predicted by various approaches

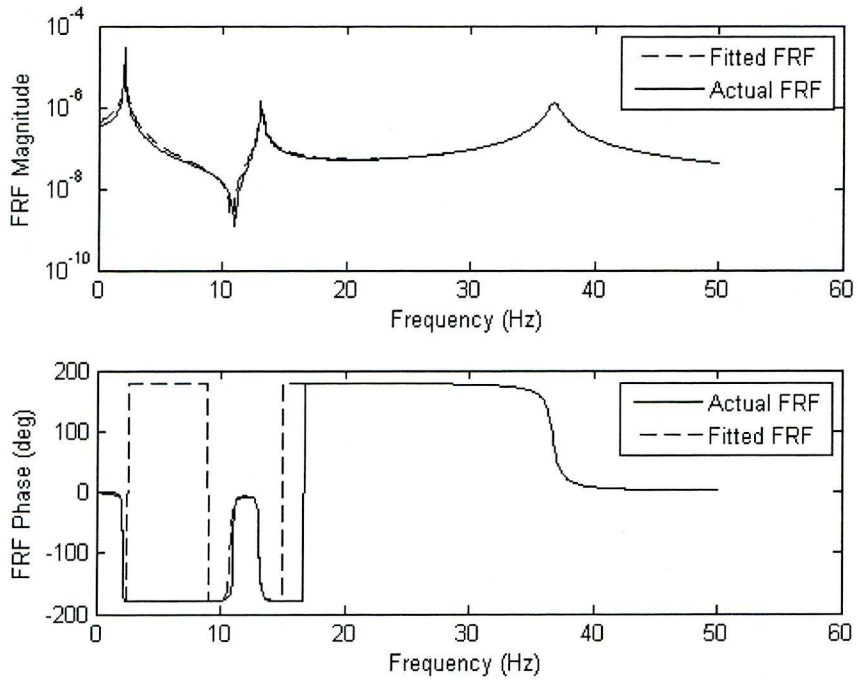

Figure 5.9: Beam Model. Typical Fitted and Actual FRF plots

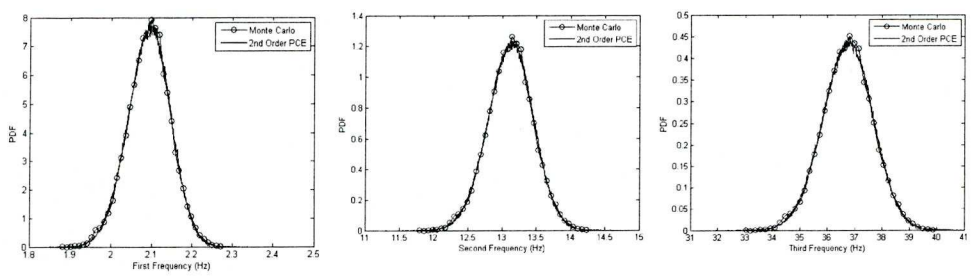

Figure 5.10: Beam Model. PDF Distributions for Frequencies for first three modes using PCE and MCS

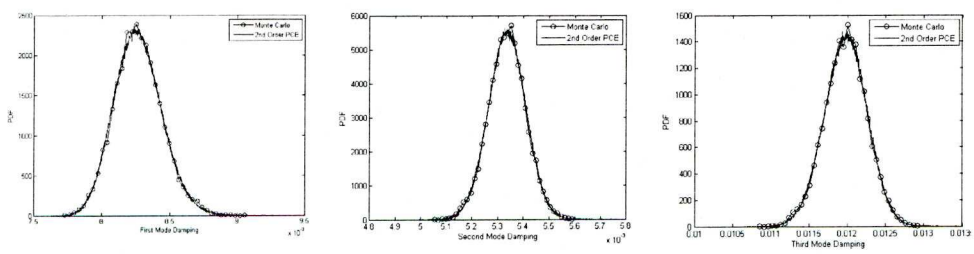

Figure 5.11: Beam Model. PDF Distributions for Damping Ratios for first three modes using PCE and MCS

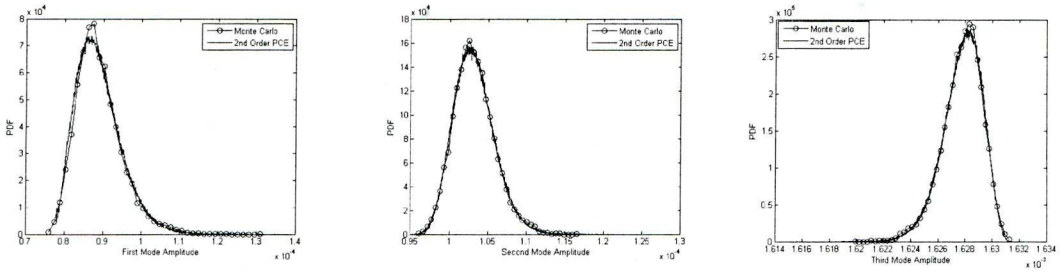

Figure 5.12: Beam Model. PDF Distributions for Residue Amplitude for first three modes using PCE and MCS

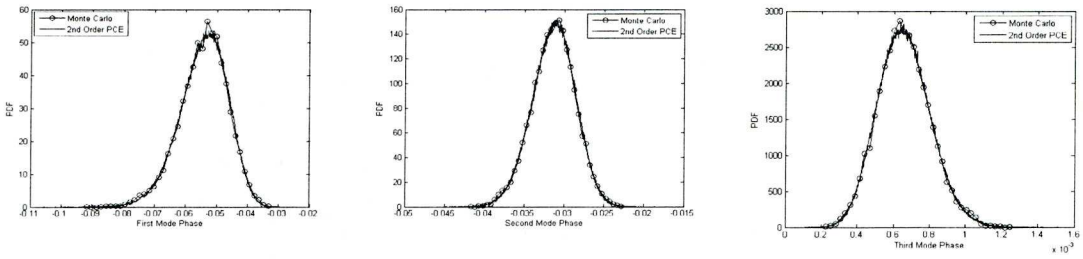

Figure 5.13: Beam Model. PDF Distributions for Residue Phase for first three modes using PCE and MCS

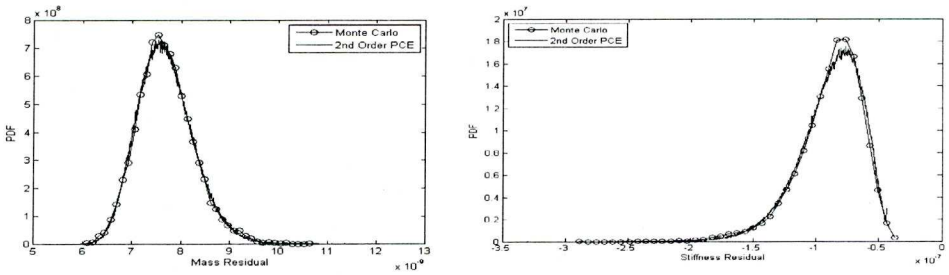

Figure 5.14: Beam Model. PDF Distributions for Mass and Stiffness Residual Distributions for first three modes using PCE and MCS

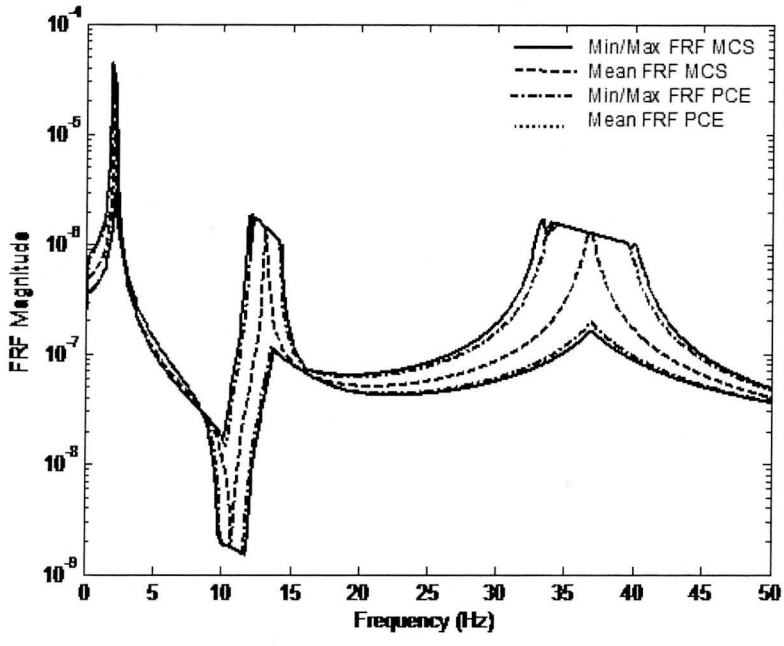

Figure 5.15: Beam Model. FRF 99% Confidence Bounds by PCE and MCS approaches

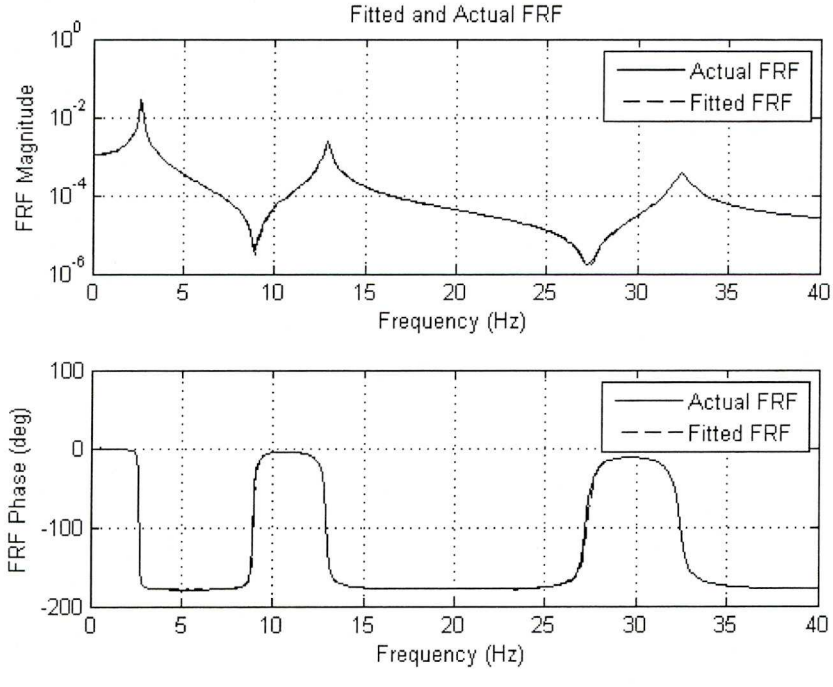

Figure5.16: Composite Wing Model. Typical Model and Fitted FRF Plots

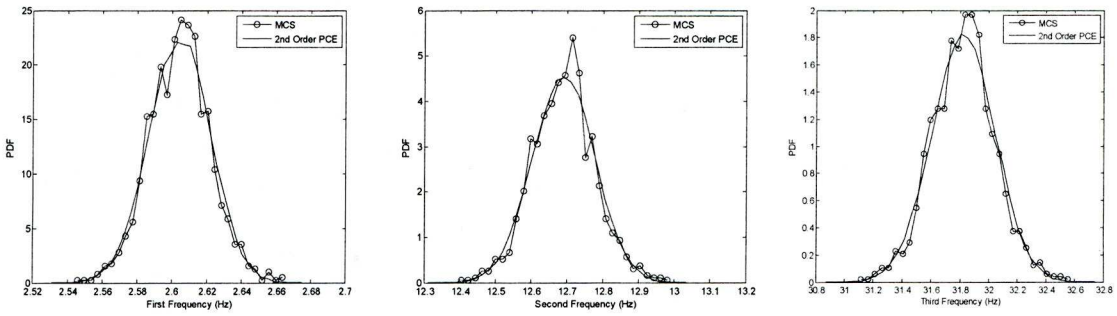

Figure 5.17: Composite Wing Model. PDF Distributions for Frequencies for first three modes using PCE and MCS

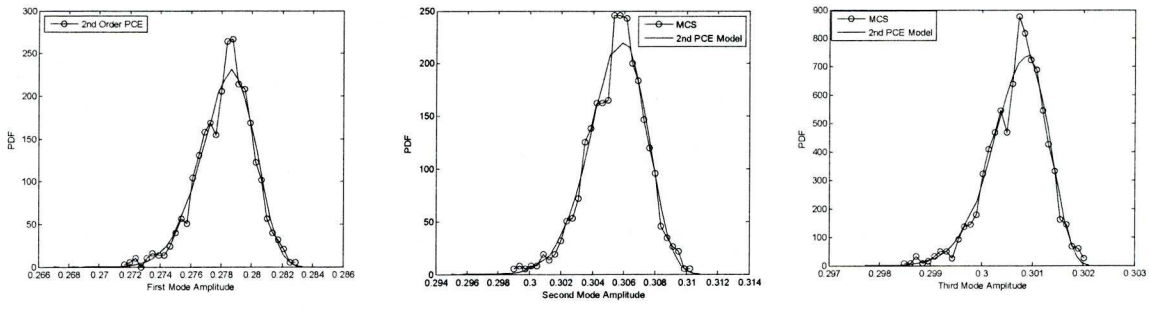

Figure 5.18: Aircraft Wing Model. PDF Distributions for Residue Amplitude for first three modes using PCE and MCS

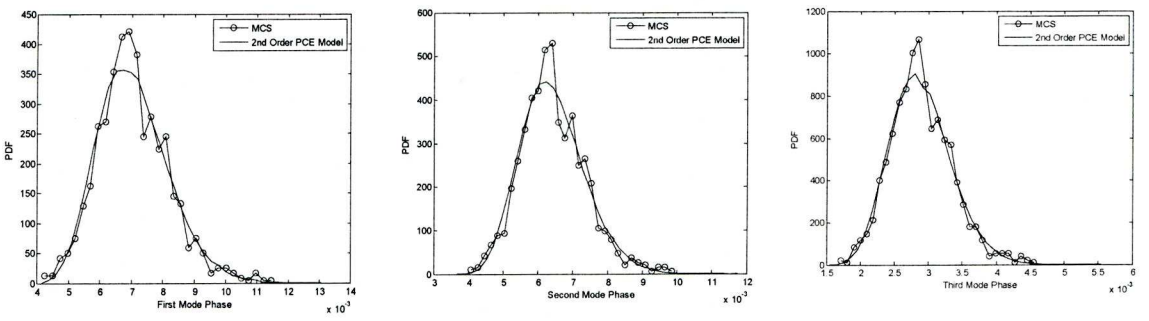

Figure 5.19: Composite Wing Model. PDF Distributions of Phase of Residues for First 3 Modes using PCE and MCS

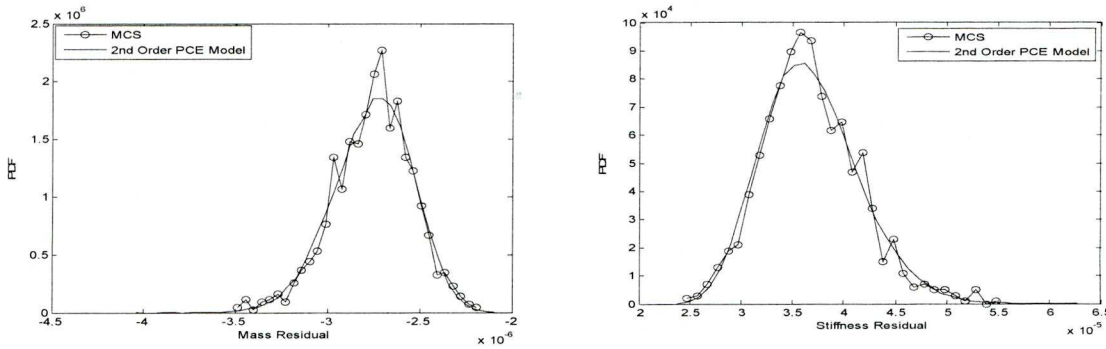

Figure 5.20: Composite Wing Model. PDF Distributions of Mass and Stiffness of Residual for First 3 Modes using PCE and MCS

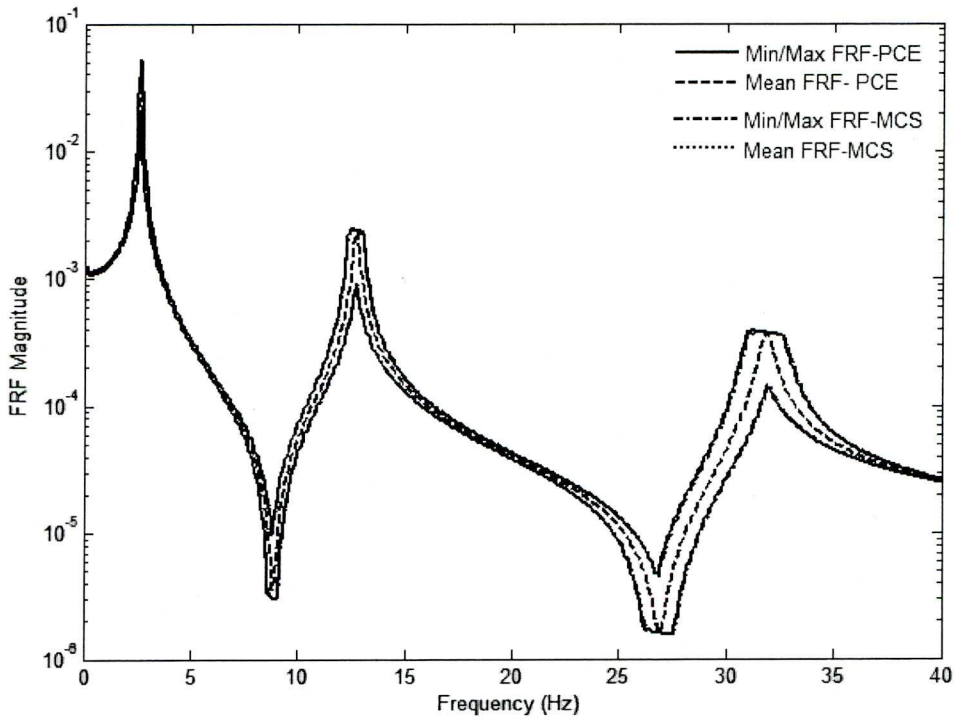

Figure 5.21: Composite Wing Model. 99% FRF Confidence Bands FRF Plot by PCE and MCS approaches (E and G Uncertain parameters)

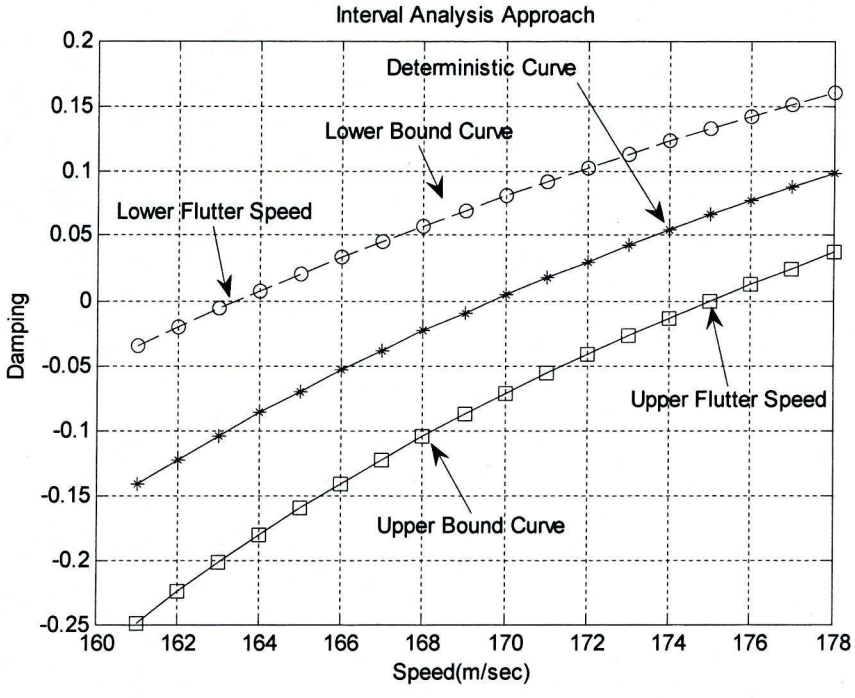

Figure 5.22: Interval Analysis Approach

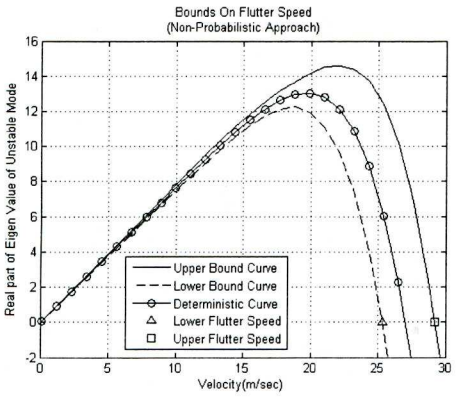

a) Bounds on v-g curves – Method Interval Analysis (Non-Probabilistic Approach)

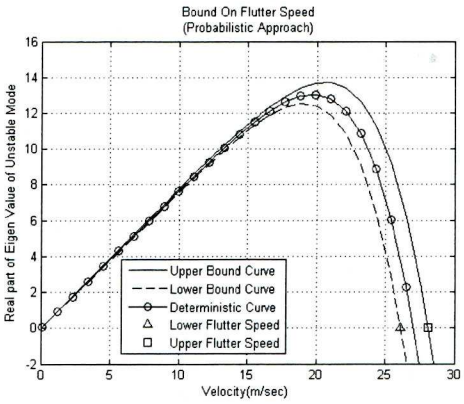

b) Bounds on v-g curves – Method Interval Analysis(Probabilistic Approach)

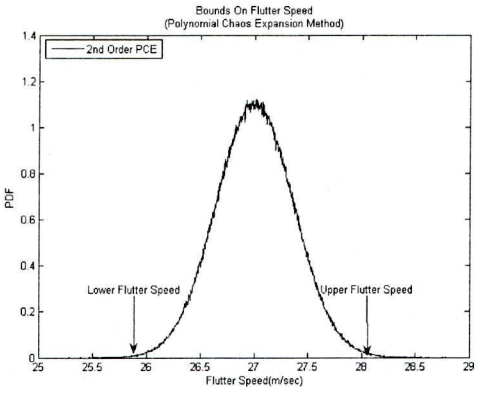

c) PDF plot for Flutter Speed- PCE Model

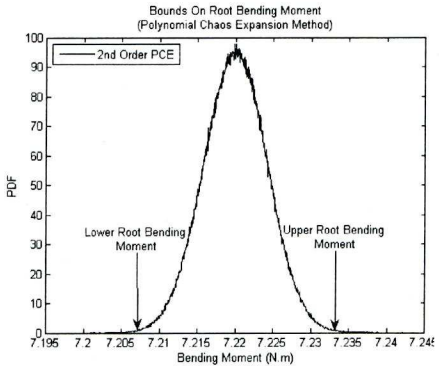

d) PDF plot of RBM-PCE Model

Figure 5.23: Flutter speed and RBM bounds by PCE and Interval analysis approaches

Chapter 6

Robustness of Composite Wing Aeroelastic Design

6.1 Introduction

A design, which minimises the performance variation without eliminating the uncertainty, is a robust design[59] and is often insensitive to the small changes. Robust design approaches seek to minimize the variation in the system performance about the mean design point[60].

In this chapter, two approaches for robust design are presented; first when PDF of response is available (for example from the PCE approach) and in second case when only upper and lower bounds are known (for example from non-probabilistic interval analysis approach).

6.2 Robust Design Criteria

6.2.1 Robust Design concept for PCE Approach

The efficient PCE approach to PDF generation in Chapter 5 can be used for the robust design optimisation. Here, the concept of robustness is used as a measure of safety of the structure in terms of the probability of survival, i.e. some defined flutter speed or maximum root bending moment not being exceeded.

Consider the deterministic optimum design, a design that is obtained either by maximising the flutter speed or minimising the root bending moment or both. Such designs when incorporated with uncertainty (for example, the longitudinal Young's modulus) will then produce the PDF.

Now consider the typical PDF plots for both flutter speed and maximum root bending moment obtained by applying the PCE method to an optimised deterministic design, as shown in Figure 6.1. For some required design flutter speed V_D, the area to the left of this line contains all the uncertain cases that give flutter. Similarly, for some required design root bending moment R_D, the area to the right of this line contains all the uncertain cases that give root-bending moment.

For a robust optimization, we need to find the design that gives the largest area of PDF *above* the design flutter speed. The same approach holds for gust response, except now we require maximising the area of the PDF that lies *below* some pre-defined design root bending moment. A robust optimum design is not necessarily the one with the best flutter speed, but the one with the largest PDF area to the right of the design flutter speed or the largest PDF area to the left of the design root bending moment. The "robust design" PDF is better than the "non-robust design" PDF even though a significant proportion of the "non-robust design" PDF lies above it.

6.2.2 Robust Design concept for Interval Analysis Approach

The predicted bounds obtained using the interval analysis approach can be utilised to explore the robust optimum design. Consider the typical upper and lower bounds plots obtained by applying the Interval Analysis Method to an optimised deterministic design, as shown in Figure 6.2, in which A and B points on these curves represent the lower and upper flutter speed (in Figure 6.2). Here measure of failure for the flutter speed can be assumed as

$$MOF_{flutter} = \frac{V_D - V_A}{V_B - V_A} \qquad V_A < V_D < V_B$$
$$= 1 \qquad V_B < V_D \qquad (6.1)$$
$$= 0 \qquad V_A > V_D$$

in which V_D ,V_A and V_B corresponds to some design, lower and upper flutter speed respectively.

Similarly, the measure of failure for the root bending moment can be written as

$$MOF_{gust} = \frac{R_B - R_D}{R_B - R_A} \qquad R_A < R_D > R_B$$
$$= 1 \qquad R_D > R_A \qquad (6.2)$$
$$= 0 \qquad R_B > R_D$$

in which R_D ,R_A and R_B corresponds to some design, lower and upper root bending moment respectively.

6.3 Robust Design of the Composite Plate Wing Model using PCE

In this section, the robust design of the composite wing plate model using the PCE approach is demonstrated on the following two cases:

1. Flutter/Divergence only
2. Flutter and gust response

In each case both Deterministic and Robust designs are compared.

6.3.1 Optimal Deterministic Design for Flutter/Divergence

A composite wing model 1 composed of six layers with lay-up configuration of $(\theta_1/\theta_2/\theta_3)_s$ was considered as the case to illustrate how

the PDFs generated from the PCE approach can be used for robust optimisation. The longitudinal Young's modulus (E_1), in-plane shear modulus (G_{12}) and total thickness of laminate were all treated as uncertain parameters. The coefficient of variation for the moduli was 0.1 and that for the thickness was set as 0.02.

Initially, the wing lay-up orientation was optimised using PSO assuming there was no uncertainty in the parameters, giving the deterministic maximum flutter speed of 32.9 m/s, as shown in Table 6.1. The optimum orientations were found to be $[-34.16/48.5/21.0]_s$. For every application of PSO, eight particles in the swarm were selected. A 2nd order probabilistic flutter model was then derived based upon these orientations using thirty different test samples. PDF plots were then generated from this flutter model by taking 100000 emulations. Comparison with MCS (3375 simulations) is shown in Figure 6.3 and once again there is good agreement. The MCS results were performed to confirm the finding that there is a noticeable skewness to the PDF, and Table 6.1 shows that the mean of the probabilistic model is almost 2 m/s less than the deterministic optimum.

6.3.2 Robust Optimisation including Uncertainty for Flutter/Divergence

A robust optimisation was then performed for design flutter speeds of 28 and 32m/s. For each selected lay-up orientation, a PCE probabilistic flutter model was generated using the above procedure, and then the PDF calculated using 100000 emulations. The area of the PDF less than the design flutter speed was then minimised. Figure 6.4 shows a typical convergence of the optimisation process, it can be seen that on the initial runs, the entire PDF distribution is less (i.e. flutter occurs) than the design flutter speed, however, after 10 iterations virtually all of the

PDF distribution is above (flutter free) the design flutter speed. Figure 6.3 shows the optimum robust design PDF for the 32 m/s case (for which orientations were found to be $[-33.62/47.82/\ 67.9]_s$ and gave flutter speed of 32.242 m/s without uncertainties in the parameters)and it can be clearly seen how most of the area is above that of the deterministic optimum PDF even though the mean value is less. For the the design case considered, the robust design approach has roughly a 50% reduction in flutter cases compared to (see Table 6.2) the deterministic optimum design.

6.3.3 Optimal Deterministic Design for Flutter/Divergence and Gust Alleviation

The fibre placement requirement in the composite structures to increase the flutter/divergence speed conflicts that used to attain maximum gust alleviation (increased downwash). Consequently, if the wing is optimised considering just one of these parameters, it is likely that the performance of the other will be poor. Consider a multi-objective cost function Ω_{det} that combines both requirements such that

$$\Omega_{det} = \min(w_f * \frac{V_d}{V_{max}} + w_g * \frac{R_{min}}{R_d}) \qquad (6.3)$$

in which w_f , w_g are weight factors whose sum equals unity, V_d and V_{max} are the design and maximum flutter/divergence speed, and R_d and R_{min} are the design and minimum root bending moment. Setting either of the weight factors to unity gives the cases where one of the objective functions is inactive, and by setting the weightings for various values between 0 and 1 leads to the determination of the Pareto Frontier[80] that defines the best multi-objective flutter speed and root bending

moment solution for different weight factors. These different weightings allow different emphasis to be made on the optimisation.

The baseline wind tunnel rectangular composite wing model 2 of 10 layers with three orientation variables i.e. $\left(\theta_1/(\theta_2)_2/(\theta_3)_2\right)_s$ is considered (for the material properties see Table 6.3). The longitudinal Young's modulus (E_1) was treated as the uncertain parameter with a coefficient of variation of 0.05.

PSO was employed to the PCE-Model one with 20 particles in each loop and a maximum total of 50 iterations conducted, in order to optimise the lay-up for each set of weighting values. Maximum flutter speeds and bending moments for different weighting values are given in Table 6.4 and the points making up the Pareto Optimal Curve are shown in Figure 6.5. As might be expected, the maximum instability speed is obtained when the gust constraint is inactive, and the minimum root bending moment obtained when the flutter constraint is inactive. Note that the instability speed drops significantly when only the gust response is considered, in this case a divergence instability is found. The ideal case would be when flutter speed is 25.07 m/sec (which is flutter only case) and RBM is 7.157 N.m (which is the Gust only case). Here an average principle is applied which means that sum of ratio of the flutter speed to the maximum flutter speed and the minimum RBM value to the RBM value should be close to 2(2 value is the ideal case). Such ideal Pareto point is named as "Utopia point" in the literature[60]. Based on this criterion, the $w_f = 0.1$ $w_g = 0.9$ case can be taken as the optimum deterministic lay-up configuration.

Furthermore, it is interesting to note in Table 6.5 that the flutter speed is 23.827 m/sec for w_f =0.9, 0.8, 0.7 and 0.6 even though these points

correspond to a large spread of orientations θ_1 , θ_2 and θ_3. For all these w_f values, similar ratios of torsional stiffness (D_{66}) to bending stiffness (D_{11}) ~0.33, and bend-torsional stiffness (D_{16}) to bending stiffness (D_{11}) ~ -0.4, can be seen leading to the same flutter speed.

6.3.4 Robust Optimisation including Uncertainty– Generation of Robust Pareto Curves

The PCE-model one was considered as the case to illustrate how the PDFs generated from the PCE approach can be used for robust optimisation. The cost function was taken as

$$\Omega_{robust}=\min(w_f*\alpha+w_g*\beta) \tag{6.4}$$

in which w_f , w_g are again weight factors whose sum must be one, α is the probability of failure for flutter/divergence against given some given design speed and β is the probability of failure for the root bending moment against some given design root bending moment, using the criteria defined in Figure 6.1. A robust optimisation was then performed in which the area of the PDF smaller than the design flutter speed, and the area of the PDF greater than the root bending moment, were minimised. 15 samples for E_1 were taken to define the PCE model for each set of orientations and then the PDFs for flutter speed and gust response calculated using 100000 emulations. 10 particles were used for each iteration of the PSO optimization and 50 iterations in total were taken. This process was then repeated for different w_f and w_g combinations for design flutter speeds and root bending moments of (25m/s, 7.255Nm – Example 1a) and (24.4m/s, 7.25Nm – example 1b).

Figure 6.6 and Figure 6.7 shows the PDFs obtained for the optimised deterministic and robust designs (best Pareto point) for these two severe

design cases. Note how the robust optimum PDFs have a skewed distribution that is beneficial for meeting the defined cost function. The probability of failure due to flutter/divergence and gusts are shown in Table 6.6and Table 6.7. Table 6.6 and Table 6.7 show how the probability of failure due to flutter (example 1a) lowered from 68 % to 47.5 % and probability of failure due to gust root bending moment from 29% to 2.6 %. Similarly, Table 6.7 shows how the probability of failure due to flutter (example 1b) lowered from 29 % to 19 % and probability of failure due to gust root bending moment from 81% to 3 %. The Robust Pareto points for both design cases shown in Figure 6.8 show the best Pareto points, here defined as the sum of the two failure probabilities.

6.4 Robust Design of the Composite Plate Wing Model using Interval Analysis

In this section, the robust design of the composite wing plate model using the Interval Analysis approach is demonstrated on the following two cases:

1. Flutter/Divergence only
2. Flutter and gust response

A baseline composite wing 2 of 12 layers with three theta variables i.e. $\left((\theta_1)_2/(\theta_2)_2/(\theta_3)_2\right)_s$ is considered for both the said cases. The longitudinal Young's modulus (E_1) was treated as uncertain parameter and for flutter only case it has bound of [92.12-103.88 GPa] whereas for flutter and gust case it has bound of [93.3-102.7 GPa].

6.4.1 Optimal Deterministic and Robust Design for Flutter/Divergence

Initially, the wing lay-up orientation was optimised using PSO assuming there was no uncertainty in the parameters, giving the deterministic maximum flutter speed of 34.893 m/s as shown in Table 6.9 (in this table an optimum design(flutter only case) is one when the gust constraint was inactive). The optimum orientations were found to be $[(-20.4084)_2/(39.002)_2/(33.3321)_2]_s$. For every application of PSO, 20 particles in the swarm were selected.

A robust optimisation was then performed, for the design flutter speed of 34 m/s, by including uncertainty in longitudinal Young's modulus. For each selected lay-up orientation in PSO, minimum and maximum flutter speeds were calculated and then utilized in the equation(6.1) to predict the possibility of failure. The robust orientations were found to be $[(-20.200)_2/(39.6245)_2/(43.642)_2]_s$.

The measure of failure for the robust optimum design is 1.5% whereas for the deterministic optimum design 65% (quite large value compared with deterministic design). Plots of the real part of eigenvalue against speed for the deterministic and robust designs are shown in Figure 6.9 and Figure 6.10 respectively. Note the deterministic optimum design, due to uncertainty in Young's modulus, showed mode switching phenomenon.

The determinstic optimum design has higher deterministic flutter speed (34.893 m/sec) compared with the robust optimum design (34.585 m/sec). It means that robust design is not necessarily the one, which has higher deterministic flutter speed but is the one, which is least sensitive to uncertainties.

Note at lower speed, the uncertainty has no effect on the upper and lower curves of the real part of eigenvalues and this effect become prominent at higher speed.

6.4.2 Deterministic Optimal Design- Generation of Pareto Frontier Optimal Curve

As mentioned in the section 6.3.3, if the wing is optimised just one of the parameter (flutter), it is likely that performance of the other (gust alleviation) will be poor. For such categories of the optimisation problems, a multi-objective cost function Ω_{det} that combines both requirements can be defined as

$$\Omega_{det} = \min(wf * \frac{V_d}{V_{max}} + wg * \frac{R_{min}}{R_d}) \tag{6.5}$$

in which w_f , w_g are weight factors, the sum of both must be one, V_d and V_{max} are design and maximum flutter/divergence speed and R_d and R_{min} are design and minimum root bending moment.

PSO is employed with 20 particles in each loop and a maximum total of 50 simulations conducted, in order to optimise the lay-up for each set of weighting values. Maximum flutter speeds and bending moments for different weighting values are given in Table 6.9 and points making up the Pareto Optimal Curve are shown in Figure 6.11. As might be expected, the maximum instability speed is obtained when the gust constraint is inactive, and the minimum root bending moment obtained when the flutter constraint is inactive. Note that the instability speed drops significantly when only the gust response is considered, in this case a divergence instability is found.

The ideal case for the deterministic optimum design would be when the flutter speed is 34.893 m/sec (which is flutter only case) and the RBM is 7.0202 N.m (which is the Gust only case). Such ideal Pareto point is named as "Utopia point" in the literature[60]. Here following averaging principle is applied to obtain the Pareto optimal point

$$\frac{V_f}{V_{f\max}} + \frac{RBM_{\min}}{RBM} \to 2 \tag{6.6}$$

where V_f and $V_{f\max}$ is flutter speed and the maximum flutter speed and RBM and $RBM_{\min}$ is root bending moment and the minimum root bending moment for the entire weightings values between 0 and 1 at the particular design constraints. Ideally, the right hand side of the expression (6.6) should be equal to 2. Following the above rule, w_f=1.0, 0.7 and 0.2 have same values upto three decimal places (1.973) and any one from these three points can be taken as a Pareto optimal point. In the present study, w_f=0.2 is assumed as an optimal Pareto point.

6.4.3 Robust Optimisation including Uncertainty– Generation of Robust Pareto Curves

The cost function employed is as follows

$$\Omega_{\text{robust}} = \min(\text{wf} * \text{POF}_{\text{flutter}} + \text{wg} * \text{POF}_{\text{gust}}) \tag{6.7}$$

in which w_f , w_g are weight factors, the sum of both must be one, $\text{POF}_{\text{flutter}}$ is probability of failure for flutter/divergence against given design speed and POF_{gust} is probability of failure for root bending moment against given design root bending moment. A robust optimisation was then performed, with a total of 50 iterations (and in each iteration 20 particles were taken), by varying w_f and w_g for the

design speed of 34m/sec and the root bending moment of 7.20N.m. For each selected lay-up orientation, upper and lower bounds for all modes and then measure of failure were computed and are given in Table 6.10.

The Robust Pareto points are shown in Figure 6.12 show the best Pareto points, here defined as the sum of the two measure of failure.

Similarly, Table 6.11 shows how the measure of failure due to flutter lowered from 67 % to 24 % and measure of failure due to gust root bending moment from 85% to 19 %.

Further analysis of the deterministic optimum design shows its sensitivity towards the uncertainties of the longitudinal Young's modulus. Note the occurrence of the mode-switching phenomenon in the Figure 6.13.

Similarly, the design with w_f=0.7 and w_g=0.3 is also checked and the mode switching phenomenon is noticed and hence, making it sensitive to the uncertainty of the Longitudinal Young's modulus (see Figure 6.14).

The plot of real part of eigenvalue for the robust design is shown in Figure 6.15, and no mode switching is noticed. The deterministic flutter speed of the robust optimum is 34.255 m/sec, which is lower than the deterministic speed of the deterministic optimum design (34.849 m/sec). It shows that the robust design is not necessarily the one, which has larger flutter speed compared with the deterministic optimum design, but must be the design, which is least sensitive to the uncertainty.

Such an approach could arguably be employed for aircraft certification and not just for composite designs. Currently, a design flutter boundary

is specified which must be demonstrated by flight test, however, a flutter free safety margin (typically 15%) must also be validated using extrapolation of flight test results [91] and the worst case bending moments obtained from a range of different gust cases. For a probabilistic approach, the PDFs due to uncertainties (including flight condition) would need to be shown to be above the design flutter speed rather than simply defining a safety margin, and a similar approach taken for the gust response. Airworthiness is still a long way from considering such an approach, however, with increasingly efficient structural designs, the influence of uncertainties on flutter boundaries will have to be taken into account some time in the future.

6.5 Conclusions

1. The PCE and Interval Analysis (IA) approaches are applied sucessfully to predict the robust optimum designs for the single and multi-objective aeroelastic design problems.

2. The robustness of the composite wing model in terms of the flutter speed and root bending moment was considered, and a robust design approach incorporating uncertainties was proposed making use of the efficient PDF generation process. It was shown that a better probabilistic design can be achieved compared to simply taking the best deterministic design solution.

3. The upper and lower bounds obtained from the IA approach are utilized for the robust optimum design prediction. It has been shown that the robust design is not necessarily the one which has higher flutter speed compared with the deterministic optimum design, but must be the design, which is least sensitive to the uncertainty.

4. At the lower speed values, the upper and lower bound curves of real part of eigenvalues are minimally affected by uncertainty. Such affects may become profound closer to flutter as noted in the present studied examples.

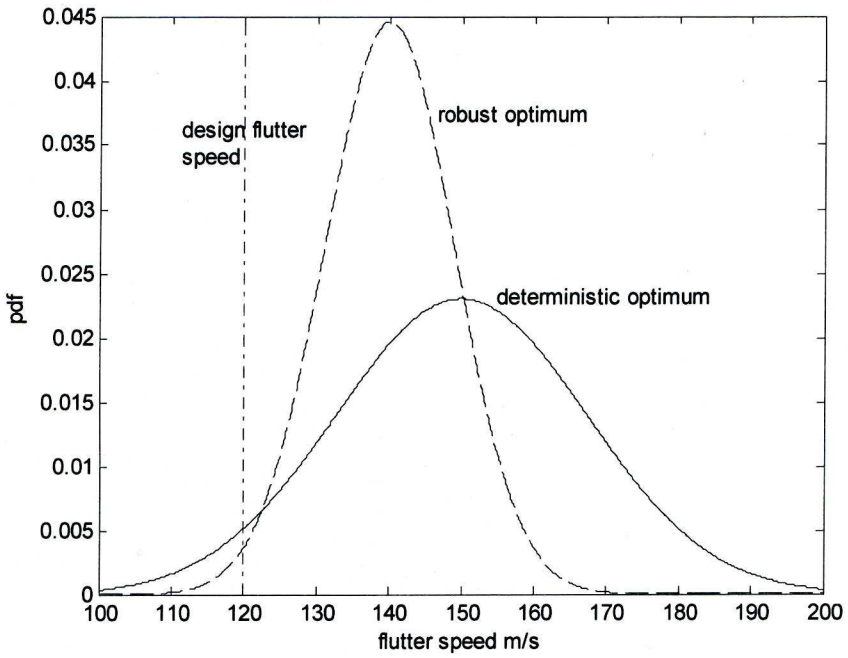

a) Robust Design for Flutter

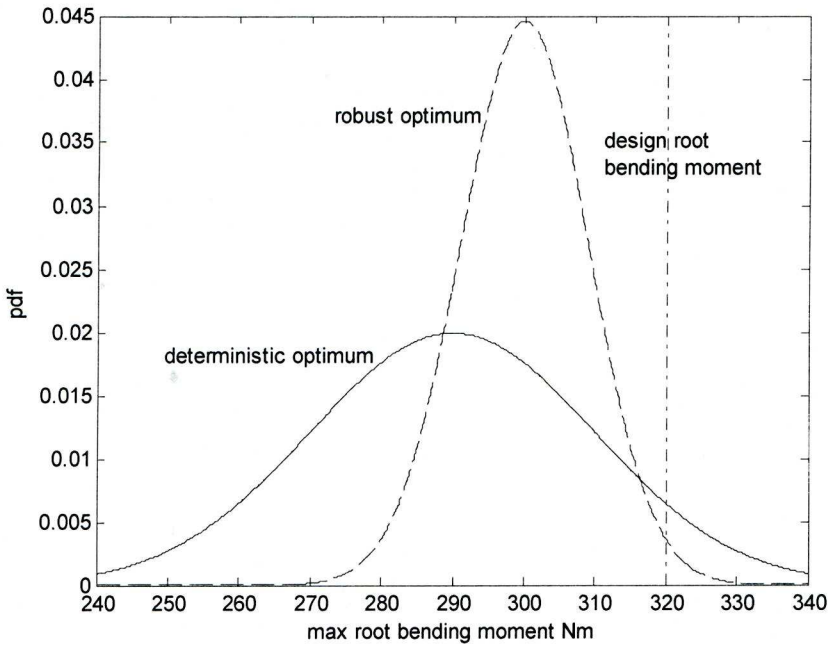

b) Robust Design for Gust Response

Figure 6.1: Robust Design from PCE PDF

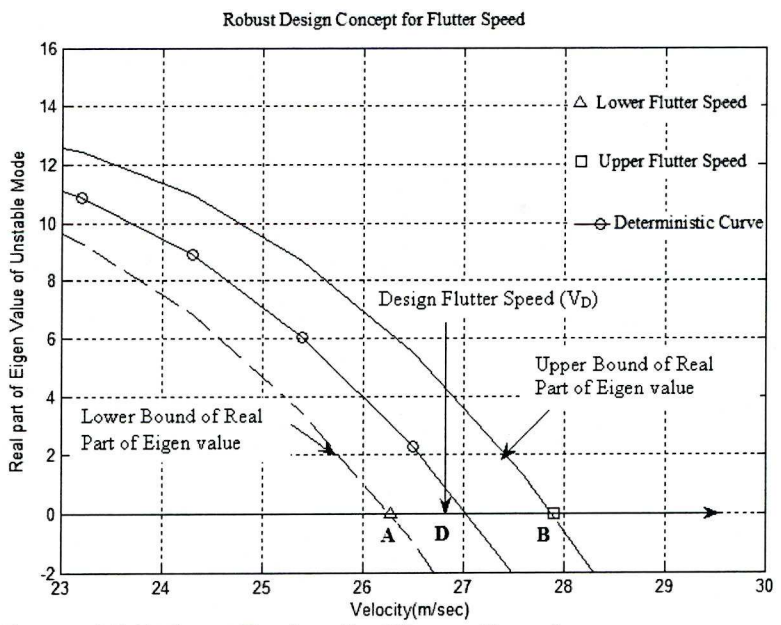

Figure 6.2:Robust Design for Flutter Speed

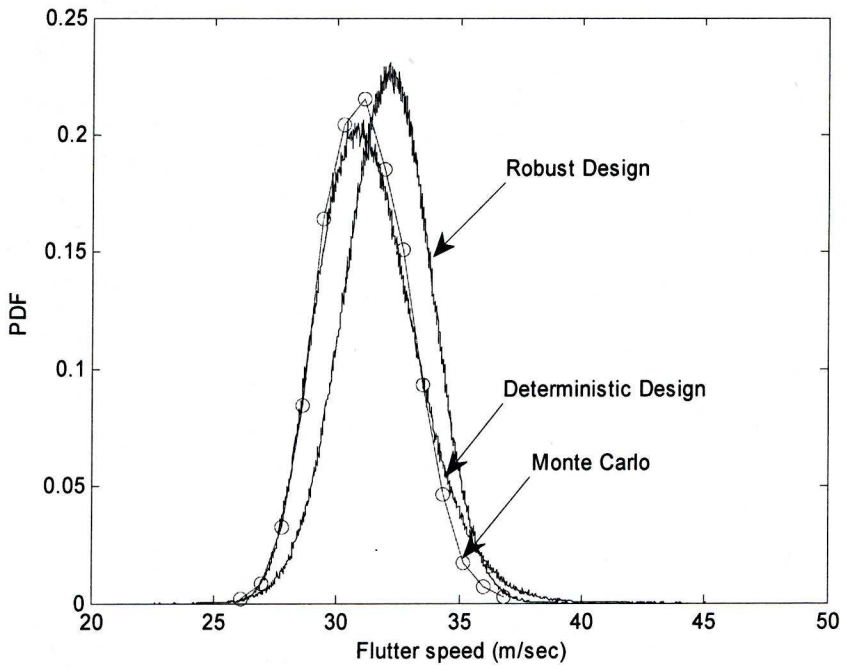

Figure 6.3: Flutter PDFs for Deterministic and Robust Designs

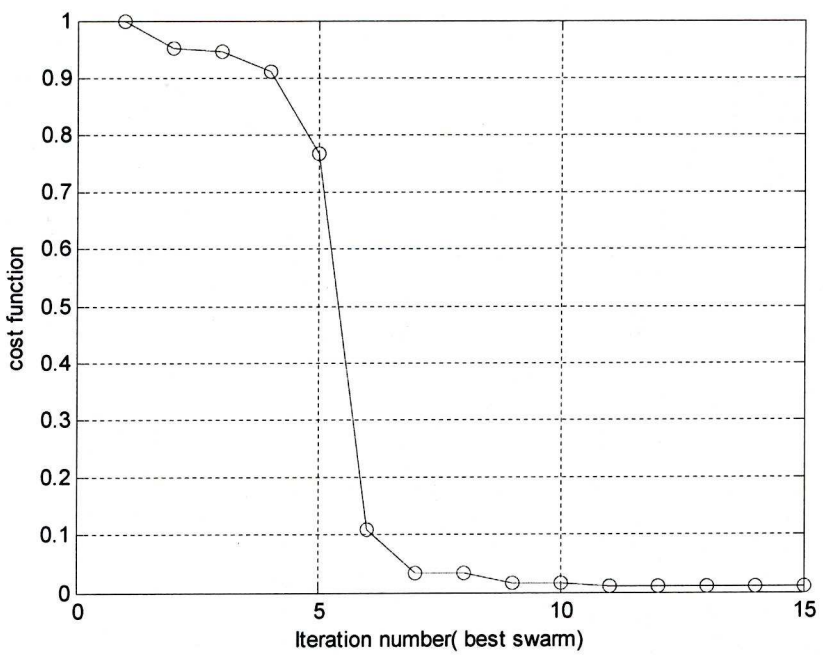

Figure 6.4: Particle Swarm Optimisation Convergence for Robust Optimisation Case

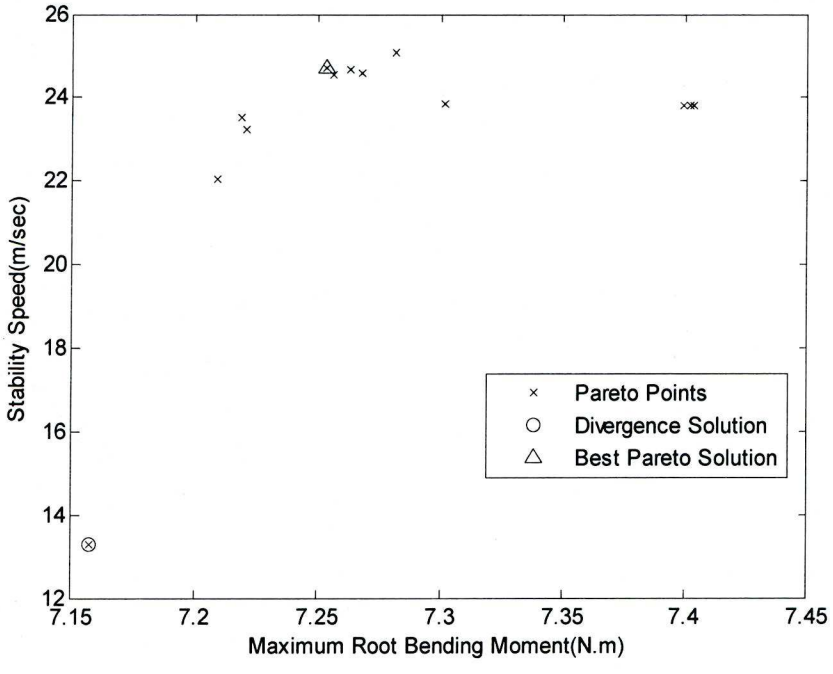

Figure 6.5: Deterministic Pareto Curve (PCE approach)

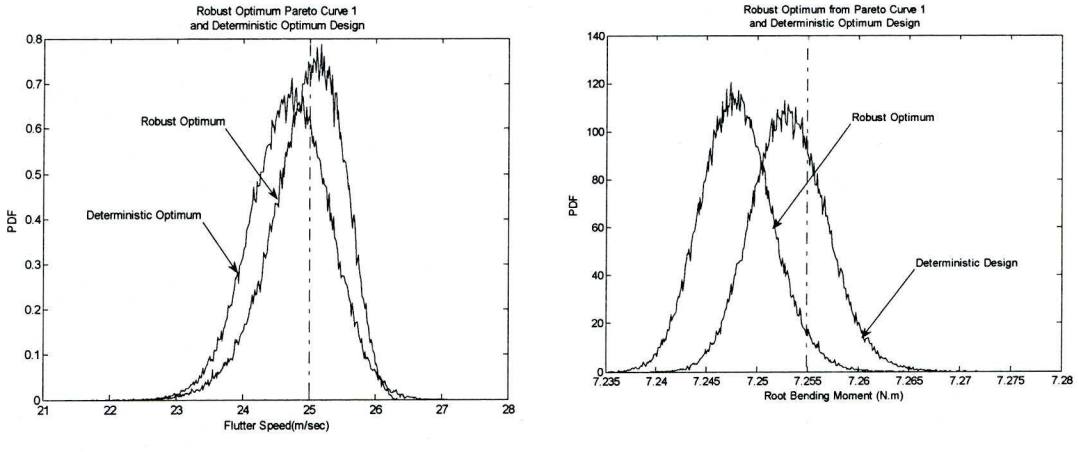

Figure 6.6 a&b: Example 1a: PDFs for Robust and Deterministic Optimum Design(V_d=25m/sec, R_d=7.255N.m)

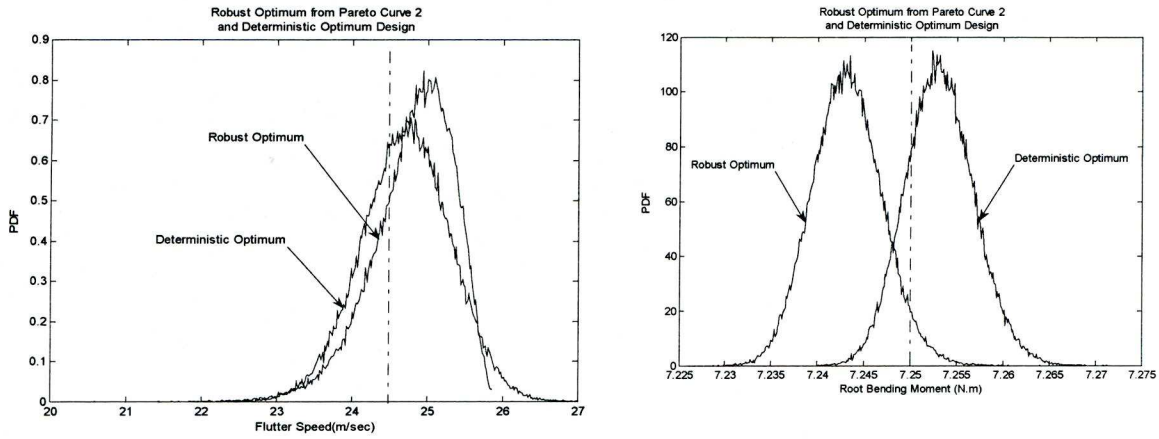

Figure 6.7a&b: Example 1b:PDFs for Robust and Deterministic Optimum Design(V_d=24.4m/sec, R_d=7.25N.m)

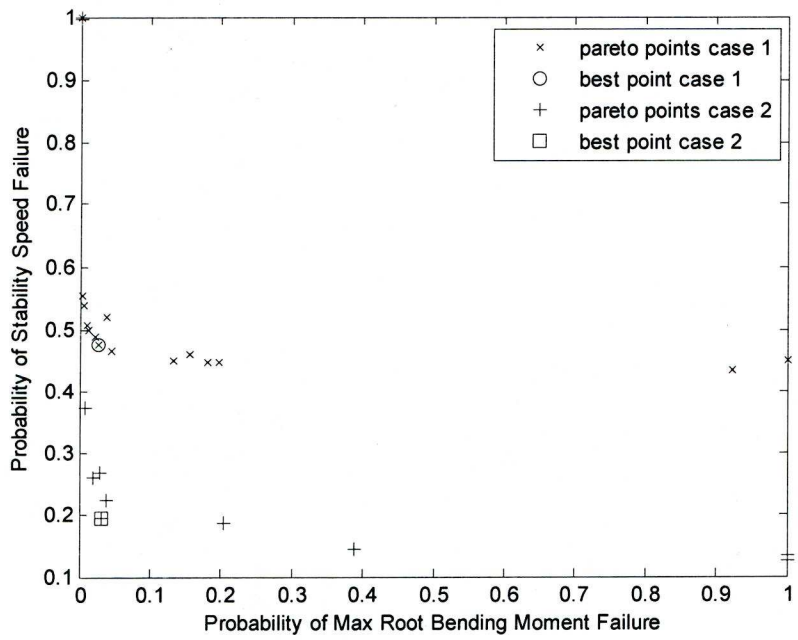

Figure 6.8: Family of Robust Pareto Curves

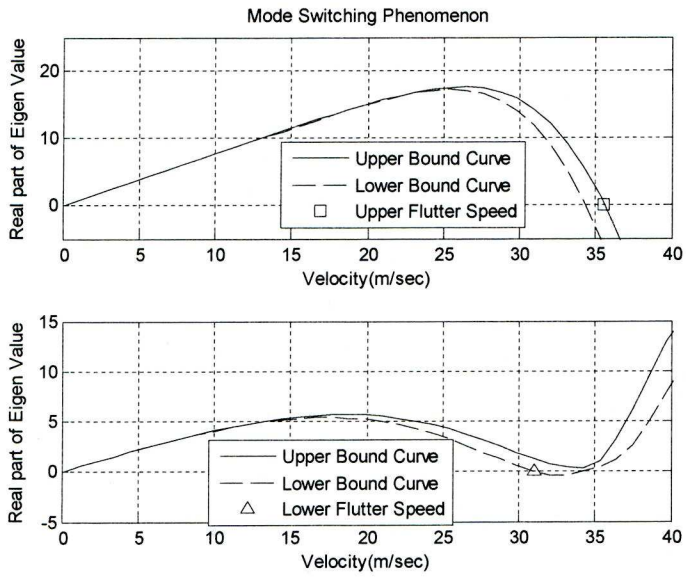

Figure 6.9: Deterministic Optimum Design(Flutter only case) by Interval Analysis approach

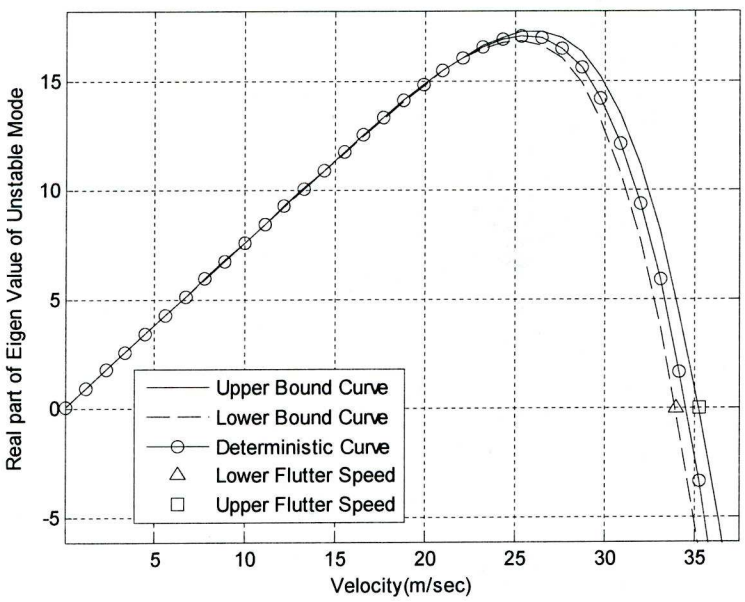

Figure 6.10: Robust Optimum design (Flutter only case) predicted by Interval Analysis

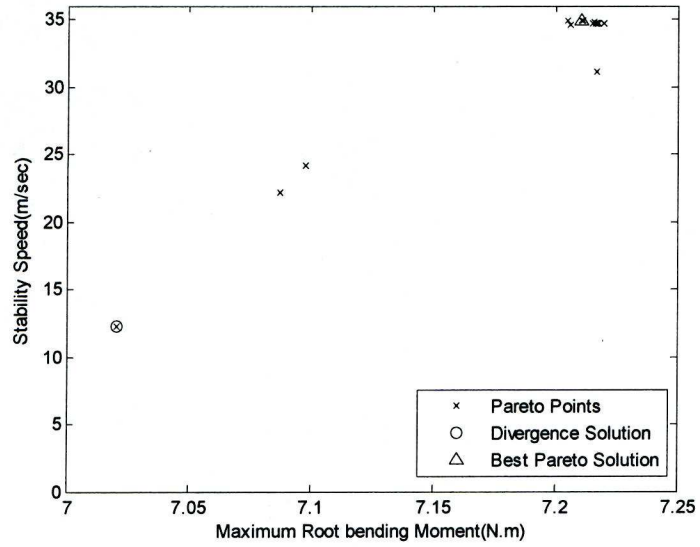

Figure 6.11: Deterministic Pareto Curve (Interval Analysis approach)

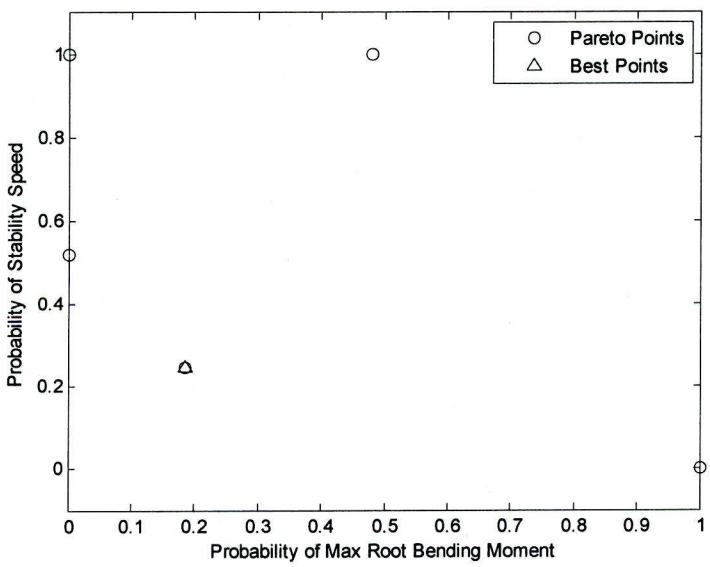

Figure 6.12: Robust Pareto Curve (Interval Analysis Approach)

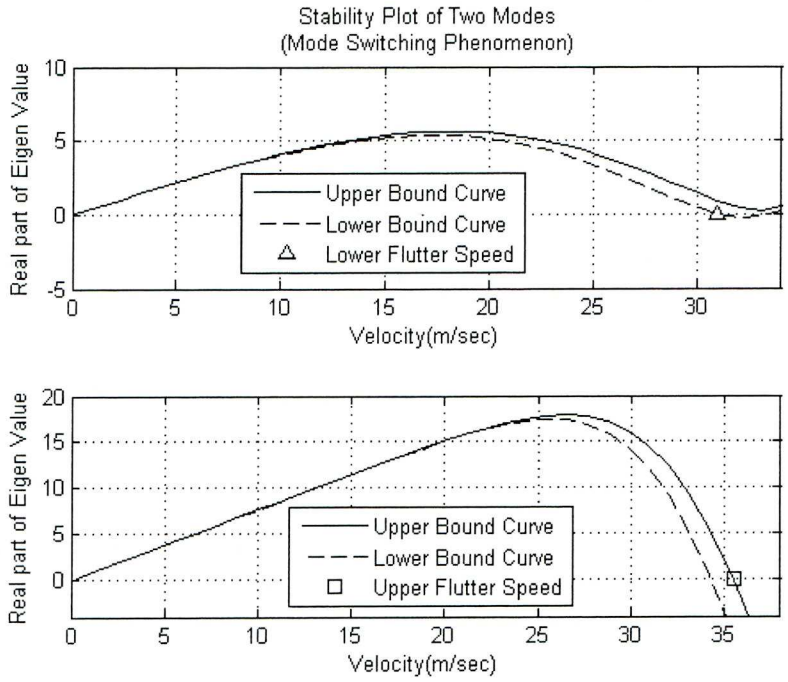

Figure 6.13: Deterministic Optimum Design (Flutter and Gust case)

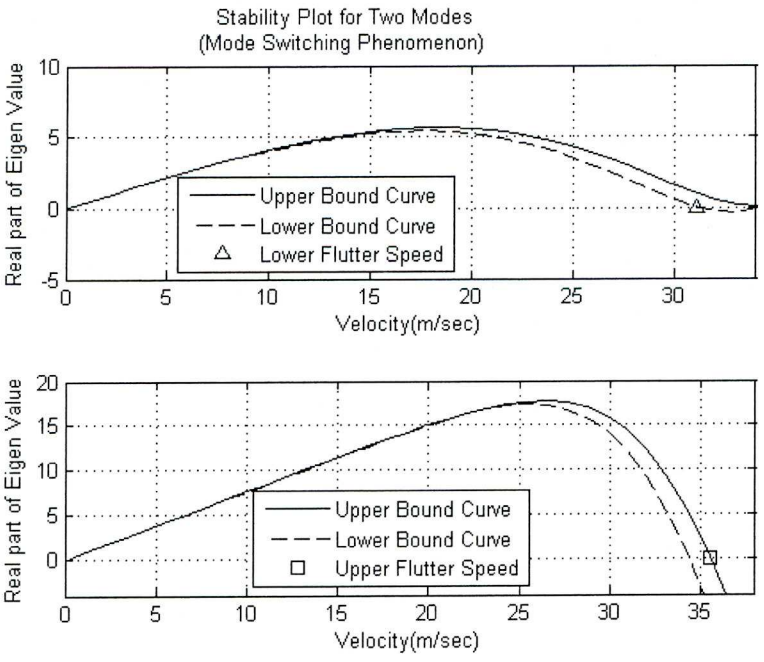

Figure 6.14: Design with w_f=0.7 and w_g=0.3

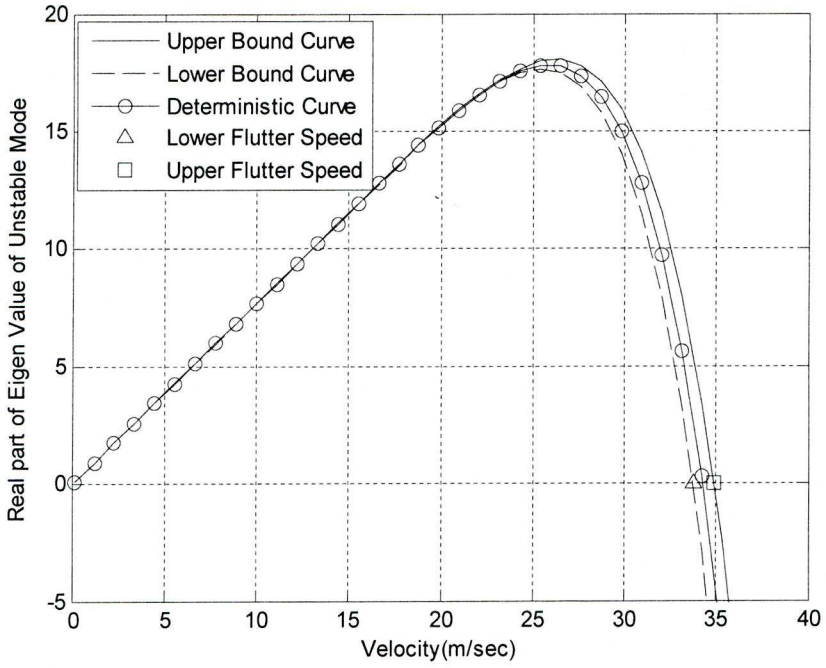

Figure 6.15: Robust Design predicted by Interval Analysis (Flutter and Gust case)

	Flutter Speed (m/s)
Deterministic Optimisation Flutter Speed	32.90
Mean of Monte Carlo Simulations Applied to Deterministic Optimum	31.15
Mean of PCE Applied to Deterministic Optimum	31.17
Mean of PCE Applied to Robust Optimum	32.10

Table 6.1: Flutter Speeds for Different Approaches

Design Flutter Speed	Deterministic Optimum	Robust Optimum
32 m/sec	0.6533	0.4845

Table 6.2: Probability of Failure- Flutter/Divergence only

E_1 GPa	E_2 GPa	G_{12} GPa	υ_{12}	Density kg/m^3
98	7.9	5.6	0.28	1520

Table 6.3: Material Properties Used in present cases.

w_f	w_g	Flutter/Div. Speed (m/sec)	Root Bending Moment (N.m)	θ_1 (°)	θ_2 (°)	θ_3 (°)
1.0	0.0	25.0700	7.2820	-42.3737	47.9617	-44.1302
0.9	0.1	23.8270	7.4017	-23.5154	-35.3039	47.5169
0.8	0.2	23.8270	7.4032	-24.3086	-34.3355	47.0356
0.7	0.3	23.8270	7.3993	-34.9408	-22.5529	45.6406
0.6	0.4	23.8270	7.4031	-33.1148	-24.5205	45.2736
0.5	0.5	24.6630	7.2635	-45.3499	43.5452	-20.1395
0.4	0.6	24.5640	7.2556	43.524	-45.4133	-12.8175
0.3	0.7	24.5970	7.2679	-43.5281	44.8467	-13.4601
0.2	0.8	23.8600	7.3018	-38.6938	1.5951	55.6069
0.1	**0.9**	**24.7290**	**7.2531**	**-45.7300**	**40.0767**	**-45.7167**
0.03	0.97	23.5410	7.2198	31.1043	-36.5689	30.9572
0.02	0.98	23.222	7.2214	-38.6602	29.0288	28.3559
0.01	0.99	22.0560	7.2094	24.5041	-35.9390	24.3028
0.0	1.0	13.29	7.157	18.4704	1.6351	-62.4714

Table 6.4: Results of Deterministic Pareto Curve for PCE example

w_f	w_g	D_{11} (N.m)	D_{16} (N.m)	D_{66} (N.m)	D_{66} / D_{11}	D_{16} / D_{11}
0.9	0.0	12.1184	-4.8096	4.0137	0.331	-0.397
0.8	0.2	12.1513	-4.8628	4.0286	0.331	-0.400
0.7	0.3	12.1918	-4.7651	3.9964	0.328	-0.391
0.6	0.4	12.2265	-4.8848	4.0329	0.33	-0.40

Table 6.5: Stiffness terms for Optimum Design

w_f	w_g	Probability of failure for Flutter/Div. Speed	Probability of failure for Root Bending Moment	θ_1 (°)	θ_2 (°)	θ_3 (°)
1.0	0.0	0.4320	0.9228	-44.9057	44.6058	43.6562
0.94	0.06	0.4488	0.1322	-46.1729	42.6892	41.6163
0.93	0.07	0.4489	1.00	-42.8459	47.2415	-42.9535
0.92	0.08	0.4581	0.1545	-45.4179	42.5114	42.5165
0.91	0.09	0.4473	0.1811	-46.3069	42.7451	42.5165
0.9	0.1	0.4456	0.1964	-46.6026	43.1476	41.9994
0.8	0.2	0.4645	0.0458	-45.4093	41.7612	40.4985
0.7	0.3	0.5186	0.0384	-43.4647	41.1686	37.6573
0.6	**0.4**	**0.4753**	**0.026**	**-45.0396**	**40.9335**	**42.5863**
0.5	0.5	0.4870	0.0212	-44.9181	41.3812	38.0406
0.4	0.6	0.50	0.012	-44.6446	40.7416	39.5151
0.3	0.7	0.5374	0.0049	-44.0513	40.2991	36.9742
0.2	0.8	0.5058	0.0113	-44.5136	40.6856	39.1529
0.1	0.9	0.555	0.0041	-43.8885	39.2242	43.0712
0.0	1.0	1.00	0.00	-0.1804	22.4598	21.0108

Table 6.6: Pareto Points. Example 1a. Probability of failure for V_d=25m/sec and R_d=7.255N.m

w_f	w_g	Probability of failure for Flutter/Div. Speed	Probability of failure for Root Bending Moment	θ_1 (°)	θ_2 (°)	Θ_3 (°)
1.0	0.0	0.1257	1.00	-44.6763	44.7538	45.7829
0.95	0.05	0.1333	1.00	-42.7783	46.9172	42.5027
0.9	0.1	0.1431	0.3876	-45.5041	42.2772	36.8100
0.85	0.15	0.1845	0.2041	-43.6924	39.7344	44.9365
0.8	0.2	0.9960	0.0016	-41.1930	29.0702	-44.3151
0.7	0.3	1.00	0.00	-13.8436	21.2166	25.4918
0.6	0.4	1.00	0.00	-4.7522	23.9674	30.0159
0.55	**0.45**	**0.1943**	**0.032**	**-43.5662**	**39.6119**	**35.5990**
0.5	0.5	0.3725	0.009	-42.2486	38.7858	25.9278
0.4	0.6	0.2586	0.019	-42.5242	38.1823	38.9942
0.3	0.7	0.223	0.039	-43.9076	40.2159	31.0037
0.25	0.75	0.266	0.029	-42.0308	38.5420	36.3310
0.2	0.8	1.00	0.00	-9.3498	22.7460	25.6460
0.1	0.9	1.00	0.00	2.0978	17.1528	32.3017
0.0	1.0	1.00	0.00	-5.800	23.412	25.9100

Table 6.7: Pareto Points. Example 1b. Probability of failure for V_d=24.4m/sec and R_d=7.25N.m

	Design Speed m/sec	Design Root Bending Moment N.m	Probability of failure against Flutter/divergence speed	Probability of failure against gust
Deterministic Optimum	25	7.255	0.6855	0.2922
	24.4	7.25	0.2957	0.8120
Robust Optimum Best Pareto Point	25	7.255	0.4753	0.026
	24.4	7.25	0.1943	0.032

Table 6.8: Probability of Failure

w_f	w_g	Flutter/Div. Speed (m/sec)	Root Bending Moment (N.m)	θ_1 (°)	θ_2 (°)	θ_3 (°)
1.0	0.0	34.8930	7.2112	-20.4084	39.0024	33.3321
0.9	0.1	34.7060	7.2195	-21.6988	37.0906	-16.8319
0.8	0.2	34.6840	7.2162	-20.0930	38.0668	-44.1519
0.7	0.3	34.8710	7.2103	-20.5468	36.1805	48.3433
0.6	0.4	34.6840	7.2154	-20.3420	36.9206	-39.6042
0.5	0.5	34.7830	7.2159	-21.4165	39.8181	10.2347
0.4	0.6	34.6950	7.2170	-20.2604	37.8735	-40.8794
0.3	0.7	34.6950	7.2175	-21.0158	36.3979	-29.4627
0.2	**0.8**	**34.8490**	**7.2048**	**-20.3406**	**36.3164**	**32.202**
0.1	0.9	34.5630	7.2062	-21.8435	33.6172	3.4577
0.05	0.95	31.0870	7.2170	-39.8332	38.9815	39.1573
0.02	0.98	24.1790	7.0974	15.7414	-28.1075	-18.9463
0.01	0.99	22.2100	7.0874	15.6521	-23.3485	13.8908
0.0	1.0	12.2220	7.0202	16.4276	16.4280	16.4279

Table 6.9: Results of Deterministic Pareto Curve-For Interval Analysis Method

w_f	w_g	$MOF_{flutter}$	MOF_{gust}	θ_1 (°)	θ_2 (°)	θ_3 (°)
0.0	1.0	1.0	0.0	-8.5005	39.1642	26.2527
0.1	0.9	0.5119	0.0	-21.1438	27.9443	31.5643
0.2	0.8	1.0	0.0	-7.6565	9.6980	29.3213
0.3	0.7	1.0	0.0	-11.2546	26.7896	10.2800
0.4	0.6	1.0	0.0	-16.0225	17.5030	40.2873
0.5	**0.5**	**0.244**	**0.1864**	**-20.5017**	**30.8953**	**32.6836**
0.6	0.4	1.0	0.0	-2.6322	19.9242	4.8372
0.7	0.3	1.0	0.0	-7.494	19.9217	42.2058
0.8	0.2	1.0	0.0	-6.0055	17.8585	1.4671
0.9	0.1	1.0	0.4790	-20.2357	33.8524	31.5521
1.0	0.0	0.0	1.00	-20.2501	41.1163	36.1406

Table 6.10: Results of Robust Pareto Data-Interval Analysis Approach

	$MOF_{flutter}$	MOF_{gust}
Deterministic Optimum Design	0.67	0.85
Robust Optimum Design	**0.24**	**0.19**

Table 6.11: Measure of failure of Robust and Deterministic Design

Chapter 7

Effect of Damage on Aeroelastic Response of Aircraft Composite Wing

7.1 Introduction

Composite materials are being used increasingly in aerospace structures; however, sources of uncertainty in such structures do exist apart from the structural parameters, which include matrix cracking[2, 3], moisture absorption, fibre breakage caused by excessive loading or fatigue. The aeroelastic behaviour (stability and response) for composite wings is sensitive to these damage uncertainties.

Before developing the probabilistic PCE model by including the damage uncertainty, the deterministic approach is applied first to analyse the effects of damage (with known value and locations) on the aeroelastic stability and response of the composite wing.

In the Talreja approach, experimentally determined material constants[2] were utilized to develop a damaged material model. In this model, the longitudinal Young's modulus was negligibly affected, however, the transverse Young's modulus, Poisson's ratio and shear modulus were lowered significantly depending upon the crack density. In the self-consistent approach, the damaged material model was calculated for varying amounts of crack density. In this approach, transverse Young's and Shear moduli were largely affected, whereas longitudinal Young's modulus and Poisson ratio remained unaffected. The fibre breakage phase was also incorporated in both the approaches.

To simulate the fibre breakage phase, all of the material properties of the corresponding layer were lowered almost to zero (very small values were assumed to overcome the finite element analysis computational difficulties).

In this chapter, the effect of damage on the flutter speed, gust response due to '1-cosine' discrete gust, static wing bending deflection and wing twist at a particular flight condition are predicted and compared with an undamaged case. A more realistic full-scale aircraft FE wing model is selected in this regard.

7.2 Aeroelastic Response-Without Damage

The full-scale aircraft FE composite wing 4 is considered.

7.2.1 Flutter Analysis-Without Damage

Before performing a flutter analysis, the wind-off frequencies of the composite wing were determined using NASTRAN 103 solver from which bending, torsion and sway modes are identified. Here first eight mode shapes with frequency values are shown in Figure 7.1 to Figure 7.8.

Once the mode shapes and their frequencies are identified and established, the same structural wing model was coupled with the aerodynamic model, which is defined via Doublet Lattice Method. The PK method, a frequency matching technique, was adopted to find the flutter speed and frequency using the NASTRAN 145 solver.

The flutter phenomenon is caused due to the unfavourable interaction of two modes, here the 2nd Bending and 1st Torsion modes show such an interaction as shown in Figure 7.9 and the 2nd Bending mode eventually

became unstable (i.e. its damping value becomes zero) at 167.5 m/sec with a frequency value of 18.6 Hz.

7.2.2 Gust Response Due to "1-Cosine" Discrete Gust-Without Damage

In this section, "1-cosine" discrete gust response is calculated against some gust signal (see Figure 7.10a). The leading edge tip, trailing edge tip deflection and root bending moment are calculated(see Figure 7.10b,c,d) by using the NASTRAN 146 solver.

7.2.3 Static Deflection and Twist of Composite Wing-Without Damage

The designed composite wing is assessed in terms of the leading and trailing edge tip deflection and twist against a particular flight condition. Following flight conditions are assumed in the present study:

Angle Of Attack= AOA= 2^{o} ; Speed = 90 m/sec
Dynamic Pressure= 4.96 KN/m^2; Mach number =0.5

Other assumptions are that the pitching and lateral effects are zero. NASTRAN 144 solver was utilized to determine static deflection and twist of the wing.

The difference between the vertical deflection on leading edge and trailing edge per chord gave a twist value of -1.94^{o}. The negative sign of the twist angle was due to more trailing edge tip vertical deflection compared with the leading edge. The deflection plot of corresponding grid points are shown in Figure 7.11.

7.3 Aeroelastic Response- With Damage

The effect of damage on an aeroelastic response is studied in this section. Two damage models are utilized i.e. the Talreja and Self-consistent Methods. In Aeroelastic behaviour, flutter speed, gust response, static deflection and twist of the composite wing are predicted by utilizing these damage models against various levels of damage defined via following cases:

Case 1: Transverse Matrix Cracking with crack density of 0.1
Case 2: Transverse Matrix Cracking with crack density of 0.4
Case 3: Transverse Matrix Cracking with crack density of 0.4 and fibre breakage at specified location.

Definition of the damage location and damaged layers

In the present study, the damage locations are assumed in top skin, bottom skin, front spar and rear spar. One location is arbitrary selected close to the root section of the wing to incorporate the fibre breakage phase.

The front and rear spars of lay-up $((-45^{o})_4)_s$ is replaced with $((-d^{o}/d^{o}/-45^{o}/-45^{o})_4)_s$, where 'd' represents a layer of the same angle but with the transverse matrix cracks. Similarly, the top and bottom skins at the four locations (two for each) are represented with $((-d^{o})_2/(d^{o})_3/d^{o})_s$, whereas rest of the skin layers have no damage(See Figure 7.12).

The damaged layers properties are calculated by adopting the Talreja and Self-consistent methods while the layer with the broken fibres has material properties values equal to the order of 1e-9 of the undamaged values.

7.3.1 Flutter Analysis-With Damage

The Talreja damage model is adopted first for all the three cases one by one to predict the flutter speed of the wing. Reduced material properties of a damaged layer for each crack density values are tabulated in Table 7.2 and summary of the results is presented in Table 7.3 while effect of the various damage levels on the flutter speed is shown in Figure 7.13.

It is interesting to note that when the crack density is low (β=0.1) means with less numbers of matrix cracks, the reduction in the flutter speed was minimal whereas with the crack density of 0.4 it became ~0.6% and increased to approximately ~ 2% when the layers with broken fibres were included.

The Self-consistent Model was now applied on the above cases. Here again first step involves calculating the reduced material properties for various levels of damage which is tabulated in Table 7.4. A summary of results for all these cases is presented in Table 7.5 whereas variation in the flutter speed due to damage is shown in Figure 7.14.

Variation in the flutter speed values are approximately same compared with the Talreja model predicted values.

These results are only valid for the studied damage level and location defined in the present work. It is very much possible that results can vary for the same damage level but with the changed locations.

7.3.2 Gust Response- With Damage

In order to predict the gust response, layers not only with the broken fibres but also of the matrix cracks with a crack density of 0.4 were included in the wing model. Leading and trailing edge tip deflections

and root bending moment were noted and it was found that the trailing edge deflection was increased by ~1.0 %(0.195m to 0.197m) and a very minimal effects on the root bending moment was noted. Main reason is that gust is a stiffness driven mechanism and for this case, effects are minimal (see Figure 7.15) and can be ignored.

7.3.3 Static Deflection and Twist of Wing- With Damage

In order to predict the static deflection and twist of the wing, layers not only with the broken fibres but also of the matrix cracks with a crack density of 0.1 and 0.4 were included in the model. The Talreja and Self-consistent Damage Models were adopted for the said cases and leading edge, trailing edge tip deflection and wing twist were calculated against flight conditions defined in the section 7.2.3. Results are presented in Table 7.1 and it was found that the wing twist of -1.94° remained the same for all the cases and can be concluded that effects on the twist value due to the above said damage level and locations could be ignored. To determine these values NASTRAN 144 solver was utilized.

7.4 PCE approach for bounds on flutter speed due to structural and damage uncertainties

In this section, uncertainty in the crack density was treated as a probabilistic manner along with the longitudinal modulus of the composite wing. Crack density has a mean value of 0.275 with coefficient of variation of 0.15 and E_1 has a mean value of 135 GPa with coefficient of variation of 0.03. The damage locations were assumed in the top skin, bottom skin, front spar and rear spar. One location was arbitrary selected close to the root section of the wing to incorporate the fibre breakage phase.

The front and rear spars of lay-up $((-45^{o})_4)_s$ was replaced with $((-d^{o}/d^{o}/-45^{o}/-45^{o})_4)_s$, where 'd' represents a layer of the same angle but with the transverse matrix cracks. Similarly, the top and bottom skins at the four locations (two for each) are represented with $((-d^{o})_2/(d^{o})_3/d^{o})_s$, whereas rest of the skin layers have no damage(See Figure 7.12).

PDF obtained for both the cases (structural uncertainty only and structural and damage uncertainty) are shown in Figure 7.16. There is no considerable shape difference noted in both except that the PDF corresponding to the structural and damage uncertainties shifts towards the lower flutter speed value and contribution of the damage uncertainty to the PDF shape is negligible for this wing design. Possible reason to this result is that layers with the matrix cracks are assumed symmetric in the layup configuration.

When cracked layers are asymmetric in the lay-up, the influence of the cracks on the shape of the PDF and flutter speed value may be different probably due to the coupling terms appearing in the structural stiffness matrix. PDF estimate approach defined in Chapter 6 may be applied to such problems to explore the feasibility of the damage tolerant designs.

7.5 Conclusions

1. In this chapter, two damage models i.e. the Talreja and two-phase methods were applied by considering the transverse matrix cracking and fibre breakage phases to predict variation in the aeroelastic stability and response of the aircraft composite wing model. Flutter speed, gust response due a "1-cosine" discrete gust and the static wing bending deflection and twist for a flight condition was studied and presented. It was found that transverse matrix cracks along with the layers with broken fibre have a significant effect on the flutter speed (~ 2% reduction)

whereas variation in the RBM and the static wing tip twist values were negligible for the studied case. Reduction in the flutter speed, a dynamic phenomenon, was largely due to the variation of the interaction of modes caused by the variation in the damage uncertainties.

2. The Talreja and two-phase models predicted approximately the same reduction value of the flutter speed.

3. The effect of damage on the wing twist and tip deflections, which are produced from the static analysis at a particular flight speed, were minimal because these are mainly a stiffness driven static phenomenon and at a wing level, the stiffness reduction due to the damage was very small. However, for a larger damage scenario results may vary.

4. The PCE approach, by including damage uncertainties, can lead to explore the feasibility of damage tolerant aeroelastic designs.

	Talreja Model			Two-Phase Model		
	Case 1	Case 2	Case 3	Case 1	Case 2	Case 3
LE Tip Deflection(m)	0.351	0.353	0.353	0.352	0.353	0.353
TE Tip Deflection(m)	0.368	0.3701	0.370	0.369	0.370	0.370
Twist(~^{o})	-1.94	-1.94	-1.94	-1.94	-1.94	-1.94

Table 7.1: Static Deflection and twist of Composite Wing

	Un-Damage	Damage (β=0.1)	Damage (β=0.4)
E_1(GPa)	136.5	135.9	135.4
E_2(GPa)	10.0	9.56	6.62
υ_{12}	0.3	0.28	0.22
G_{12} (GPa)	4.8	4.8	4.8
Ply thickness(mm)	0.125	0.125	0.125
Density(Kg/m^3)	1570	1570	1570

Table 7.2: Reduced Stiffness Properties at various Crack Densities by Talreja Model

	Without Damage	Case1	Case 2	Case 3
Flutter Speed(m/sec)	167.53	167.42	166.57	164.43
Flutter Frequency (Hz)	18.60	18.59	18.46	18.34

Table 7.3: Flutter Speed of wing for various Cases (Talreja Method)

	Un-Damage	Damage β=0.1	Damage β=0.4
E_1(GPa)	136.5	136.5	136.5
E_2(GPa)	10.0	8.77	7.02
υ_{12}	0.3	0.3	0.3
G_{12} (GPa)	4.83	4.54	4.12
Ply thickness(mm)	0.125	0.125	0.125
Density(Kg/m^3)	1570	1570	1570

Table 7.4: Reduced Material Properties at various Crack Density levels(β) by Two-phase Damage Model

	Without Damage	Case1	Case 2	Case 3
Flutter Speed(m/sec)	167.53	167.15	166.55	164.41
Flutter Frequency (Hz)	18.60	18.54	18.45	18.33

Table 7.5: Flutter Speed of wing with and without Damage for various Cases

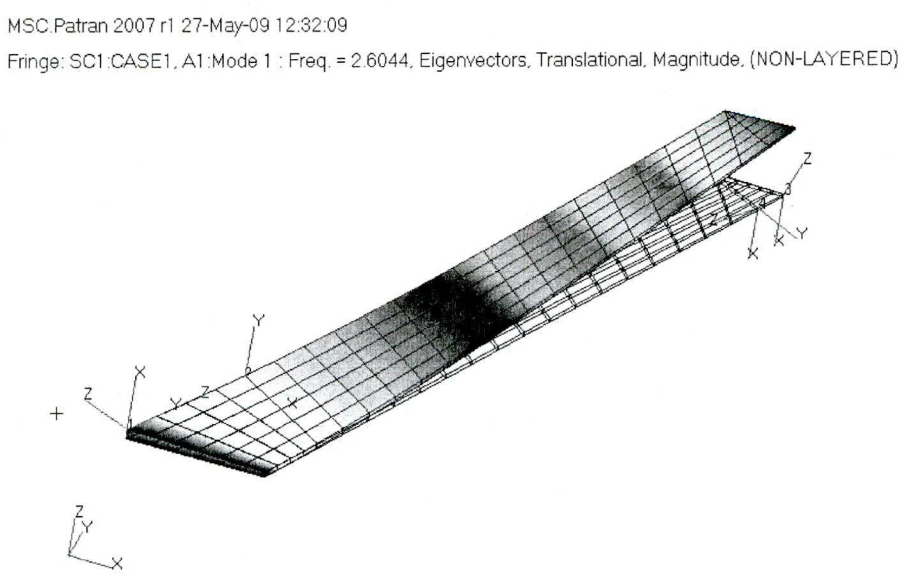

Figure 7.1: 1st Bending Mode at 2.6 Hz

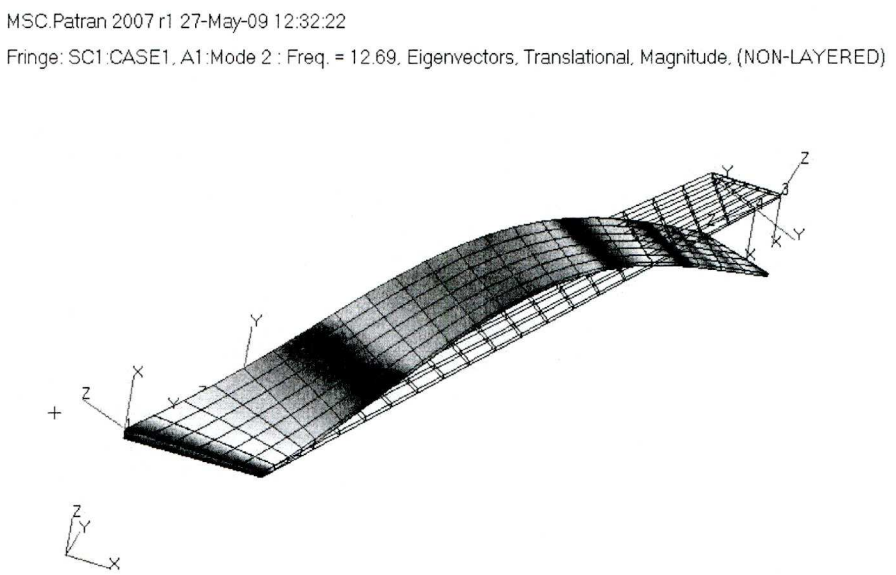

Figure 7.2: 2nd Bending mode at 12.69 Hz

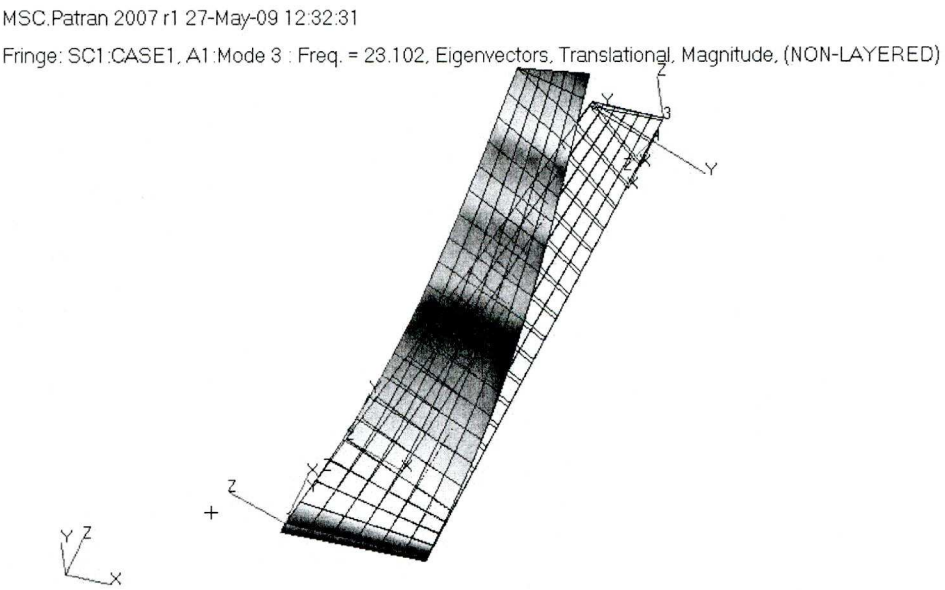

Figure 7.3: 1st Sway Mode at 23.1 Hz

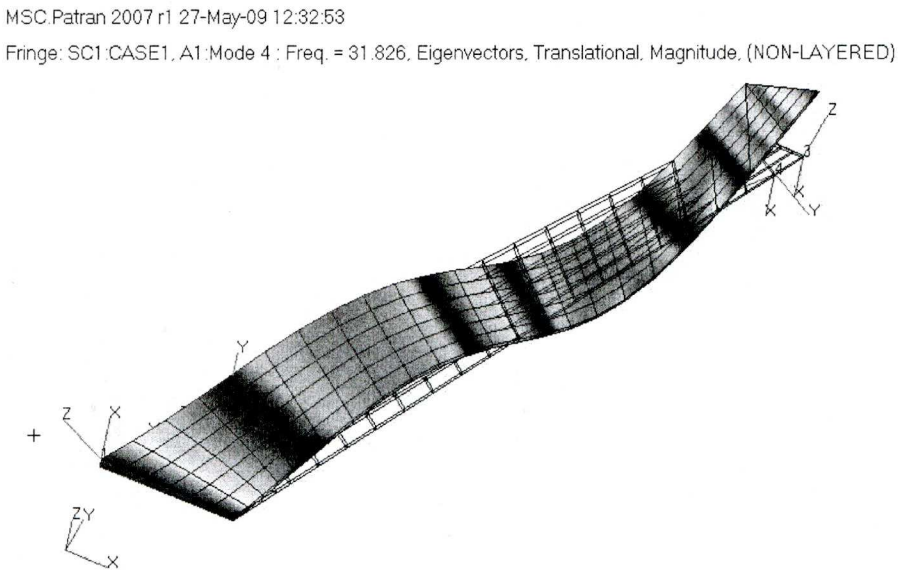

Figure 7.4: 3rd Bending Mode at 31.83 Hz

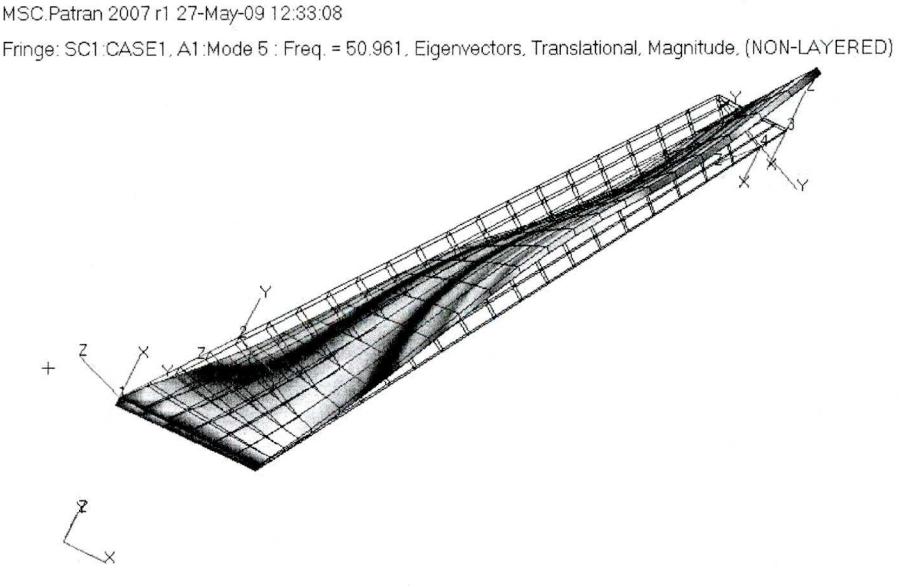

Figure 7.5: 1st Torsion Mode at 50.96 Hz

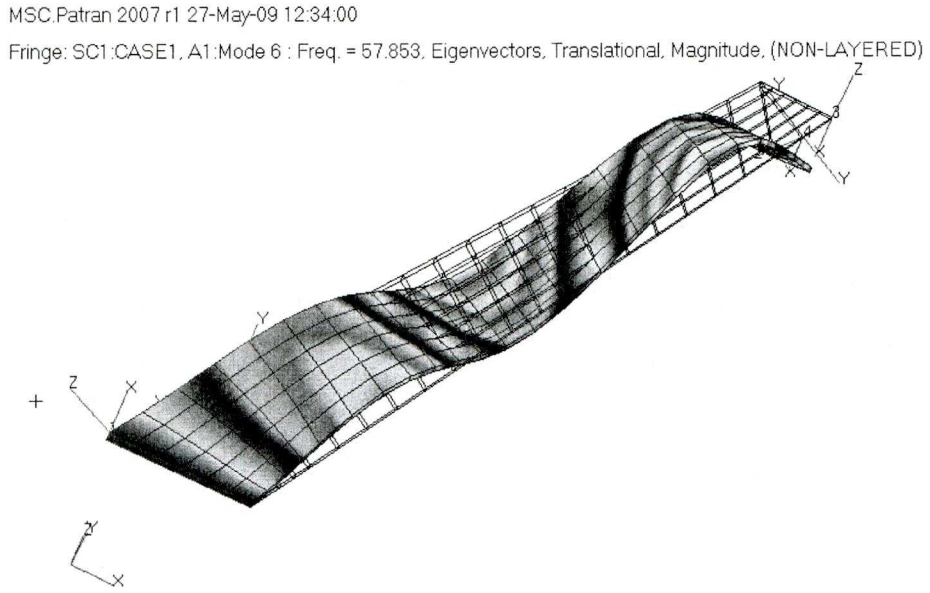

Figure 7.6: 4th Bending Dominant Mode at 57.85 Hz

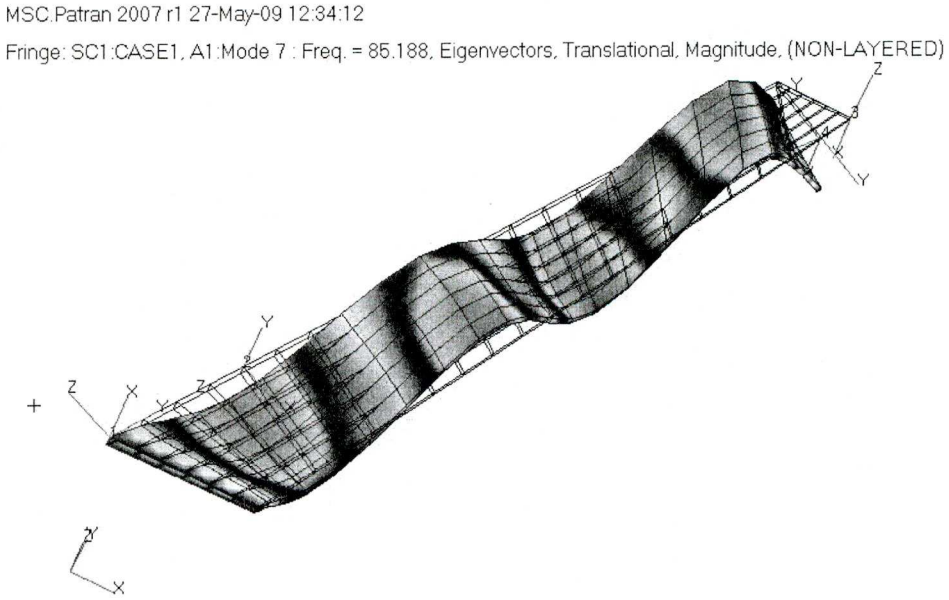

Figure 7.7: 5th Bending Dominant Mode at 85.19 Hz

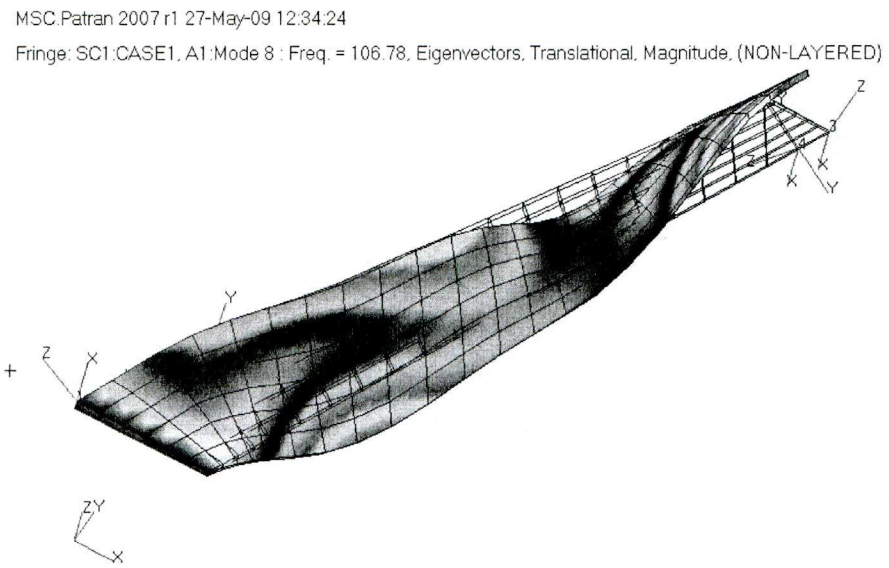

Figure 7.8: 2nd Torsion Dominant Mode at 106.78 Hz

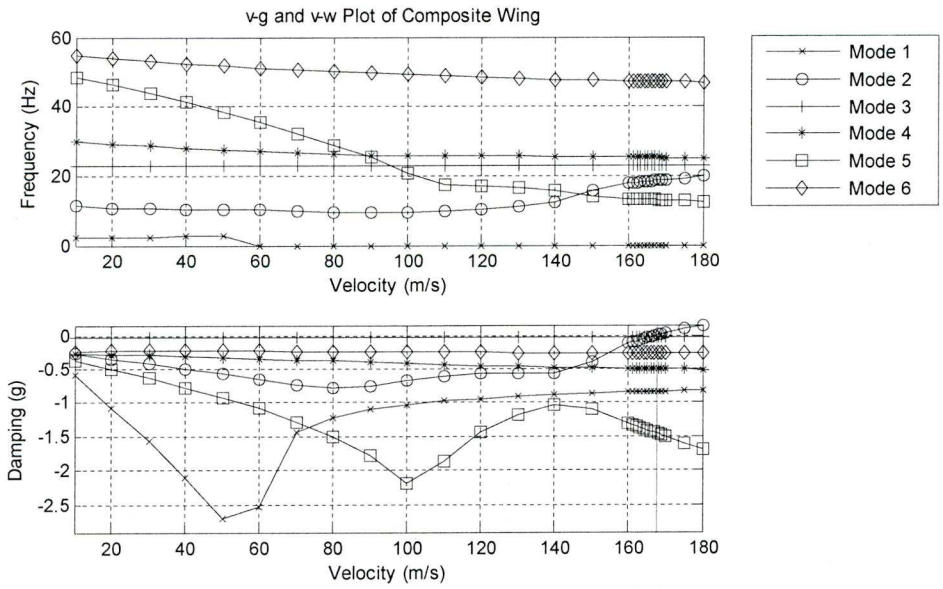

Figure 7.9: v-g and v-w plot to predict Flutter Speed and Frequency

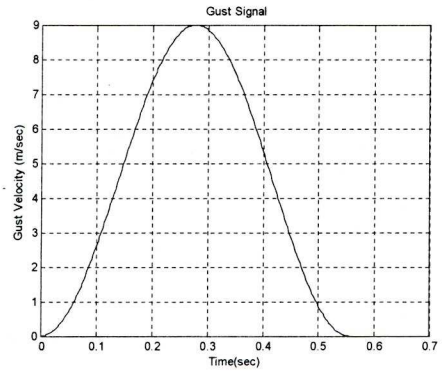

a) Gust signal

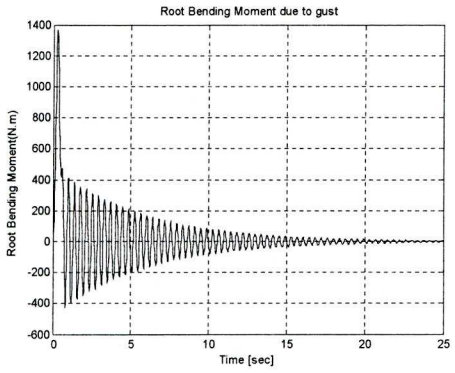

b) Root bending moment

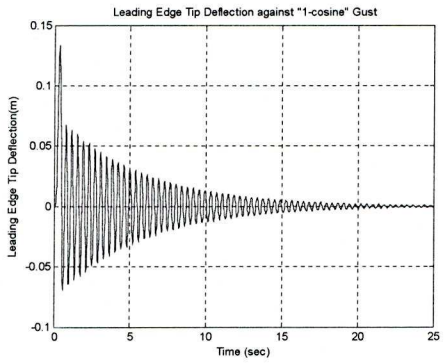

c) Leading edge tip deflection

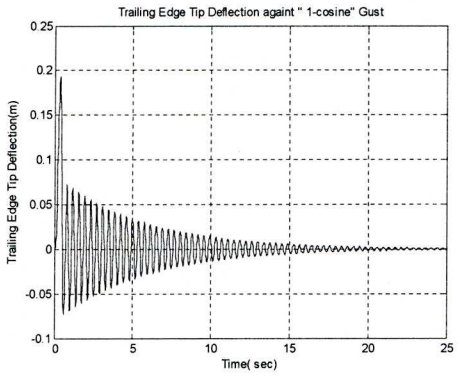

d) Trailing edge tip deflection

Figure 7.10: Gust signal and LE and TE tip deflection(Un-Damage)

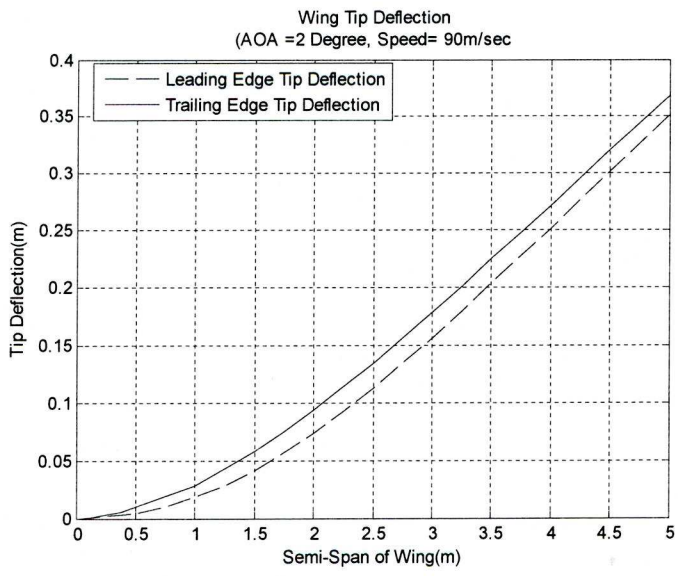

Figure 7.11: Tip Deflection and Twist of Composite Wing

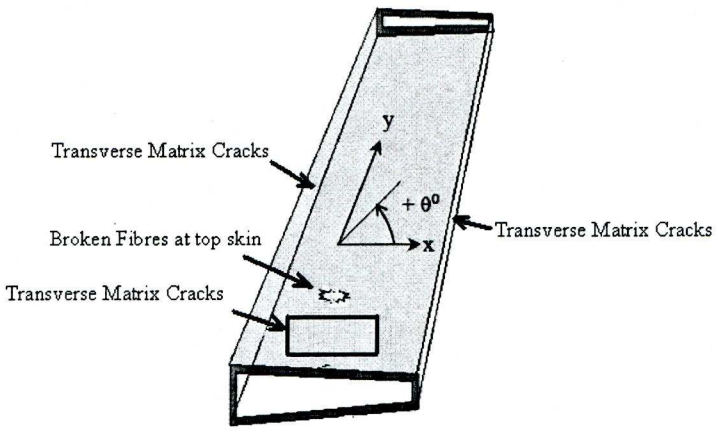

Figure 7.12: Location definition of damage

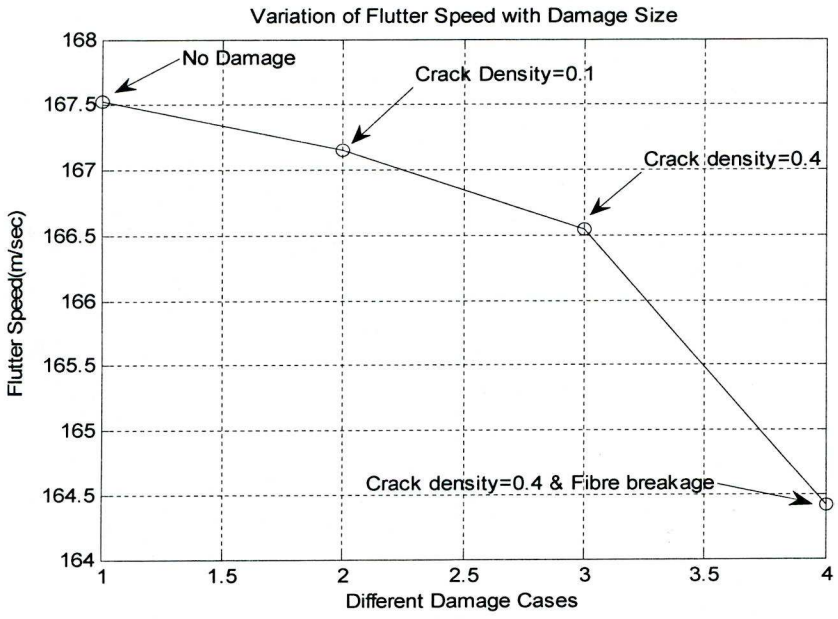

Figure 7.13 : Effect of various levels of damage on the flutter speed by Talreja Model

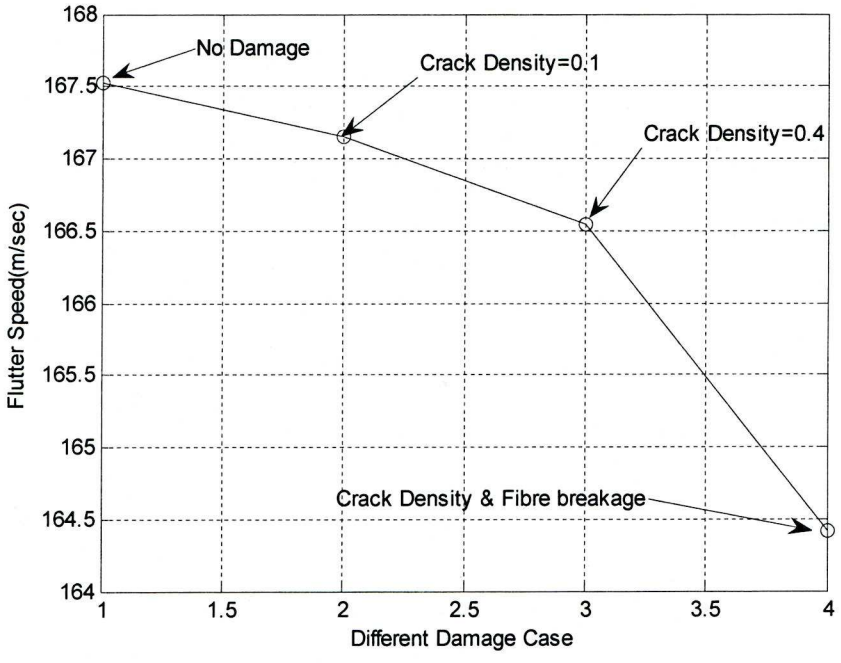

Figure 7.14: Variation in flutter speed by using Two-phase Damage Model

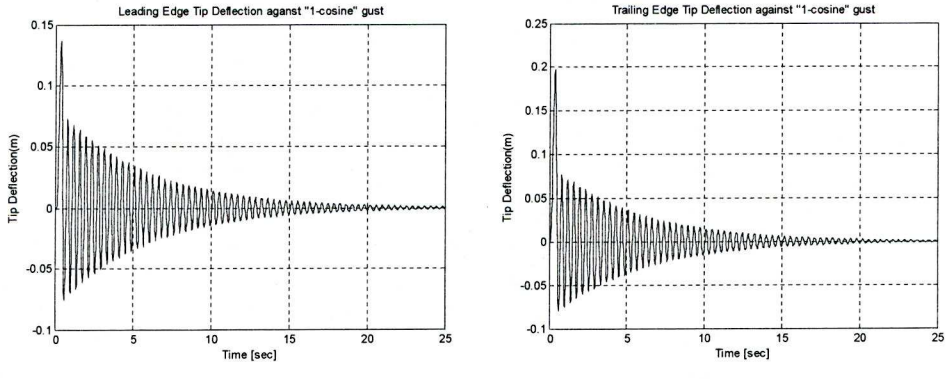

b) Leading edge tip deflection c) Trailing edge tip deflection

Figure 7.15:Leading and trailing edge tip deflection

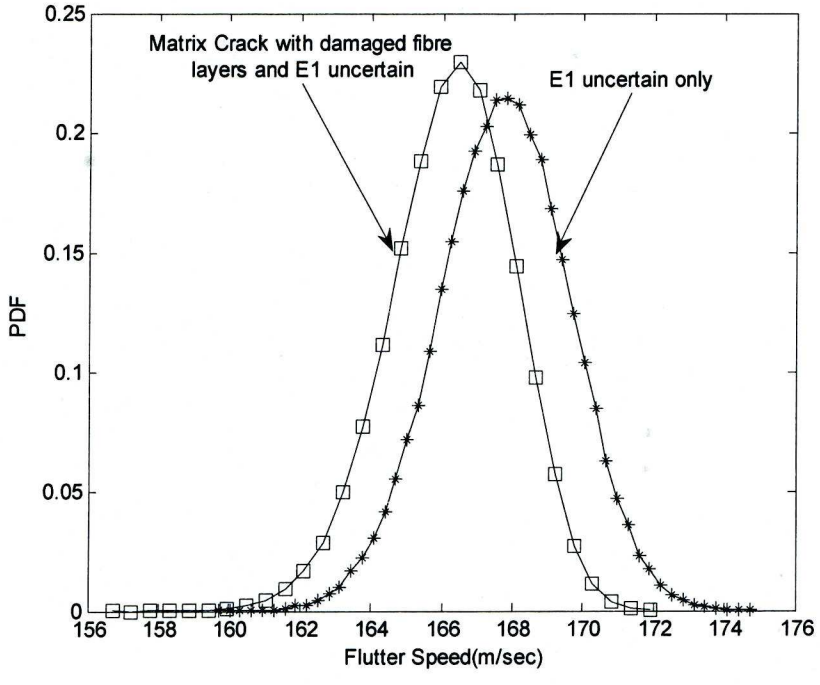

Figure 7.16: PDF of composite wing with structural and structural and damage uncertainties.

Chapter 8

Conclusions and Future Work

Conclusions

The deterministic aeroelastic models for the flutter speed, divergence speed, gust response due to 1-cosine discrete gust and a simplified aero-servo-elastic model for the active control of the gust were derived for the idealised composite wing model. Binary Genetic Algorithm and Particle Swarm Optimisation approaches were integrated with the aeroelastic model to tailor the aeroelastic stability and response without any uncertainty.

Two theoretical approaches applicable to the aeroelastic stability and response of the composite structures with uncertainty in the structural and damage parameters were then explored. The Polynomial Chaos Expansion approach (with regression and statistically averaging methods) was applied for the uncertainty quantification in the aeroelastic stability and response. Similarly, the Interval Analysis approach, when information of uncertainty is imprecise, was used to determine the uncertainty quantification in the aeroelastic stability and response.

These approaches were applied to the idealised composite wing model, the Goland wing model and a more realistic full-scale aircraft FE composite wing model, with an excellent agreement of the uncertainty quantification of the aeroelastic stability and response compared with the Monte Carlo Simulations being obtained.

A new concept for the prediction of the robust optimum aeroelastic design, for the single and multi-objective functions, based on PDF estimates obtained from the PCE approach, was proposed and applied successfully on the wind tunnel composite wing model.

A new concept for the prediction of the robust optimum aeroelastic design for the single and multi-objective functions, based on upper and lower bound curves of the real part of the eigenvalues, was proposed and applied successfully on the wind tunnel composite wing model.

The effect of damage, due to matrix cracks of various amounts of crack density and fibre breakage, on the aeroelastic stability of the full-scale aircraft FE composite wing model, as well as gust response and static wing deflection, were also explored. Significant reduction of the flutter speed was noted due to the damage.

Such proabailistic and non-probabilistic approaches by including the structural and damage uncertainties can be applied to the composite aircraft design and certification process. While in the designing phase, a least sensitive design (a robust optimum design) by including uncertainties can be obtained by analysing the PDF estimates predicted by the PCE approach or upper and lower bounds predicted by the Interval Analysis approach. The performance of produced design by adopting these approaches against some design speed is likely to be better in terms of proabability or measure of failure compared with the traditional deterministic design approaches, which are based on the crisp values of structural paramaters.

Such an approach could arguably be employed for aircraft certification and not just for composite designs. Currently, a design flutter boundary is specified which must be demonstrated by flight test, however, a

flutter free safety margin (typically 15%) must also be validated using extrapolation of flight test results and the worst case bending moments obtained from a range of different gust cases. For a probabilistic approach, the PDFs due to uncertainties (including flight condition) would need to be shown to be above the design flutter speed rather than simply defining a safety margin, and a similar approach taken for the gust response. Similarly, for the non-probabilistic approach, the lower bound of the flutter speed due to uncertainties (including flight condition) needs to be shown to be above the design flutter speed.

A new concept of handling the matrix cracks in the probabilistic manner was proposed for the flutter speed PDF. This PCE based FE model can allow the possibility of the damage tolerant designs to be explored.

Finally, the PCE approach was applied successfully to predict the uncertain bounds of the FRF of a simple beam and full-scale aircraft FE composite models.

Future Work

A non-sample based Galerkin projection method may be explored to predict the effects of uncertainties on the aeroelastic stability and response. Such approach will require the formulation of system of equations involving beta coefficients and some technique or approach will then be required to find these coefficients. A robust design approach without utilizing the PDF estimates may then be explored.

In the robust design approach, the feasible design space should be increased e.g. allowing for thickness and mass variation in the wing panels. Such an increase in the size of feasible design space (to be

explored) will be required for the large and complex aeroelastic systems.

The weighted sum approach to generate Pareto points which show the non-convex behaviour has been criticised in the literature, therefore, other techniques such as NBI (Normal Boundary Intersection) may be explored to generate smooth Pareto points for finding the best Pareto solution.

Uncertainty in the position of the damage may be incorporated to explore the damage-tolerant designs.

The PCE approach for the industrial aircraft model with large number of uncertain parameters needs to be explored to find its limitations.

References:

1. J.R.Wright & J.E.Cooper, *Introduction of Aircraft Aeroelasticity and Loads*. 2007: John Wiley & Sons Ltd.
2. R.Talreja, *Stiffness Properties of Composite Laminates with Matrix Cracking and Interior Delamination.* Engineering Fracture Mechanics, 1986. **25**(5/6): p. 751-762.
3. G.J. Dvora, N. Laws, & M. Hejazi, *Analysis of Prgressive Matrix Cracking in Composite Laminates. I. Thermoelastic Properties of a Ply with Cracks.* Journal of Composite Materials, 1985. **19**: p. 216-234.
4. B.C. Hoskin & A.A. Baker, *Composite Materials for Aircraft Structures*, ed. J.S. Przemieniecki. 1986, New York: AIAA.
5. H.B. & C.T. Sun, *Hygrothermal Effects on the Stress Field of Laminated Composite* Journal of Reinforced Plastics and Composites, 1989. **40**(8): p. 40-54.
6. D.H.Hodges & G.A.Pierce, *Introduction to Structural Dynamics and Aeroelasticity*. 2002, Cambridge: Cambridge University Press.
7. R.L.Bisplingoff, *Aeroelasticity*. Vol. 2. 1983, New York: Dover Publisher.
8. Y.C.Fung, *An Introduction to the theory of Aeroelasticity*. 1993, Mineola,New York: Dover Publications.
9. T.A.Weisshaar & B.L.Foist, *Vibration Tailoring of Advanced Composite Lifting Surfaces.* Journal of Aircraft, 1985. **22**(2): p. 141-147.
10. L. Librescu & S.Thangjitham, *Analytical Studies on Static Aeroleastic Behavior of Forward-Swept Composite Wing Structures.* Journal of Aircraft, 1991. **28**(2): p. 151-157.

11. S.J.Hollowell & J.Dugundji, *Aeroelastic Flutter and Divergence of Stiffness Coupled, Graphite/Epoxy Cantilever Plates.* Journal of Aircraft, 1984. **21**(1): p. 69-76.
12. M. H. Datoo, *Mechanics of Fibrous Composites.* 1991, New York: Elsevier Science Publishing Co., Inc.
13. I.Lottati, *Flutter and Divergence Aeroelastic Characteristics for Composite Forward Swept Cantilevered Wing.* Journal of Aircraft, 1985. **22**(11).
14. Jiann-Quo. Tarn Kuo-Juin. Lin., *Flutter Analysis of Cantilever Composite Plates in Subsonic Flow.* AIAA, 1989. **27**(8): p. 1102-1109.
15. S.Haldar.& M.Mukhopadhyay M.K. Pandit, *Free Vibration Analysis of Laminated Composite Rectangular Plate Using Finite Element Method.* Journal of Reinforced Plastics and Composites, 2007. **26**(1): p. 69-80.
16. D. Kr. Maiti & P.K. Sinha, *Bending and free vibration analysis of shear deformable laminated composite beams by finite element method.* Composite Structures, 1994. **29**: p. 421-431.
17. Akram Al-Obeid, *Vibration and Buckling of Laminated Composite Plates With Various Boundary Conditions*, in *Department of Aeronautical Engineering.* 1993, The University of Manchester, UK: Manchester.
18. S.Guo, W.Cheng, & D.Cui, *Aeroelastic Tailoring of Composite Wing Structures by Laminate Layup Optimization.* AIAA, 2006. **44**(12): p. 3146-3149.
19. T.A.Weisshaar, *Aeroelastic Tailoring of Forward Swept Composite Wings.* Journal of Aircraft 1981. **18**(8): p. 669-676.
20. L. Librescu & J.Simovich, *General Formulation for the Aeroelastic Divergence of Composite Swept-Forward Wing Structures.* Journal of Aircraft, 1988. **25**(4): p. 364-371.

21. Kyo-Nam. Koo, *Aeroelastic Charecteristics of Double-Swept Isotropic and Composite Wings.* Journal of Aircraft, 2001. **38**(2): p. 343-348.

22. S.S.Rao, *Optimisation of Airplane Wing Structures Under Gust Loads.* Computers and Structures, 1982. **21**(4): p. 741-749.

23. Tae-Uk. Kim & I.H.Hwang, *Optimal design of composite wing subjected to gust loads.* Computers and Structures, 2005. **83**: p. 1546-1554.

24. S.J.Miller. *Wing Design Incorporating a Passive Loads Alleviation Device.* in *Aircraft Structural Design, Challenges for the next Generation-Concept to Disposal.* 2008. Liverpool: Royal Aeronautical Society.

25. A. Manan & J.E.Cooper. *Robust Design of Composite Wings for Gust Response.* in *50th AIAA/ASME/ASCE/AHS/ASC Structures, Structural Dynamics, and Materials Conference.* 2009. Palm Springs, California.

26. G.Vio & J.E.Cooper. *Optimisation of Composite Wing Structure for Passive Gust Alleviation.* in *Aircraft Structural Design, Challenges for the next Generation- Concept to Disposal.* 2008. Liverpool: Royal Aeronautical Society.

27. K. Wilkinson, J. Markowitz, E.Lerner, D.George & S.M. Batill, *FASTOP: A Flutter and Strength Optimization Program for Lifting-Surface Structures* Journal of Aircraft, 1977. **14**(6): p. 581-587.

28. J.Kuttenkeuler & U. Ringertz, *Aeroelastic tailoring considering uncertainties in material properties.* Structural Optimization, 1998. **15**: p. 157-162.

29. T.J. Hertz & T.A. Weisshaar M.H. Shirk., *Aeroelastic Tailoring-Theory,Practice, and Promise.* Journal of Aircraft, 1986. **23**(1): p. 6-18.

30. T.A.Weisshaar & R.J.Ryan, *Control of Aeroelastic Instability Through Stiffness Cross-Coupling.* Journal of Aircraft, 1981. **23**(2): p. 148-155.

31. T.A.Weisshaar & D..K.Duke, *Induced Drag Reduction Using Aeroelastic Tailoring with Adaptive Control Surfaces.* Journal of Aircraft, 2006. **43**(1): p. 157-164.

32. S. Guo., *Aeroelastic optimization of an aerobatic wing structure.* Aerospace Science and Technology 2007. **11**: p. 396-404.

33. J.A.Green, *Aeroelastic Tailoring of Aft-Swept High-Aspact-Ratio Composite Wings.* Journal of Aircraft, 1986. **24**(11): p. 812-819.

34. K.Isogai, *Direct Search Method to Aeroelastic Tailoring of a Composite Wing under Multiple Constraints.* Journal of Aircraft, 1989. **26**(12): p. 1076-1080.

35. M. Allen & K. Maute, *Reliability-based design optimization of aeroelastic structures.* Structural and Multidisciplinary Optimization, 2004. **28**: p. 228-242.

36. H. Bae, R.V. Grandhi & R.A. Canfield, *Uncertainty Quantification of Structural Response Using Evidence Theory.* AIAA, 2003. **41**(10): p. 2026-2068.

37. Y Ben-Haim, *Information-gap decision theory: decisions under severe uncertainty*. 2001: Academic Press.

38. A. Hunter & S.Parsons, *Applications of Uncertainty Formalisms,pp.8–32*. 1998, New York: Springer.

39. R.E. Moore, *Interval Analysis*, ed. G. Forsythe. 1966, New York: Prentice-Hall.

40. R.E. Moore, *Methods and Applications of Interval Analysis*, ed. W.F. Ames. 1979, Philadelphia: SIAM.

41. G. Shafer, *A Mathematical Theory of Evidence*. 1976, Princeton, NJ: Princeton Univ. Press.

42. N. Wiener, *The Homogeneous Chaos.* American Journal of Mathematics, 1938. **60**(4): p. 897-936.

43. R.G.Ghanem and P.D.Spanos, *Stochastic Finite Elements: A Spectral Approach.* 1991, New York: Springer-Verlag.

44. Roger Goerge Ghanem, *Analysis of Stochastic Sytems with Discrete Elements* in *Engineering.* 1988, Rice: Housten,Texas. p. 232.

45. D.Xiu & G.Em. Karniadakis, *The Weiner-Askey Polynomial Chaos for Stochastic Differential Equations.* Journal on Scientific Computing, 2002. **24**(2): p. 619-644.

46. D.Xiu & G.Em.Karniadakis, *Modeling uncertainty in flow simulations via generalized polynomial chaos.* Journal of Computational Physics, 2003. **187**: p. 137-167.

47. S. K. Choi, R. V. Grandhi, R. A. Canfield & C. L. Pettit. , *Polynomial Chaos Expansion with Latin Hypercube Sampling for Estimating Response Variability.* AIAA, 2004. **42**(6): p. 1191-1198.

48. Z.Qiu & X. Wang, *Parameter perturbation method for dynamic response of structures with uncertain-but-bounded paramters based on interval analysis.* Internaltional Journal of Solids and Structures, 2005. **42**: p. 4958-4970.

49. Z.Qiu & X. Wang, *Comparison of dynamic response of structures with uncertain-but-bounded parameters using non-probabilistc interval analysis method and probabilistic approach.* International Journal of Solids and Structures, 2003. **40**: p. 5423-5439.

50. Z.Qiu, L. Ma & X. Wang, *Non-probabilistic interval analysis method for dynamic response analysis of nonlinear systems with uncertainty.* Journal of Sound and Vibration, 2009. **319**: p. 531-540.

51. C.L. Pettit, *Unceratinty Quantification in Aeroelasticity : Recent Results and Research Challenges.* Journal of Aircraft, 2004. **41**(5): p. 1217-1229.

52. P.S.Beran, C.L. Pettit & D.R. Millman, *Uncertainty quantification of limit-cycle oscillations.* Journal of Computational Physics, 2006. **217**: p. 217-247.

53. S.C.Catravete & R.A. Ibrahim, *Effect of stiffness uncertainties on the flutter of cantilever wing.* AIAA, 2008. **46**(4): p. 925-935.

54. L.G.Crespo, D.P.Giesy & S.P.Kenny, *Robustness analysis and robust design of uncertain systems.* AIAA, 2008. **46**(2): p. 388-396.

55. F.S. Hover and M.S Triantafyllou, *Application of polynomial chaos in stability and control.* Automatica, 2006. **42**: p. 789-795.

56. A.H.C. Smith, *Robust and optimal control using polynomial chaos theory*. 2007, South Carolina: South Carolina.

57. L.Mathellin, M.Y.Hussaini & T.A.Zang, *Stochastic approaches to uncertainty quantification in CFD simulations.* Numerical Algorithm 2005. **38**: p. 209-136.

58. O.M. Knioa & O.P. Le Maître, *Uncertainty propagation in CFD using polynomial chaos decomposition.* Journal of Fluid Dynamics Research, 2006. **38**: p. 616-640.

59. G.Taguchi, E. Elsayed & T. Hasiang, *Quality Engineering in Production Systems*. 1989, New York: McGraw-Hill.

60. Z.P. Mourelatos & J. Liang, *A Methodology for Trade-Off Performance and Robustness Under Uncertainty.* Journal of Mechanical Design, 2006. **128**: p. 856-863.

61. M.Dodson & G.T. Parks, *Robust Aerodynamic Design Optimization Using Polynomial Chaos.* Journal of Aircraft, 2009. **46**(2): p. 635-646.

62. C.Zang, M.I.Friswell & J.E.Mottershead, *A review of robust optimal design and its application in dynamics.* Computers and Structures, 2005. **83**: p. 315-326.

63. S. K. Choi, R. V. Grandhi, & R. A. Canfield, *Reliability-based Structural Design*, ed. Springer. 2007.

64. K.L. Reifsnider, K. Schulte & J.C. Duke, *Long-term Fatigue Behavior of Composite Materials.*, in *Long-term behavior of Composites,ASTM STP 813*. 1983: Philadelphia. p. 136-159.

65. D.R.Sanders, Y.I.Kim, & N.Stubbs, *Nondestructive Evaluation of Damage in Composite Structures Using Modal Parameters.* Experimental Mechanics, 1992. **32**: p. 240-251.

66. Wen-Hwa. Chen & Heng-Chih. Lin, *Flutter Analysis of Thin Cracked Panels Using the Finite Element Method.* AIAA, 1985. **23**(5): p. 795-801.

67. F.G.Hemmig & V.B.Venkayya, *Flutter Speed Degradation of Damaged, Optimized Flight Vehicles.* Journal of Aircraft, 1980. **17**(12): p. 833-834.

68. H. Arizono, *Application of genetic algorithm for aeroelastic tailoring of a cranked-arrow wing.* Journal of Aircraft, 2005. **42**(2): p. 493-499.

69. F.E. Eastep, V.A.Tischler, V.B.Venkayya, & N.S.Khot, *Aeroelastic Tailoring of Composite Structures.* Journal of Aircraft, 1999. **36**(6): p. 1041-1047.

70. F.E.Eastep, V.B.Venkayya, & V.A. Tishler, *Divergence Speed Degradation of Forward-Swept Wings with Damaged Composite Skin.* Journal of Aircraft, 1984. **21**(11): p. 921-923.

71. R.K.Kapania & F.Castel, *A Simple Element for Aeroelastic Analysis of Undamaged and Damaged Wings.* AIAA, 1990. **28**(2): p. 329-337.

72. T.Kim, S.N. Atluri & R.G. Loewy, *Modeling of Microcrack Damaged Composite Plates Undergoing Nonlinear Bimodular Flutter Oscillations.* AIAA, 1998. **36**(4): p. 598-606.

73. K.Wang & D.J.Inman, *Crack-Induced Effects on Aeroelastic of an Unswept Composite Wing.* AIAA, 2007. **45**(3): p. 542-551.

74. D.W.Jensen, E.F. Crawley & J.Dugundji, *Vibration of Cantilevered Graphite/Epoxy Plates With Bending-Torsion Coupling.* Journal of Reinforced Plastics and Composites, 1982. **1**: p. 224-269.

75. G.J. Hancock & J.R. Wright, *On the teaching of the principles of wing flexure-torsion flutter.* Aeronautical Journal, 1985: p. 285-306.

76. M.Mitchell, *An Introduction to Genetic Algorithms.* 1996: MIT Press.

77. Lawrence Davis, *Handbook of Genetic Algorithms.* 1991: ITP, Internal Thomson Publishing Company.

78. M. Clerc., *Particle Swarm Optimization.* 2006: ISTE Ltd.

79. A.Manan, G.Vio,M.Y. Harmin &J.E.Cooper, *Optimisation of the aeroelastic composite structures using evolutionary algorithms.* Journal of Engineering Optimisation, 2009. **In press**.

80. R.E.Steuer, *Multiple criteria optimisation:theory,computation and application.* 1986, New York: John Wiley.

81. A. Manan & J.E.Cooper, *Design of Composite Wings Including Uncertainties: A Probabilistic Approach.* Journal of Aircraft, 2009. **46**(2): p. 601-607.

82. X. Wang & Z. Qiu, *Nonprobabilistic Interval Reliability Analysis of Wing Flutter.* AIAA, 2009. **47**(3): p. 743-748.

83. M.D.Mckay, R.J.Beckman & W.J.Conover, *A comparison of three methods for selecting values of input variables in the analysis of output from a computer code.* Technometrics, 1979. **21**(2): p. 239-245.

84. D. J. Ewins, *Modal Testing-Theory, Practice and Application*, ed. R.S.P. Ltd. 2002.

85. M.H. Richardson & D.L. Fermenti. *Parameter Estimation from Frequency Response Measurements using Rational Fraction Polynomials*. in *1st IMAC conference*. 1982. Orlando, Florida.

86. D.Ghosh, R. Ghanem & J.Red-Horse, *Analysis of Eigenvalues and Modal Interaction of Stochastic Systems.* AIAA, 2005. **43**(10): p. 2196-2201.

87. D.H.Oh & L.Librescu, *Free vibration and reliability of composite cantilevers featuring uncertain properties.* Reliability Engineering and System Safety, 1997. **56**: p. 265-272.

88. M.I.Friswell & S.Adhikari, *Derivatives of Complex Eigenvectors Using Nelson Method.* AIAA, 2000. **38**(12): p. 2355-2357.

89. S.Adhikari, *Rate of Change of Eigenvalues and Eigenvectors in Damped Dynamic System.* AIAA, 1999. **37**(11): p. 1452-1458.

90. R.B. Nelson, *Simplified Calculation of Eigenvertor Derivatives.* AIAA, 1976. **14**(9): p. 1201-1205.

91. G.Dimitriadis & J.E.Cooper, *Prediction of Flutter Boundaries During Flight Flutter Testing.* Journal of Aircraft, 2001. **38**(2): p. 355-367.

Appendix A

Two-phase model- A composite ply with tranverse matrix cracks

Two phase method is an approach which predicts the reduction in the composite ply stiffness values due to presence of the tranverse matrix cracks[3]. To explain this concept, consider an infinite fibrous media with slit cracks assumed to be the elliptical shape. Let 'a' and 'b' be the major and minor semi-axes of the ellipsoidal crack and let η be number of these cracks per unit area of x_1-x_2 plane.

Area of one ellipsoidal crack $= \pi ab$ and
Area of η number of cracks$= \pi \eta ab$ (1)

Equation (1) can be simplified to

$$\text{Area of } \eta \text{ number of cracks} = \frac{\pi}{4} \beta \delta \qquad (2)$$

where β is crack density parameter($= 4a^2\eta$) and δ is aspect ratio of the ellipsoidal crack ($= \frac{b}{a}$). Now suppose that if cracks have length '2a' then β is the average numbers of cracks in a square of side '2a'. Alternatively, when cracks are located in a ply, then β measure average distance between cracks and finally the distance for successive cracks comes out to be ($= \frac{2a}{\beta}$). β value ranges from 0 to 1, in which 0 is for non-existence of cracks.

To predict the overall compliance and hence stiffness, the unidirectional cracked composite layer is treated as an orthotropic homogeneous solid on a macro-scale for which the constitution equation of average stress-strain is given by[3]

$$\overline{\sigma} = L\overline{\varepsilon}, \overline{\varepsilon} = M\overline{\sigma} \tag{3}$$

in which L and M are stiffness and compliance matrices of order 6x6 respectively and are given by[3]

$$\begin{aligned} L &= L_o - \overline{\beta} L_o \Lambda L \\ M &= M_o + \overline{\beta}\Lambda \end{aligned} \tag{4}$$

where $\overline{\beta} = \frac{1}{4}\pi\beta$ and L_0 and M_0 are stiffness and compliance matrices of un-cracked composites. The Λ matrix in (4), has only three components and are expressed as[3]

$$\begin{aligned} \Lambda_{22} &= \frac{M_{22}M_{33} - M_{23}^2}{M_{33}}\left(\alpha_1^{1/2} + \alpha_2^{1/2}\right), \\ \Lambda_{44} &= \left(M_{44}M_{55}\right)^{1/2}, \\ \Lambda_{66} &= \frac{(M_{22}M_{33} - M_{23}^2)(M_{11}M_{33} - M_{13}^2)^{1/2}}{M_{33}}\left(\alpha_1^{1/2} + \alpha_2^{1/2}\right) \end{aligned} \tag{5}$$

where α_1 and α_2 are roots of following equation[3]

$$\left(M_{22}M_{33} - M_{23}^2\right)\alpha^2 - \left\{M_{33}M_{66} + 2\left(M_{12}M_{33} - M_{13}M_{23}\right)\right\}\alpha + M_{11}M_{33} - M_{13}^2 = 0 \tag{6}$$

M_{22}, M_{44} and M_{66} terms of the stiffness matrix [M] change (in this approach) whereas others remain same as that of un-cracked composite layer i.e.

$$
\begin{aligned}
&M_{11} = M_{11}^0, M_{12} = M_{12}^0, M_{13} = M_{13}^0 \\
&M_{23} = M_{23}^0, M_{33} = M_{33}^0, M_{55} = M_{55}^0 \\
&M_{22} = M_{22}^0 + \overline{\beta}\left(M_{22}M_{33} - M_{23}^2\right)\left(\frac{\alpha_1^{1/2} + \alpha_2^{1/2}}{M_{33}}\right), \\
&M_{44} = M_{44}^0 + \overline{\beta}\left(M_{44}M_{55}\right)^{1/2}, \\
&M_{66} = M_{66}^0 + \overline{\beta}\left(M_{22}M_{33} - M_{23}^2\right)^{1/2}\left(M_{11}M_{33} - M_{13}^2\right)^{1/2}\left(\frac{\alpha_1^{1/2} + \alpha_2^{1/2}}{M_{33}}\right)
\end{aligned}
\tag{7}
$$

and from equation (6)

$$
\begin{aligned}
&\alpha_1\alpha_2 = \frac{M_{11}M_{33} - M_{13}^2}{M_{22}M_{33} - M_{23}^2}, \\
&\alpha_1 + \alpha_2 = \frac{M_{33}M_{66} + 2\left(M_{12}M_{33} - M_{13}M_{23}\right)}{M_{22}M_{33} - M_{23}^2}
\end{aligned}
\tag{8}
$$

and unknown the shear compliance M_{44} can be obtained from equation (7)

$$
M_{44} = M_{44}^0 + \frac{\overline{\beta}}{2}\left[\overline{\beta}M_{55} + \left(\overline{\beta}^2 M_{55}^2 + 4M_{44}^0 M_{55}\right)^{1/2}\right] \tag{9}
$$

Equations (7) to (9) can be reduced to

$$
\begin{aligned}
&x = M_{22}M_{33} - M_{23}^2, \quad x_0 = M_{22}^0 M_{33} - M_{23}^2 \\
&y = M_{66}M_{33}, \quad y_0 = M_{66}^0 M_{33}, \\
&p = M_{11}M_{33} - M_{13}^2, \quad q = 2\left(M_{12}M_{33} - M_{13}M_{23}\right)
\end{aligned}
\tag{10}
$$

from which the following equation is formulated

$$y = y_0 + \left(\frac{p}{x}\right)^{1/2}(x - x_0) \tag{11}$$

and the solution of 'x' is obtained from

$$F(x) \equiv x - x_0 - \overline{\beta}\left\{3p^{1/2}x^{3/2} + (y_0 + q)x - p^{1/2}x_0x^{1/2}\right\}^{1/2} = 0$$
$$x_1 = x_0 - \frac{F(x_0)}{F'(x_0)} \tag{12}$$

Once x_1 is obtained, we can then calculate the remaining entries of M matrix (i.e. M_{22} and M_{66}) the inverse of which give us reduced stiffness matrix of cracked composite layer.